POLITECNICO

MILANO 1863

SCUOLA DI INGEGNERIA INDUSTRIALE
E DELL'INFORMAZIONE

Micro Electro-Thermo-Mechanical Actuators for On-chip Material Characterization

TESI DI LAUREA MAGISTRALE IN
MATERIALS ENGINEERING AND NANOTECHNOLOGY

Author: **Alberto Scotti**

Abstract

MEMS are nowadays quite widespread and their applications in every-day life, has led to the creation of more and more reliable devices. In this study, micro electro-thermal actuators (ETA) have been investigated for material characterisation, including the so-called "chipping" phenomenon, a major cause of malfunctioning due to the fragmentation of the structural materials, as a consequence of accidental impacts.

Initially, existing analytical models to understand ETA functioning have been applied, then numerical simulations, through the software Abaqus, have been carried out. In this phase, it has been essential to create a model that coupled the physical phenomena involved in the device functioning.

The experimental phase, on the fabricated latest versions of electro-thermal-mechanical actuators for the characterization of polycrystalline silicon, has been the next step. It has begun with the search for possible manufacturing defects that could have influenced the correct functioning. For both devices, no problems of any kind have been encountered in this regard, allowing to pass to the maximum operating limits investigation; the relationship between temperature and electrical conductivity has been then investigated, evidencing the conditions corresponding to a deviation from the ohmic trend of the V-I curve. Subsequently, the analysis of the motion of the two devices has been carried out, obtaining opposite results: while for the old version (labelled ETA3) it is possible to perform the characterization procedure, for the most recent version (labelled ETA4) no significant displacement values have been reached. To explain the latter results, simulations have been carried out in order to determine the possible causes; through electro-mechanical simulations, a bending of the comb finger arms has been found, which resulted in an increase in the measured capacity without the shuttle actually moving.

Keywords: MEMS, electro-thermal actuators, polycrystalline silicon, mechanical characterisation, chipping, impact analysis, multi-physics simulations

Sommario

Oggigiorno i MEMS (Micro Electro Mechanical Systems) sono diffusi in molteplici settori industriali, il che ha portato ad una loro produzione su larga scala. Questo ha comportato la necessità di conoscere e caratterizzare le proprietà dei materiali strutturali utilizzati nella loro realizzazione all'interno dei processi produttivi.

Il lavoro effettuato in questa tesi è focalizzzato su una specifica classe di micro dispositivi, gli attuatori elettro-termo-meccanici, al fine di indagare le proprietà meccaniche del silicio policristallino, un materiale tradizionalmente impiegato nei MEMS. In particolare, sono stati considerati micro-attuatori elettro-termo-meccanici per la caratterizzazione del fenomeno di "chipping", una possibile causa di malfunzionamento dovuto alla frammentazione e alla scheggiatura da impatto, osservabili nei dispositivi portatili dell'elettronica di consumo per uso quotidiano (es. smarthphone, computer portatili, auticolari senza fili ecc.). Due dispositivi sono stati progettati e realizzati, basati sul medesimo sistema di attuazione ma differenti nel meccanismo di caratterizzazione; su di essi sono state effettuate, in primo luogo delle simulazioni multifisiche (usando il software coomerciale Abaqus), seguite da un iter sperimentale.

La prima fase di lavoro è consistita nello studio dell'accoppiamento tra i diversi fenomeni fisici coinvolti, al fine di poter ottenere risultati simulati significativi. Successivamente si è passati alla fase sperimenatale, applicata su entrambi i dispositivi, e composta, in primo luogo, dalla verifica dell'effettiva mobilità del dispositivo, escludendo così ogni possibilità di malfunzionamento causato da difetti di fabbricazione. Successivamente, è stata condotta un'indagine sui limiti di funzionamento e sulla dipendenza delle proprietà del materiale dalla temperatura; è stato messo in luce che, a seguito di un aumento dei valori in ingresso, si è persa, nella versione più recente del dispositivo, la linearità nella relazione V-I, a causa di un aumento della resistività elettrica con la temperatura.

Il passo successivo nella procedura sperimentale è stato lo studio della mobibiltà di entrambi i moduli; mentre per il primo modulo, detto ETA3, è stata verificata la possibilità di procedere con la caratterizzazione del materiale, per la versione più recente, detta ETA4, non si è raggiunto il medesimo risultato, portando lo studio verso l'indagine delle cause di questo risultato inatteso. Sulla base delle ipotesi fatte, sono state effettuate

delle simulazioni meccaniche per indagare i possibili effetti delle vibrazioni di risonanza sulla struttura, supportate dall'analisi della frequency response function (FRF), da misure sperimentali della risposta in frequenza, senza esiti soddisfacenti. Sono state effettuate, quindi, delle simulazioni elettro-meccaniche per riprodurre un'interazione elettrostatica tra le facce dei condensatori, atti alla misura dello spostamento, ed è stata trovata una flessione dei rispettivi bracci, spiegando l'inatteso risultato.

A seguito dello studio è stato possibile affermare che, a causa dell'elevata inclinazione delle travi del sistema di attuazione, la versione più recente del dispositvo, detta ETA4, non è in grado di compiere spostamenti orizzontali necessari per procedere con l'effettiva caratterizzazione del silicio policristallino, così come progettato. Al contrario, considerando la versione precedente (ETA3), è possibile effettuare la procedura di caratterizzazione senza ottenere risultati a riguardo senza tuttavia giungere alla rottura da impatto, in quanto l'angolo delle travi è troppo piccolo per generare la forza richiesta per lo studio del fenomeno di "chipping".

Parole chiave: MEMS, attuatori elettro-termo-meccanici, silicio policristallino, caratterizzazione meccanica, chipping, analisi dell'impatto, simulazioni multifisiche

Contents

1 | Introduction

MEMS is the acronym for MicroElectroMechanical Systems. As the name implies, "Micro" is referred to the size scale, "Electro" involves both electricity and electronics fields and the movement of electrons, and, by introducing the term "Mechanical", also physical movable parts are included.

MEMS are usually the integration of both mechanical and electronics elements on a silicon wafer, exploiting specific micro-fabrication technologies, such as the ThELMA^{TM} process (Thick Epitaxial Layer for Micro-actuators and Accelerometer). This integration between miniaturized mechanical devices and electronic control, combined with the different realization processes, allows to create microsystems able to sense, transduce and report a certain signal. Thanks to the reliability of MEMS production processes and to the versatility in their possible application, in recent years their market has shown a growth like the Moore Law.

As a first approximation, it is possible to classify MEMS devices in two categories:

- Inertial Modules: devices able to sense mechanical and kinematic quantities such as accelerations and angular velocities (accelerometers and gyroscopes, respectively).

- Non-inertial Modules: all the devices that do not perform inertial measurements. For instance, piezolectric transducers (in particular PMUTs: piezoelectric micro-machined ultrasound transducers); micro-pumps (used, for example, in the bioengineering field); piezoresistive actuators; pressure, temperature and humidity sensors. Electro-thermal actuated micro-systems are another possible class of devices which belongs to this category.

The focus of this work is on non-inertial modules produced by STMicroelectronics, and specifically on electro-thermo actuated devices.

Typical MEMS devices manipulate energy in several physical domains; the micro-actuator systems presented in this thesis combine the electro, thermo and mechanical effects to induce large displacements, and they are called Electro-Thermal Actuators (ETA).

The electro-thermal actuation mechanism is widely present in literature, due to the flexibility in the material choice, low-cost fabrication, large displacement and high forces ca-

pabilities, using relatively low driving voltage difference. They do not involve electrostatic or magnetic fields for actuation: therefore, these devices are suitable for manipulation of biological samples and electronic chips [20]. Also, electro-thermal actuators can operate in air, vacuum, a dusty environment and a liquid medium.

1.1.   Aim and scope of the thesis

The present work aims to provide an investigation of the fabrication, operation principles and structural design of four different electro-thermo mechanical devices made to perform an on-chip mechanical characterization of different materials, and, more precisely, to get insights into the latter two ETAs that have been produced.

In the on-chip testing approach, both the specimen and the testing machine are developed at the micro-scale in the same die; conversely, an off-chip testing procedure exhibits an external actuator at higher scale compared to the die sample on which it is applied, similarly to the macro-scale approach, where a specimen is put in a larger testing machine. Thus, the advantages of the on-chip methodology for mechanical characterization at the micro scale derive from the possibility to test the material in conditions almost identical to those found in real applications, avoiding external disturbances coming from off-chip laboratory tests [7]. This actuation system has been used to design micro-systems for the on-chip mechanical characterization of the most diffuse MEMS material, i.e. polycrystalline silicon, hereafter labelled as $poly1$, and other materials at the nano scale, such as Carbon Nanotubes (CNT), see [2], [6], [7] and [9].

Firstly, a description of the four devices, all fabricated for the mechanical characterisation of a material at the micro scale, will be provided; more precisely, a device to reproduce tensile mechanical tests on CNT (called ETA1 in the following) and, the remaining three devices (ETA2, ETA3, ETA4) for the mechanical characterization of polycrystalline silicon, the main structural material used in the MEMS manufacturing process. ETA2 has been fabricated to perform axial tensile tests on a sample, in order to evaluate its elastic stiffness. ETA3 and ETA4 have been designed to reproduce one of the most common issue in MEMS, the mechanical failure induced by accidental impact, usually accompanied by the chipping phenomenon, i.e. the detachment of small fragments from the surface. Indeed, the extensive use of other MEMS into portable devices built according to the on-chip logic, has made accidental drops and other random loads a common instance, which, through MEMS devices, can be studied, in fact, in these testing devices the local fragmentation of a $poly1$ proof mass is intentionally obtained as a consequence of the impact against target.

The comparison between these ETAs considers also Capacitance-Voltage (C-V) tests, to measure the horizontal displacement thanks to capacitive sensing. Finally, experimental results for ETA4 have been also compared with the ones previously obtained through 3D multi-physics finite element (FE) simulations.

1.2. Structure of the thesis

A brief synthesis of the contents of every chapter is reported here to give a better description of which arguments have been treated in this thesis:

- *Chapter 1: Introduction*

- *Chapter 2: Structural and functional components of the devices*
  In this chapter, firstly, the devices considered and their fabrication process , followed by the common parts that characterise them have been introduced.

- *Chapter 3: Design of devices for on-chip mechanical tests*
  In this part it has been introduced the finite element formulation for elementary structure, aimed to the choice of the structural parameters for the tensile test devices fabrication. The focus has been moved to explanation of the governing physical phenomena acting on the devices.

- *Chapter 4: Numerical simulations*
  The choice of the material parameters and option analysis to be used for the numerical structural simulations with the program Abaqus, together with the obtained results have been discussed.

- *Chapter 5: Experimental set-up and results*
  This chapter presents the experimental configurations and the results obtained, particularly regarding maximum reached displacement and, finally, the release and impact procedure, aimed to the material characterization.

- *Chapter 6: Conclusions and future perspectives*
  This conclusive chapter summarize the results discussed in the previous parts, giving a final evaluation and a possible continuation of the work.

# 2 | Structural and functional components of the devices

As it has been anticipated in the chapter 1, in this work different electro-thermally actuated micro-devices have been compared.

1. ETA1: performs mechanical tensile tests on nano manipulated CNT samples;

2. ETA2: recreates purely tensile on-chip mechanical loading tests on a $0.7\mu m$ thick $poly1$ specimen, which has been fabricated together with the whole device;

3. ETA3 and ETA4: have been designed to carry out an on-chip mechanical testing on the impact behaviour of polycrystalline silicon samples.

The whole set of devices is characterised by the same working principle, electro-thermal actuation, which can be compared with electrostatic actuators in terms of the produced force. Joule heating is typically used to power these actuators, which generally operate at lower and more desirable voltages than electrostatic devices [10], causing a thermal expansion of the V-shaped beams anchored at the two ends, while an electric current is passing through the beams, see e.g. figure 2.1(a). The thermal stress caused by ohmic heating pushes the apex of the beam in rectilinear motion (parallel to the substrate), causing the movement of the whole shuttle [16].

These devices are all composed by four main parts: the *displacement sensor*, the *suspension springs* (including the ones connected to the heat sinks), the *electro − thermal actuator* and the *specimen* to be tested.

These components are exemplified in figure 2.1.
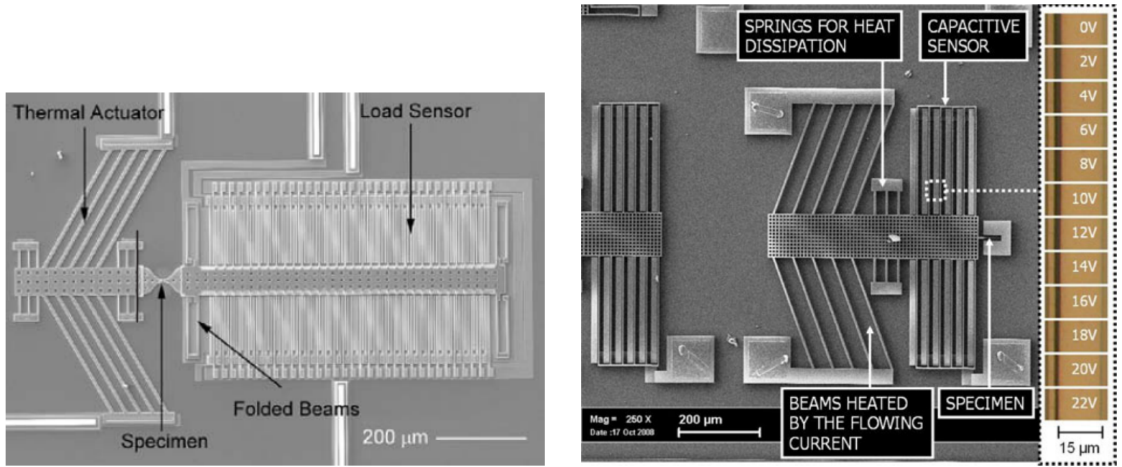
(a) *ETA*1*: micro system for nanoscale tensile tests of CNT specimen [6].*

(b) *ETA*2*: electro thermo mechanical actuator for on-chip tensile tests of poly1 sample [7].*
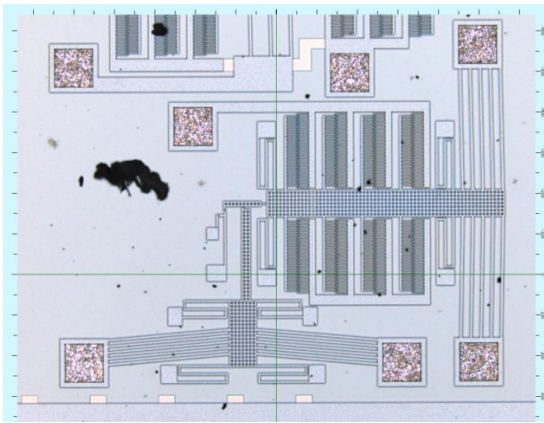
(c) *ETA*3*: prototype structure, for polysilicon impact characterization.*
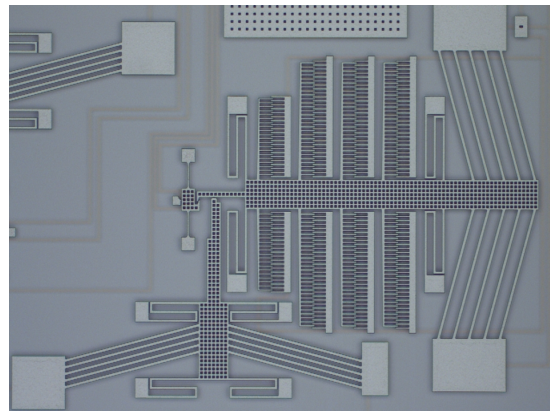
(d) *ETA*4*: device for impact and chipping characterization of polysilicon.*

Figure 2.1: Comparison between the four devices considered in this thesis.

Before addressing the description of the four devices and of the principles of the traditional capacitive approach, combined with the electro-thermo-mechanical coupled problem, the manufacturing process ThELMA^{TM}, used for the fabrication by STMicroelectronics, must be described.

2.1. The ThELMA^{TM} process

ThELMA ^{TM} (Thick Epitaxial Layer for Micro-actuators and Accelerometers) is the manufacturing process used by STMicroelectronics to produce the devices presented in this work.

This process is more complex than the common surface micromachining, but it allows thicker structures; thus, it results into more sensitive devices, allowing the possibility of measuring higher capacity values. Also, the mass is increased: this reduces the mechanical resonance frequency of the device.

The ThELMA process allows the realization of suspended structures anchored to the substrate through very compliant parts (springs), capable of moving on a plane parallel to the underlying silicon substrate [7].

2.1.1. Stages of the process

Here the ThELMA process is described briefly, considering the operations for a device realization, as depicted in figure 2.2.

1. *Substrate thermal oxidation.* The silicon wafer undergoes to high temperatures ($1100°C$) with the consequent formation of a thermal oxide layer (native oxide) 2.5 μm-thick.

2. *Deposition and patterning of horizontal interconnections.* On the thermal oxide layer a first polysilicon layer (*poly*1) is deposited, doped with phosphorous: it is used for *buried runners*. These are used to drive both potential and capacitance signals outside the MEMS, but they can be also used as a structural layer in thin polysilicon devices. This layer has been used for the fabrication of tensile specimens presented in this work.

3. *Deposition and patterning of a sacrificial layer.* Through a PECVD (Plasma Enhanced Chemical Vapour Deposition) process, a 1.6 μm-thick layer of oxide is deposited. This layer, summed with the thermal oxide, forms a 4.1 μm thick layer which provides a separation of the movable portion from the substrate, therefore it is considered as a *sacrificial layer*.

4. *Epitaxial growth of the structural layer (thick polysilicon).* Inside reactors, a polysilicon layer is made grow till reaching, nowadays, a thickness equal to 24 μm (previously it was 15 μm).

5. *Structural layer patterning by trench etch.* The movable parts are obtained through deep trench etch, which is able to reach the sacrificial oxide layer.

6. *Sacrificial oxide removal and contact metallization deposition.* The sacrificial oxide layer, thanks to selective chemical reaction, is removed. This process is carried

in dry conditions, to avoid *stiction* due to attractive capillarity reactions. The contact metallization is deposited to ensure the wire-bonding between the MEMS and the metallic frame.
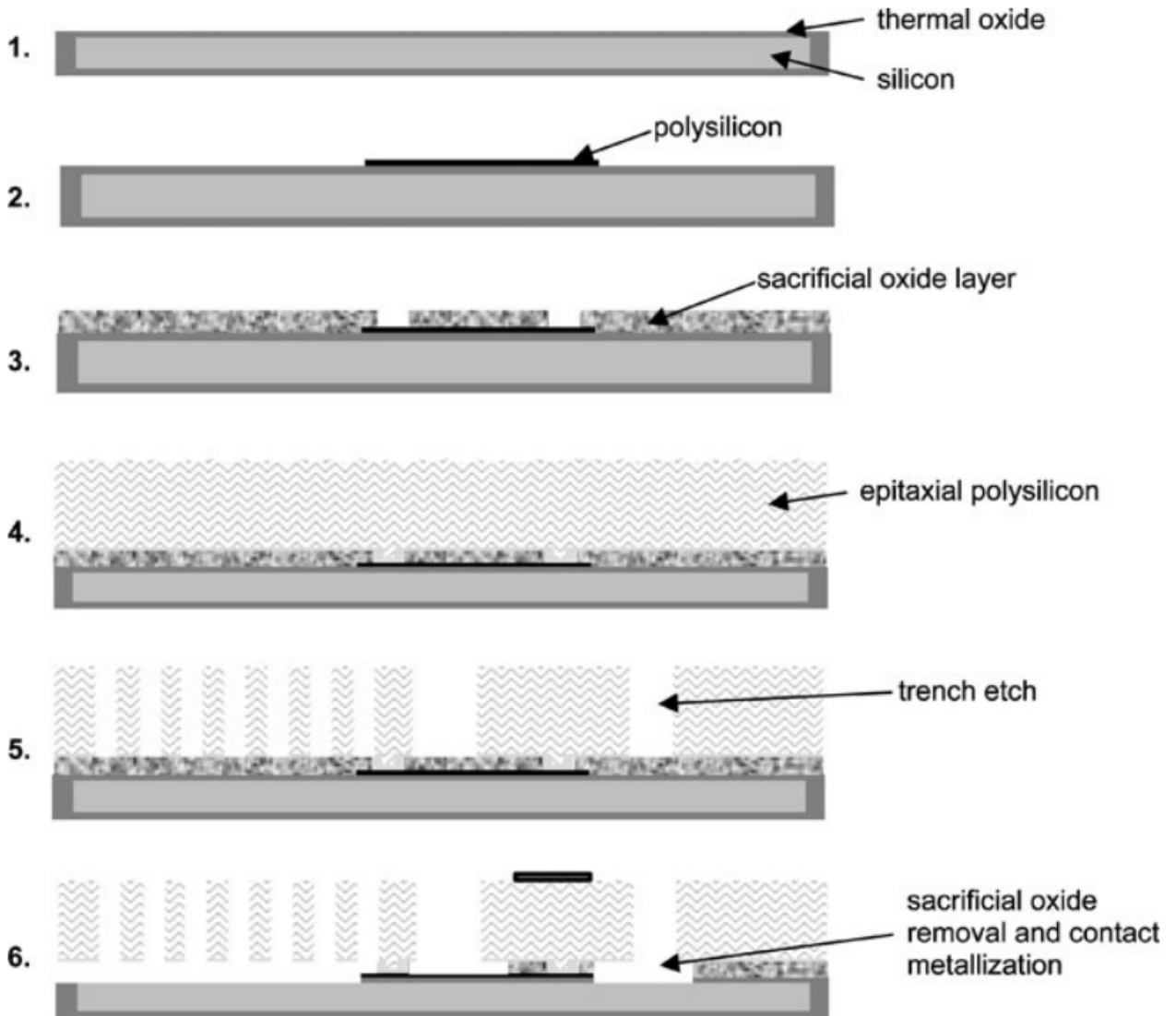
Figure 2.2: Schematic illustration of the ThELMA surface micromachining process.

The process is ended with additional steps required for the device's protection, such as wafer-to-wafer bonding. First of all, a second wafer is prepared, usually with a much simpler patterning than the first one, to be used as a cap for the previously patterned devices. Then, a *glue* is deposited by strips on the boundaries of the separating portions between each device, and the two wafers are pressed together at a controlled temperature. This

allows the sealing of the internal MEMS' environment but, on the other hand, increases the complexity of the manufacturing process.
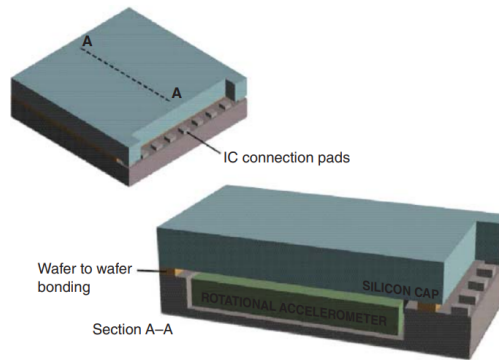
Figure 2.3: Single die and the cross-sectional view. IC, integrated circuit [8].

2.1.2. Technological limits

One of the main limitations of the ThELMA^{TM} technology concerns the maximum mass of polysilicon that can be achieved. Indeed, because of the removal step of the silicon oxide sacrificial layer (step 6), needed for the creation of suspended and movable geometry, HF is used. This acid penetrates from the upper part of the device through holes suitably created, in order to reach the oxide layer depth.

The quantity of excised SiO_2 is proportional to the exposure time with HF, but, at the same time, the removing capability of the acid decreases while it moves down below the rotor mass. As a consequence, a restriction on the structure dimensions is present.
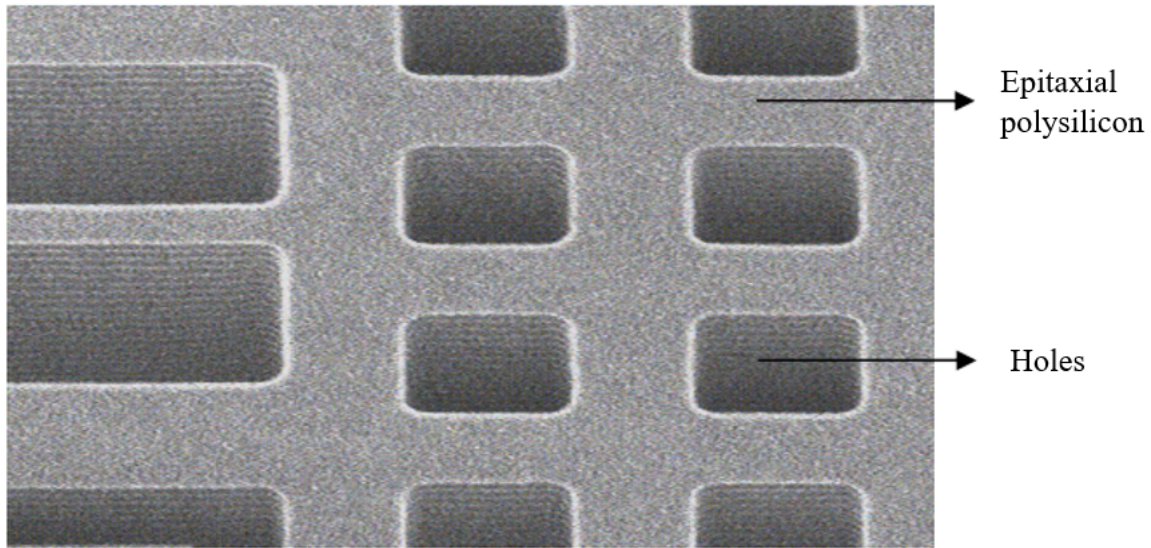
Figure 2.4: Perforated mass made of epitaxial polysilicon

Another aspect to be considered during the design is the so called *over − etch*: the designed structures in epitaxial polysilicon, after the ThELMA^{TM} process, are reduced by a (conventionally) constant quantity (averagely 0.3 μm) all over the boundaries. Typically this phenomenon is counterbalanced during design by oversizing some elements such as: supporting springs, actuation beams and the sensing portion.

Figure 2.5: Oversizing geometry during design to account for over-etch.

2.2. Displacement sensors

One of the common features between the considered ETAs is the capacitive sensing principle: the axial movement of the shuttle is perceived and measured by the capacitance variation.
Among these four devices, two sensing mechanisms have been considered:

1. parallel plate capacitors;

2. comb-finger capacitors.

The devices depicted in the figures 2.1(a) and 2.1(b) (ETA1 and ETA2) belong to the first group, while the ETA3 and ETA4 (figures 2.1(c) and 2.1(d)) to the second one.
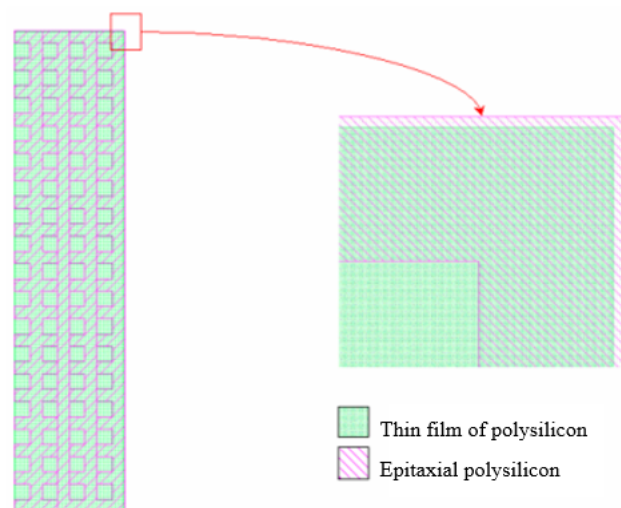Considering the first class, a parallel-plates capacitor is composed by two conductive plates with a surface S, placed at a certain distance d (the so-called gap) detached by a dielectric material. Between the two surfaces a constant potential is applied ($\bar{\varphi}$), and it can be verified that this varies linearly in the interposed dielectric material [8] (if fringing fields at the ends are neglected):
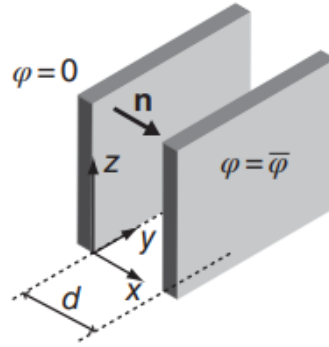
Figure 2.6: Parallel-plate capacitor.

Thus, the potential in the dielectric can be represented through the equation:

$$\varphi = \bar{\varphi}\frac{x}{d}. \tag{2.1}$$

The electric field ($\vec{E}$) along the x direction can be evaluated as the opposite of the partial derivative of φ with respect to x. Therefore, it is possible to compute the electrostatic energy as:

$$U = \int_{Space} \epsilon_r\epsilon_0|\vec{E}|^2 d\Omega = \frac{\epsilon_r\epsilon_0 S}{2}\frac{\bar{\varphi}^2}{d}. \tag{2.2}$$

From eq. 2.2, the capacitance for an ideal parallel-plate capacitor results to be:

$$C = \frac{\epsilon_r \epsilon_0 S}{d}. \tag{2.3}$$

Finally, by assuming a uniform charge distribution on the two plates, the resultant attractive force acting on one plate, pushing it to the other face, can be computed in the orthogonal direction to the plates as

$$F_{elec} = -\frac{\partial U}{\partial d} = -\frac{\epsilon_r \epsilon_0 S}{2} \frac{\bar{\varphi}^2}{d^2}. \tag{2.4}$$

It can be noticed the nonlinear dependence of both the capacitance and the electrostatic force on the relative distance between the two parallel plates. More precisely, the capacitance C is inversely proportional to d, while the electrostatic force to the second power of the gap.

The devices represented in the figure 2.1(c) and 2.1(d) (ETA3 and ETA4) are based, instead, on a different sensing mechanism: the comb-finger capacitor. This is represented in figure 2.7(a), where one element of the so called interdigitated comb-finger capacitor (figure 2.7(b)) is represented. The capacitor is formed by many comb-fingers repeated regularly.

(a) *Comb-finger capacitor.*   (b) *Interdigitated comb-finger capacitor, extracted from the device in fig.2.1(d)*
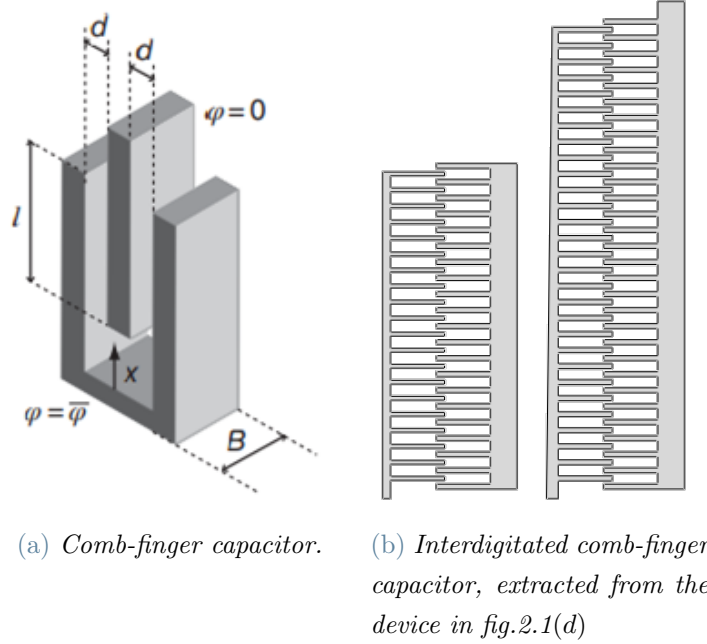
Figure 2.7: (a) Single element of the interdigitated comb-finger capacitor. (b) Interdigitated comb-finger capacitor.

A plate is centred, at a distance d, between two other parallel plates. In the analytical description, it is assumed that the distance l is sufficiently large to consider the electric field, generated by the applied voltage difference φ, only at the sides of the central surface. Fringing fields at the shorter edge and at the vertices of the surface are disregarded, as a first approximation. Therefore, the capacitance of the system, depicted in figure 2.7, can be approximated as the capacitance of two parallel isopotential plates connected in parallel, hence:

$$C = 2\frac{\varepsilon_r \varepsilon_0 Bl}{d}. \tag{2.5}$$

In this work, firstly, it must be emphasized that the measured capacitance is the result of the difference between the value during operative conditions (C_x), when the movable portion moves towards the fixed one, and the initial one (C_0).

$$\Delta C = C_x - C_0. \tag{2.6}$$

Considering, respectively, $C_0 = 2\frac{\varepsilon_0 x_0 tN}{d}$ and $C_x = 2\frac{\varepsilon_0 (x_0 + x) tN}{d}$ respectively, where the

parameters are initial penetration (x_0), the effective displacement due to the voltage application (x), the permittivity in vacuum (ε_0), the gap between the comb fingers plates (d) and the number of movable fingers (N), the capacitance variation (ΔC) will result as:

$$\Delta C = 2\frac{\varepsilon_0(x_0 + x)tN}{d} - 2\frac{\varepsilon_0 x_0 tN}{d} = 2\frac{\varepsilon_0 xtN}{d}, \tag{2.7}$$

and, therefore, the displacement can be obtained through the equation 2.7 as:

$$x = \frac{\Delta Cd}{2\varepsilon_0 tN}. \tag{2.8}$$

Under the same hypothesis, the electrostatic energy can be formulated as:

$$U = \frac{\varepsilon_r\varepsilon_0 Bl}{d} \cdot \varphi^2. \tag{2.9}$$

It is also possible to define the electrostatic force along the x direction, defined in figure 2.7. This could be done by considering the symmetric configuration of the capacitor, which allows the motion to act only along this direction.

$$F_{elec} = -\frac{\partial U}{\partial x} = -\frac{\partial}{\partial x}\frac{1}{2}\frac{2\varepsilon_r\varepsilon_0 B(l - x)}{d}\varphi^2 = \frac{\varepsilon_r\varepsilon_0 B}{d}\varphi^2. \tag{2.10}$$

It is worthwhile to mention that, differently from the parallel-plate configuration, in an ideal comb-finger setup, the electrostatic force does not depend on the coordinate along the direction of the possible relative motion between the two conductive portions of the device [8]. Another relevant difference between the two sensing configurations is the aforementioned pull-in phenomenon, which can be faced considering parallel plate capacitor. It can be understood by considering an electro-mechanical problem, which examines the reciprocal influences between mechanical and electrostatic variables.
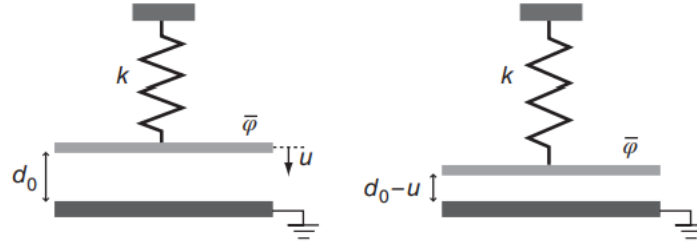
Figure 2.8: General scheme of an electro-mechanical problem, obtained by connecting a movable parallel plate capacitor to a linear elastic spring.

From figure 2.8, it is obvious that on the movable plate two different forces are acting: an elastic re-calling force (ku) and an electrostatic force.

Considering a static equilibrium situation, it is possible to write:

$$ku - \frac{\varepsilon_0 \varepsilon_r S}{2} \frac{\bar{\varphi}^2}{(d_0 - u)^2} = 0. \tag{2.11}$$

Relating the applied voltage difference $\bar{\varphi}$ to the displacement u, the resulting equation reads:

$$\bar{\varphi} = \sqrt{\frac{2k}{\varepsilon_0 \varepsilon_r S} u (d_0 - u)^2}. \tag{2.12}$$

The resulting plot of the eq. (2.12), as a function of normalized variables, is depicted in the figure 2.9. The maximum corresponds to the following displacement and potential values:

$$u \equiv u_{pi} = \frac{d_0}{3}, \tag{2.13}$$

$$\bar{\varphi} \equiv \bar{\varphi}_{pi} = \sqrt{\frac{8}{27} \frac{k}{\varepsilon_0 \varepsilon_r S} (d_0)^3}. \tag{2.14}$$

Figure 2.9: Non-dimensional voltage-displacement plot for a parallel-plate capacitor connected to an elastic spring [8].
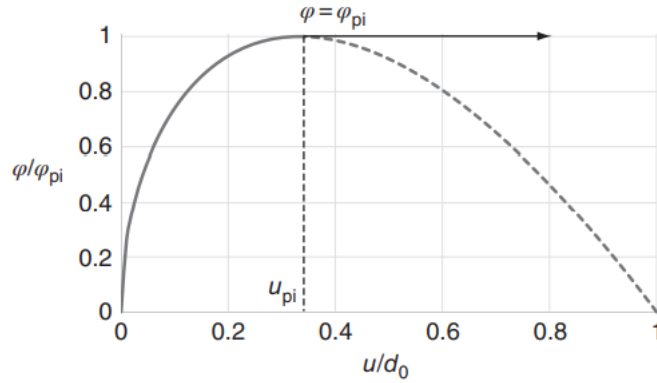
The subscript "pi" means pull-in, and the relative values correspond to pull-in values. This phenomenon can be understood by imagining that the device is controlled at increasing voltage difference between parallel plates. It can be seen from Figure 2.9 that, when the voltage and displacement reach the pull-in values, the static equilibrium can no longer be guaranteed and the movable parallel plate moves suddenly towards the opposite plate, closing the gap and creating a short circuit; in other words, the elastic force of the spring is no longer able to equilibrate the nonlinear electrostatic force and the configuration becomes unstable [8]. Notice that the pull-in value for the displacement u_{pi} means that a parallel-plate capacitor connected with a linear elastic spring can, in practice, be used until the gap reduces to one-third of the initial value [8].

This is precisely the reason why latest designed micro systems considered in this thesis (figures 2.1(c) and 2.1(d)) use comb-fingers capacitors as sensing mechanism: they cannot undergo to the pull-in phenomenon.

2.3. Suspension springs

The mechanical support of the structures depicted in the figures 2.1(c) and 2.1(d) is performed by folded springs and by the two pads, on which the potential difference is applied. The folded spring geometry is illustrated in the figure 2.10:
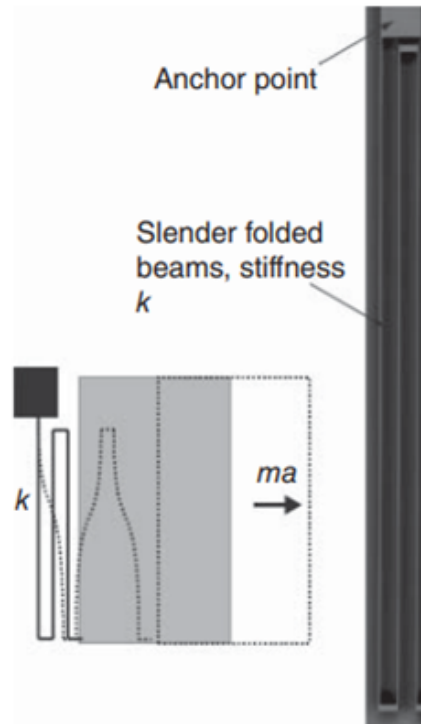
Figure 2.10: Folded spring, from: [8].

In order to calculate the stiffness of the suspension springs, first of all it must be assumed that only the vertical parts could be deformed, while the short horizontal ones and the big shuttle are rigid. Under this hypothesis, using the solution for a doubly clamped beam, the equivalent mechanical stiffness is expressed as:

$$k = \frac{12EJ}{n_{folds}l^3},$$
(2.15)

where n_{folds} is the number of the folds in the beam [8], namely three in figure 2.10.
This is the latest version of the suspension springs, present in the devices ETA3 and ETA4; in the other two devices depicted in figures 2.1(a) and 2.1(b), a different design has been chosen, where the parallel beams are connected directly to the central shuttle and the anchor. This configuration works in the same way of the previously described spring, so equation (2.12) has to be used with $n_{folds} = 1$.
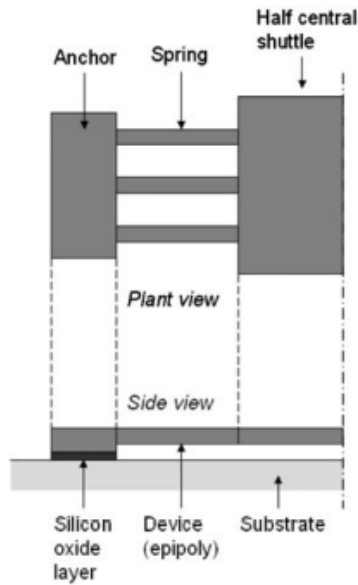
Figure 2.11: 3D FE model of the thermal sink springs [7].

Both the suspension spring cases do not only connect the shuttle to the substrate, providing a mechanical constraint to the actuator motion and avoiding the out-of-plane displacement, but also work as thermal sinks; therefore, they reduce the capacitive sensor and specimen temperature variation.

2.4.   Electro-Thermal Actuator Modelling

The procedure used to model the device has been derived from literature, in particular from [2], [6] and [23].
The analysis of a thermal actuator requires a coupled electric, thermal and mechanical investigation. In this section, the mechanical behaviour of the device is analytically derived on the basis of the following assumptions [23]:

1. The average temperature increase in the inclined beams of the thermal actuator is known;

2. The central shuttle is rigid and not affected by the temperature increase;

3. Small strains and displacements are considered, and the shear deformation of the beams is negligible, i.e. an infinite shear stiffness is assumed.

The basic constituent of the actuation model in an electro-thermal-actuator is a pair of n inclined beams, which are connected to the substrate, through pads, and to the central

rigid shuttle. Since it is the basic component of the actuation, the mechanical response of a single inclined beam has been computed, by exploiting symmetry, see figure 2.12.

(a)

(b)
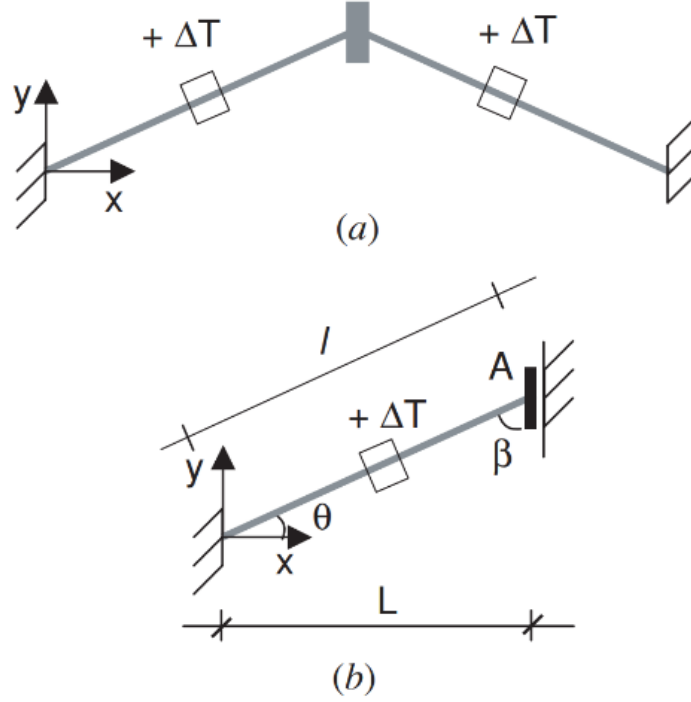
Figure 2.12: Schematic of a pair of inclined beams subjected to an average temperature increase: (a) two beams joint at the central shuttle and (b) equivalent mechanical representation of a single beam, by exploiting symmetry.

The mechanical response of the structure in figure 2.12(a) can be equivalently computed by considering half of the structure, as shown in figure 2.12(b), and in both cases the resulting formulation is obtained using the standard structural theory. The displacement at node A in the y-direction and the reaction force in the x-direction, due to an average temperature increase of ΔT along the beam, are given in the following:

$$U^{\Delta T} = U_y^A = \alpha \Delta T l \frac{s}{\left(s^2 + c^2 \frac{12l}{Al^2}\right)} = \alpha \Delta T l \frac{s}{\left(s^2 + \frac{c^2}{\psi}\right)}, \tag{2.16}$$

$$R_x^{\Delta T} = R_x^A = -\alpha \Delta T E A \frac{c}{\left(s^2 \frac{Al^2}{12I} + c^2\right)} = -\alpha \Delta T E A \frac{c}{\left(s^2 \psi + c^2\right)} \tag{2.17}$$

where α is the coefficient of thermal expansion of the beam material, E is the effective, isotropic Young's modulus of the material, l is the beam length, A is the beam cross

section, I is the moment of inertia of the cross section with respect to the out-of-plane axis z, and c and s are cosine and sine of the beam angle θ, as defined in figure 2.12(b). The dimensionless parameter $\psi = \frac{Al^2}{12I}$ is defined as the axial over bending stiffness ratio. To understand the mechanical behaviour of the whole device, it is also necessary to discuss the response of half-structure, as shown in figure 2.12(b), subjected to an external force applied to the central shuttle, acting in y direction as shown in figure 2.13 [6].
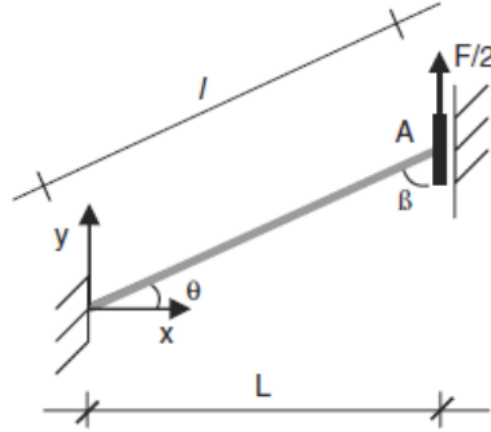
Figure 2.13: Schematic representation of an inclined beam subjected to a central force $F/2$ at one end [6].

The displacement at node A, due to an external force F applied to the central shuttle along the y-direction, is:

$$U^F = U_y^A = \frac{F}{2\left(s^2 \frac{EA}{l} + c^2 \frac{12EI}{l^3}\right)} = \frac{Fl}{EA} \frac{1}{2\left(s^2 + \frac{c^2}{\psi}\right)}. \tag{2.18}$$

From this equation the stiffness of the system of figure 2.13 for a displacement in the shuttle direction can be computed as the ratio:

$$K_b = \frac{F}{U_y^A} = \frac{2EA}{l}\left(s^2 + \frac{c^2}{\psi}\right). \tag{2.19}$$

As expected, the stiffness k_b varies continuously from the purely bending stiffness value $\frac{24EI}{l^3}$, when $\theta = 0°$, to the purely axial stiffness $\frac{2EA}{l}$, when $\theta = 90°$. As can be seen in the K_b's formulation, it is also dependent on ψ. The dependence on both ψ and θ is represented in figure 2.14, in which the $\frac{U_y^A}{\alpha \Delta Tl}$ versus θ at varying values of stiffness ratio ψ

is depicted (notice that $\alpha\Delta T$ is the beam strain due to thermal expansion, and θ ranges between 0-30°).
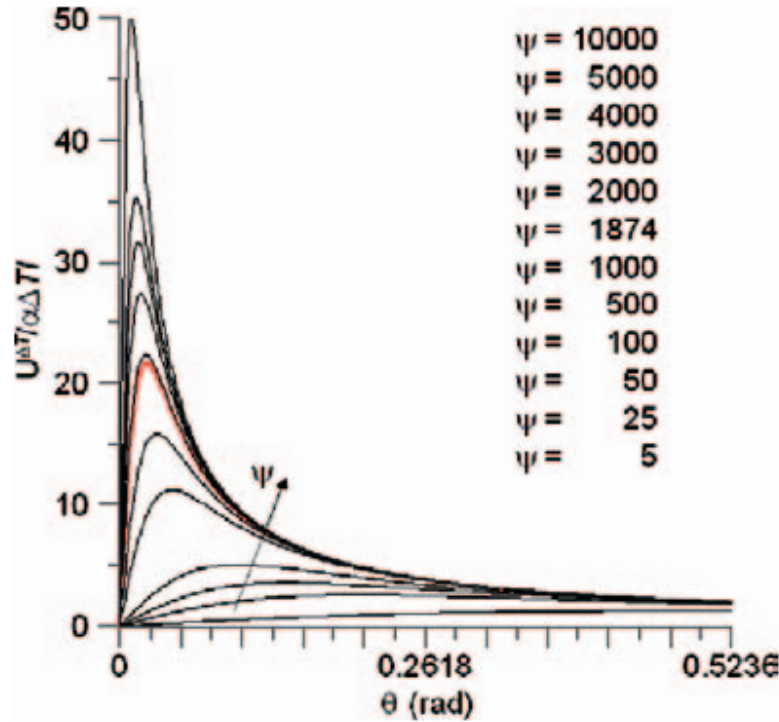
Figure 2.14: Inclined beam subjected to a uniform temperature increase: plots of the non-dimensional displacement of the shuttle as dependent on the stiffness ratio ψ [6].

As it can be noticed from figure 2.14, the best results in terms of displacement are achieved for really low angles.

In this work the V-shaped actuation structure is subjected both to an increase of temperature (ΔT) and to an external force (F), thus the total displacement is given by the superposition of the two contributes, described, respectively, by the equations (2.13) and (2.15):

$$U^{\Delta T+F} = U^{\Delta T} + U^F = \frac{(2\alpha\Delta T E A sin\theta + F)}{k_b}. \tag{2.20}$$

This is a valid analytical model to predict the displacement generated by V-shaped thermal actuator; however, in the considered devices its motion is hindered by a "sling-like" element with the own stiffness k_p.
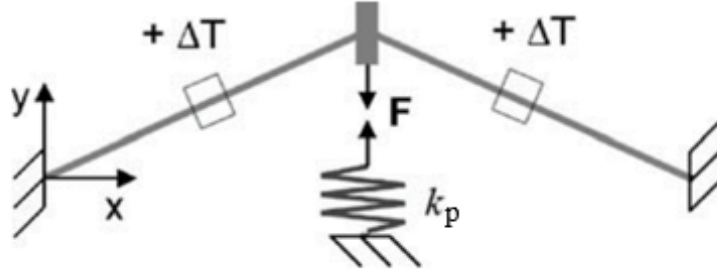
Figure 2.15: Schematic representation of a single V-shaped beam connected to the substrate with an elastic spring [6].

Accounting that the elongation of the spring coincides with the displacement of the device, and that the result can be extended to the whole structure just by considering all the beam couples as m equal springs with stiffness k_b and connected in parallel, the total displacement becomes:

$$U = \frac{2m\alpha\Delta T E A sin\theta}{mk_b + k_p}. \tag{2.21}$$

As it has been described before, the shuttle is also sustained by four heat sinks placed at specific points, which should contribute to heating dissipation, reducing the influence of the actuator temperature on the central portion of the shuttle, thus avoiding the thermal deformation of the specimen. They can be considered as springs connected in series with the device, and lumped into an equivalent elastic spring with stiffness k_{sTA} which opposes an elastic force with respect to the translation of the central rigid shuttle. The system under consideration is therefore schematized as shown in figure 2.16.
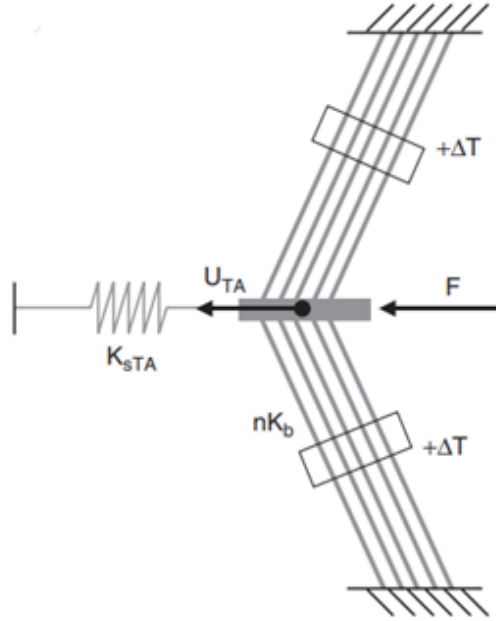
Figure 2.16: Schematic representation of the ETA constrained with suspension springs of total stiffness k_{sTA} [6]

Therefore, k_{sTA} can be computed as:

$$k_{sTA} = 2\frac{12EI_{sTA}}{l_{sTA}^3},$$ (2.22)

where I_{sTA} is the moment of inertia of the beam, and l_{sTA} is its length. This result is obtained under the hypothesis that the connecting portion between the folded beams (the shuttle) is rigid.

Imposing the kinematic compatibility, the total stiffness results to be:

$$k_{tot} = mk_b + k_p + nk_{sTA},$$ (2.23)

where m and n are the number of beams forming the V-shaped thermo actuator and the ratio between the number of heat sinks and the number of folded beams, respectively.

Thus, the displacement can be computed as:

$$U = \frac{(2\alpha\Delta TEAsin\theta + F)}{mk_b + k_p + nk_{sTA}}$$ (2.24)

This relationship between forces and displacements has been investigated in [6], where the same device was numerically tested using specimens with increasing stiffness, resulting into a consistent drop in the measured displacement. Tests have been also performed with different beam angles θ (5°, 15° and 30°) for fixed voltage value, and a correlation between the force generated and the angle seems to exist.

However, as it appears clearly in figure 2.17, forces and displacements have inverse proportionality with respect to the angle.

This means that for a high angle the device will exercise high forces and produce low displacements, while for a low angle the result will be the opposite.
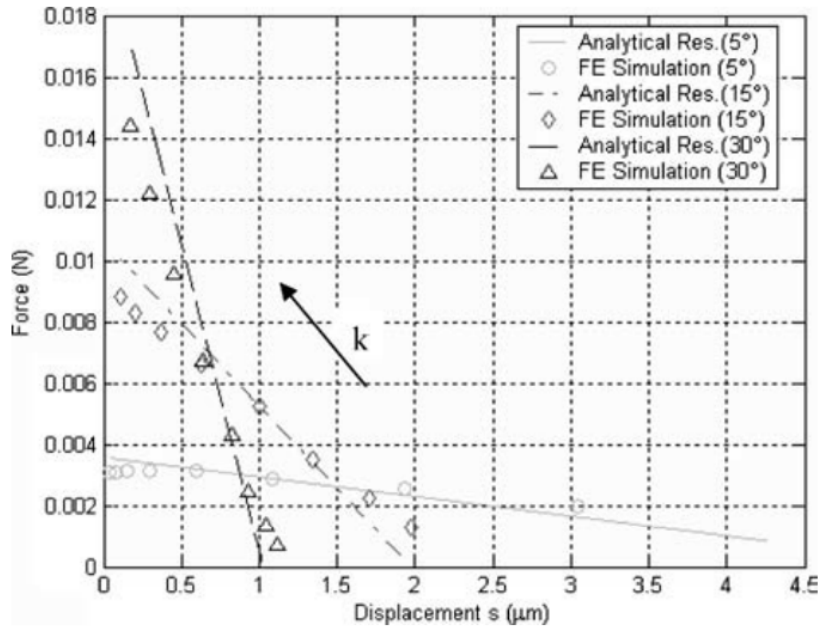
Figure 2.17: Single V-shaped beam connected to the substrate with an elastic spring and with an applied voltage $\Delta V = 8V$ .Results of FE simulations at varying elastic spring stiffness and angle θ, compared with analytical results [6].

It is important to estimate under which conditions the inclined beams might buckle. Buckling occurs when the internal force exceeds the critical buckling force. The boundary conditions for the beams (common for all the geometries considered) are: the anchor is fixed, while the other end, connected to the shuttle, cannot rotate but it can translate, see figure 2.12(b). Buckling occurs in the plane where the moment of inertia is minimum. It can be orthogonal to or parallel to the substrate, depending on the beam dimensions. The critical loads for buckling in the plane orthogonal to the substrate ($P_{cr_{min}}$) and in the plane parallel to the substrate ($P_{cr_{max}}$) are:

$$P_{cr_{min}} = \pi^2 \frac{EI_{min}}{l^2} = \frac{\pi^2 E}{l^2} \frac{tW^3}{12}; \qquad (2.25)$$

$$P_{cr_{max}} = \pi^2 \frac{EI_{max}}{l^2} = \frac{\pi^2 E}{l^2} \frac{Wt^3}{12}, \qquad (2.26)$$

where W is the width of a rectangular shape sample and t its thickness.
While the axial force acting on a single beam is:

$$N = R_x^{\Delta T} cos\theta + \frac{F}{2} sin\theta + R_x^F cos\theta = -\frac{\alpha \Delta T E A cos\theta^2}{\left(sin\theta^2 \frac{Al^2}{12I} + cos\theta^2\right)} + \frac{F sin\theta \psi}{2\left(sin\theta^2 \psi + cos\theta^2\right)}. \qquad (2.27)$$

By varying the parameters of this equation, it is then possible to evaluate if, for the angle and the ΔT chosen, the thermal actuator will buckle.
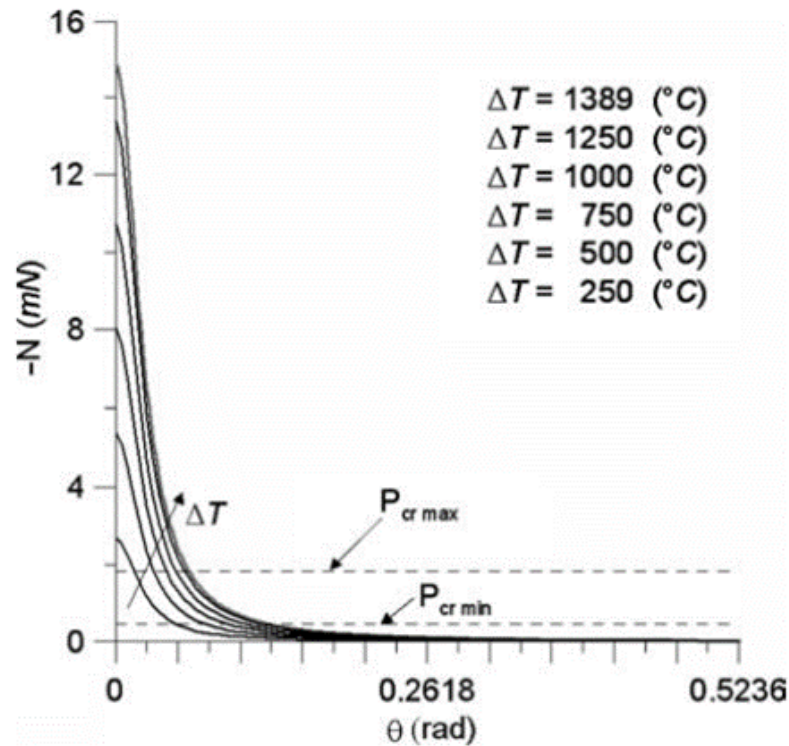

Figure 2.18: Plot of the compressive axial force in the beams of the thermal actuator, versus the angle θ at varying ΔT[6].

From the above considerations it can be concluded that buckling can occur for small angles θ, for high temperature increments and for very stiff specimen and suspension springs.

The behaviour of the whole device must be therefore carefully checked to avoid malfunctioning.

2.5.   Specimen types

Among the four considered electro-thermally actuated devices it is possible to distinguish as many different samples. Obviously, each sample is different from the other (except for the devices in figure 2.1(c) and 2.1(d)) due to the different aims of the design.

The structure depicted in figure 2.1(a) (ETA1) is built for tensile loading tests on CNT at the nano scale.

The second considered specimen, referring to ETA2, is made of a 0.7 μm thick poly1 layer, with a testing configuration similar to the one previously described for ETA1. Both devices can be used to test on other kinds of built-in specimens; the choice of an electro-thermo-

Figure 2.19: Detail of ETA1 concerning a CNT specimen [6].

mechanical actuator is driven by the higher loads which can be obtained with respect to an electrostatic actuator, considering the same area occupation and maximum applied voltage. The elongation of the specimen is measured during the tensile test by means of the capacitance variation of the electrostatic sensor. The force acting on the specimen can be derived from the applied voltage to the thermo-actuator.
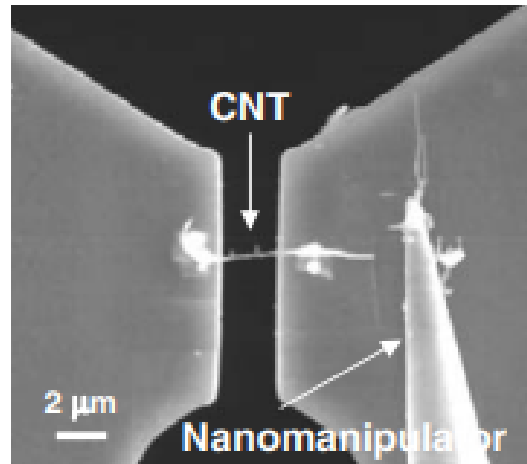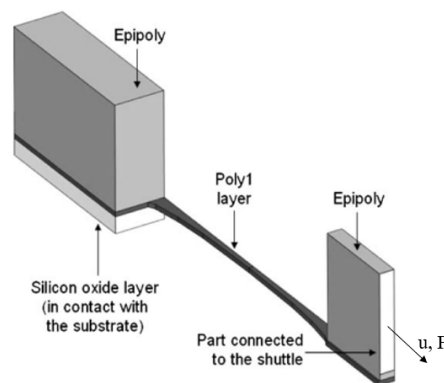

Figure 2.20: 3D model of the *poly*1 specimen testing setup in ETA2.

A peculiar feature of the proposed on-chip test device is that both the specimen elastic stiffness and the nominal tensile strength can be obtained through a unique back and forth loading cycle, in which the actuation force is slowly increased up to the specimen rupture and then slowly decreased back to zero [7].

The last two investigated devices, ETA3 and ETA4, have been designed and fabricated for the same aim: to investigate the so-called "chipping" problem, through an impact characterization of the polycrystalline silicon material. To perform these tests, it becomes necessary to design a device able to transform most of the work done by the force produced by the electro-thermo-mechanical actuator into kinetic energy. Indeed, even if the force generated by the electro-thermo-mechanical actuators is quite high, they cannot be used to directly test the material, like in the tensile strength tests performed in [6] and [7]. Among the many possible structures, the most efficient are the "hammer" and the "sling" configurations, described in the following more in details.

2.5.1. Chipping test device: hammer configuration (ETA3)
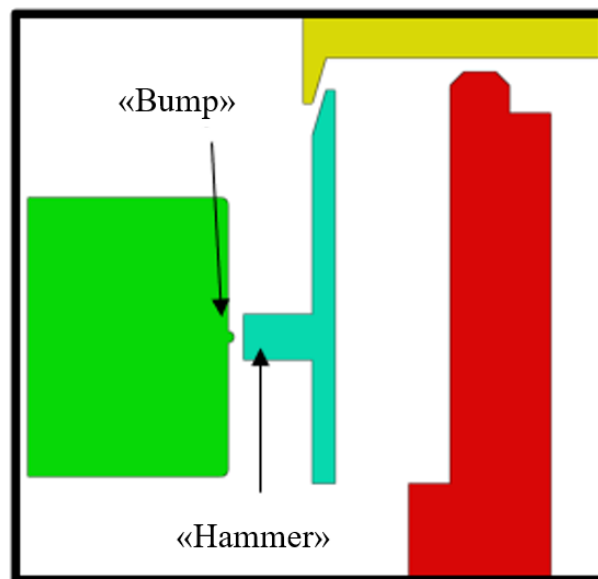
Figure 2.21: Schematic representation of the "hammer" structure for polysilicon impact testing (ETA3).

Even if the force generated by electro-thermo-mechanical actuators is quite high (at the micro-system level), it is not enough to break the target bump through an impact, so it is mandatory to create a device able to transform the force produced by the actuation system into kinetic energy to be exploited by an impact. The first design proposed (ETA3) has been a hammer-like structure to provide an impacter against a target ("bump").

It is characterised by an extremity clamped to the substrate, with the other extremity free to move, starting in an equilibrium position really close to the "bump". During the pre-charge phase, it is dragged away by the actuator, storing elastic energy thanks to the stiffness of the body itself. Subsequently, it is released, transforming large part of the stored energy into kinetic energy and finally impacting against the "bump".

2.5.2. Chipping test devices: sling-like configuration (ETA4)

The second possible configuration is the "sling-like" testing structure. It has been designed to exploit the same functioning principle of the hammer, but exerting a better control on the rotations of the moving part.

It exploits the elasticity of the two beams connecting the central "bullet" and the anchors (see figure 2.22), to convert the displacement from the equilibrium position into kinetic energy. This mechanism creates a linear motion; indeed both the displacement and the "post-release run" act along the same direction (x-direction).
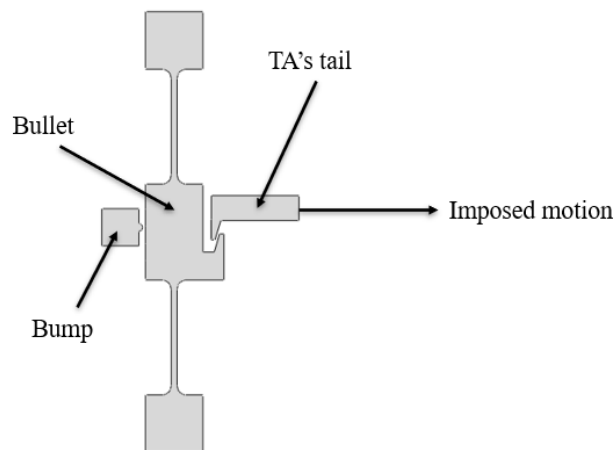
Figure 2.22: Schematic model of the sling structure design ETA4; most of the device is removed for clarity.

This release system has been designed to possibly reproduce multiple tests on the same device, thus a hook system has been built. It has been designed with an angle high enough to allow that the structure could self-detach: the two hooks can slide one respect to the other when horizontal displacement is applied. Another characteristic of this configuration is that the equilibrium position has been aligned to the center of mass of the entire bullet,

thus reducing the in-use rotations of the structure.

3 | Design of devices for on-chip mechanical tests

In the previous chapter the common parts among all the considered devices have been explained. As it has been previously anticipated in chapter 1, four different micro electro-thermo actuated devices have been considered. Despite the common actuation mechanism, these devices have different aims and have been designed with different features to better take advantage of their functionalities.

Depending on the mechanical testing procedure to be performed, the electro-thermally actuated V-shaped beams have been suitably designed in order to exploit either high forces or large displacements. Considering the first option, the devices in figure 2.1(a) (ETA1) and 2.1(b) (ETA2) have been considered; indeed, due to the high inclination of the beams ($\theta = 0 - 30°$ and $70°$ with respect to the shuttle side, respectively) high forces are generated at the expense of the maximum reachable displacement (as better explained in section 2.4). The structure in figure 2.1(d) (ETA4) has been conceived to exploit high forces too, but also to guarantee a horizontal motion of the device to "charge" the bullet. In order to obtain this goal, the beams have been designed with an inclination angle equal to $15°$, which has been predicted to achieve an experimental maximum displacement of $3.91 \ \mu m$ with an error of 1.3%. The resultant generated force ($F = k \cdot u$) has been also evaluated, since the stiffness of the moving part could become an issue if the horizontal actuator would has been not able to completely cope with the elastic response of the bullet. This force has been calculated, both with simulations and analytically, through the horizontal reaction forces acting on the anchored part of the bullet: it has been obtained to be $0.0135N$ from finite element (FE) calculations and $0.0099N$ from an analytical procedure (a less accurate approach). A completely different design has been considered for the ETA3: the inclination of the beams in this case is equal to $3°$, which allows a large displacement but low generated forces.

As detailed in the following sections, the behaviour of these devices has been firstly tested through FE multi-physics simulations, starting from an elementary structure and then moving to more complex modules, to have a first estimation of the performances of each

structure and also to have a comparison for analytical testing procedures.

3.1.   Simulations on elementary structures

In the first set of simulations, the voltage has been made to vary from 1 to 7 V, considering an inclination equal to $\theta = 20°$ for a single inclined beam. Under these hypotheses the displacement and the temperature fields have been investigated, focusing on the maximum and average reached temperature. The obtained results have been reported in table 3.1 and in figure 3.1.

Voltage [V]	Displacement $[\mu m]$	$T_{MAX}[K]$	T_{MEAN}
1	0.0433	329.74	318.11
2	0.1900	435.30	389.30
3	0.4315	584.43	486.05
4	0.7402	757.08	591.64
5	1.069	932.19	694.29
6	1.402	1110.18	790.94
7	1.715	1290.52	880.95

Table 3.1: Results of displacement, maximum and mean temperature as a function of the applied voltage for a sample inclined beam as heated by a DC voltage [9].

As reported in the figures 3.1(a) and 3.1(b), the dependence of temperature and displacement on the applied potential difference is basically linear, due to the dependence of both the electrical and thermal conductivity on the temperature.
Considering the heat transmission equation:

$$\rho_V c_v \frac{\partial T}{\partial t} - \nabla \cdot (k \nabla T) = \dot{Q}, \tag{3.1}$$

where ρ_V is the volume density of the material, c_v represents the specific heat, k is the thermal conductivity and $\dot{Q}$ is the generated thermal energy, neglecting the convection phenomena, in stationary conditions it becomes:

$$\nabla \cdot (k \nabla T) + \dot{Q} = 0. \tag{3.2}$$
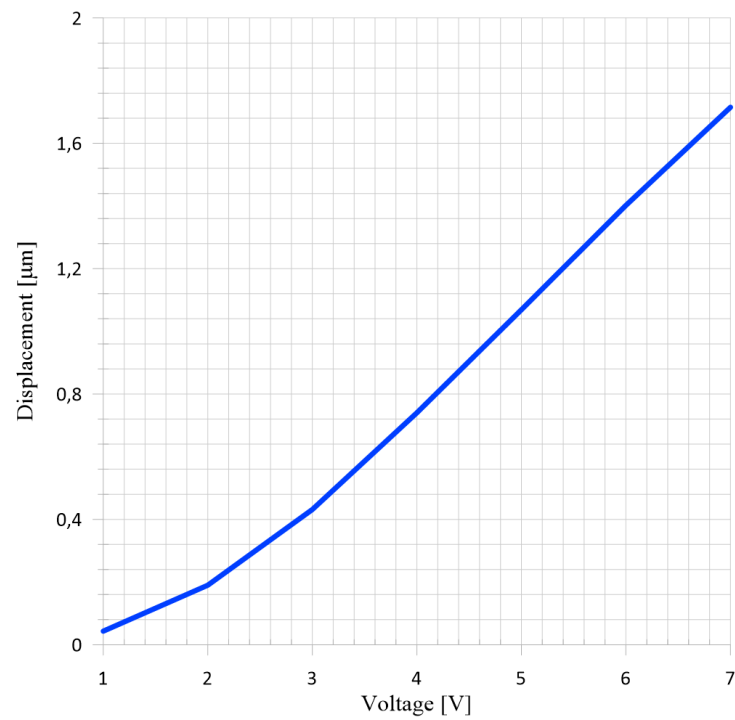
(a) *Plot of the displacement as a function of the applied potential difference for the inclined beam free end.*
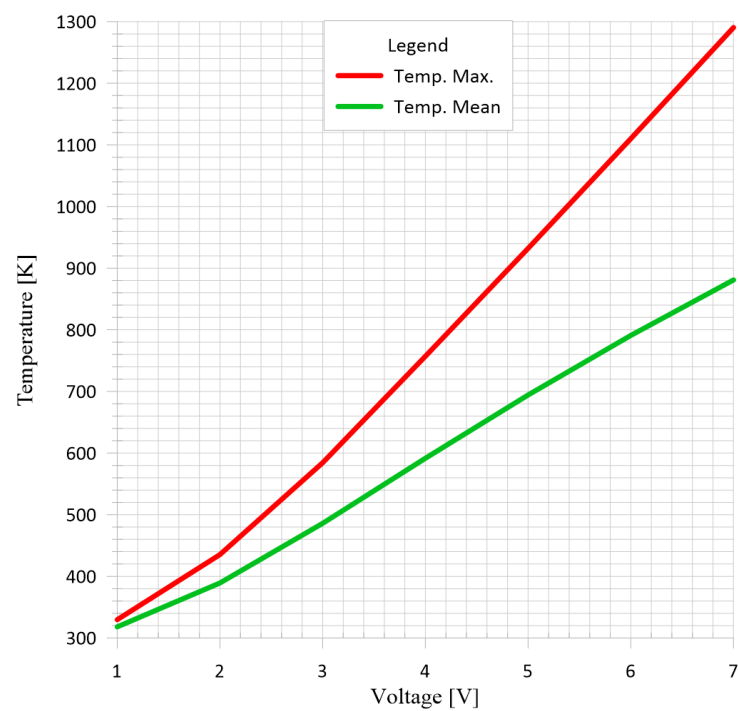
(b) *Plot of the maximum and mean temperature as a function of the applied potential difference.*

Figure 3.1

The thermal energy is generated as a result of the Joule's effect, which can be represented through the equation:

$$\dot{Q} = \dot{Q}_j = \sigma|\nabla V|^2, \tag{3.3}$$

where V is the potential and σ is the electrical conductivity. If this last parameter has been considered constant for rising temperature, then the heat generated would have assumed a parabolic evaluation, as will be assumed in further simulations in the chapter 5. However, in the following analysis, carried out in the work [9], both the thermal and electrical conductivity have been set as temperature dependents.

Simulations have been performed on the elementary structure depicted in figure 3.11, to examine the dependence of the displacement on the inclination (θ) of the actuation beams. First, a potential difference of 7 V has been imposed, under the hypothesis of small deformations; the obtained displacements, depending on the inclination angle, are reported in the table 3.2.

$\theta[°]$	Displacement [μm]
1	
2	
3	8.98
4	6.16
5	3.27
10	3.27
15	2.22
20	1.69
25	1.38
30	1.17

Table 3.2: Displacement for a varying inclination angle and an imposed voltage of 7 V, reported from [9].

A high value of deformation corresponds to small angles. On the other hand, a reduced generated force has been obtained for low angle values.

As a second set of simulations, to calculate the achievable force, a rectilinear sample with a known stiffness must be introduced (figure 3.2), then the generated force can be evalu-

ated through the formula:

$$F = k \cdot u, \quad k = \frac{EA}{L},$$

(3.4)

where E is the Young's modulus, A is the cross section of the sample and L its length, and u is the displacement.
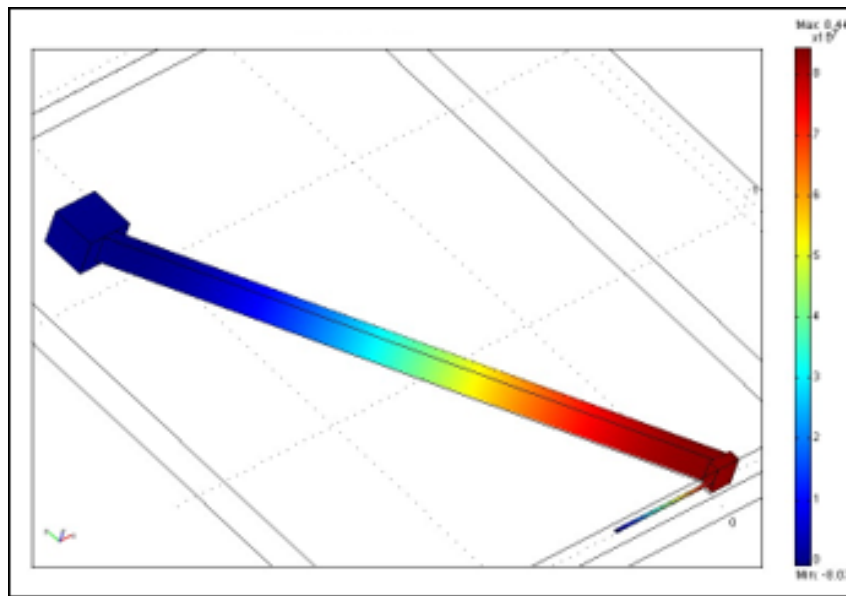
Figure 3.2: Model used for force calculation simulations ([9]).

For a given stiffness (2620 N/m) and geometrical values, the results achieved through simulations with a varying angle have been tabulated in table 3.3:

$\theta[°]$	Displacement $[10^{-1}\mu m]$	Force [mN]
5	11.20	2.93
10	14.40	3.77
15	13.61	3.57
20	12.00	3.14
25	10.50	2.75

Table 3.3: Results with respect to a varying inclination angle for a given sample stiffness equal to 2620 N/m, reported from [9].

These results correspond to the analytical values calculated through the equations described in the section 2.4.

3.1.1. Actuator sizing

The actuator is the part of the module which, thanks to the beams deformation due to the increase of temperature, drives the whole structure horizontally. The sizing and the geometrical features of the actuation system must consider the application of the MEMS; indeed, depending on the tests that must be performed, different values of displacement and generated force must be achieved.

For example, taking into account the ETA2, in order to break the specimen (thickness = 0.7 μm; E = 170 GPa) a stress equal to 3.5 GPa must be generated. Considering this data, the displacement required to reach the central fracture of the sample is 1 μm, therefore, due to the fact that the minimum width of the specimen is of 2 μm (the maximum over-etch value was considered), the required force to break it will be:

$$F = \sigma A = 3.5 \ GPa \cdot 0.7 \ \mu m \cdot 2 \ \mu m = 4.9 \ mN. \tag{3.5}$$

The temperature rising in the sample could be a possible cause of misfit between the theoretical hypothesis and the real working behaviour of the module, due to its dilatation and a consequent change in the geometrical parameters considered. To avoid or limit it, "heat-sinks" have been placed on the device to favour the warming of the central body, and to reduce the propagation of the generated heat from the actuation system to the sample. As it has been explained in the section 2.3, this configuration acts also as support for the whole device, and, thus, it should allow for its motion and ensure adequate deformations. This characteristic depends on the beam dimensions, more precisely on the length and on the width, while the out-of-plane thickness is fixed by the ThELMA process. During the design phase, a compromise between the length and the width must be reached, to obtain both a good efficiency in heat dissipation and in terms of beam stiffness.

Taking these considerations into account, the actuation system has been designed with five beams 300 μm long and 6 μm wide. As for the inclination depending on the purpose of the device, it has been set either to generate high displacements or forces.

Considering the ETA2, the figure 3.3 shows the dimensions of the actuation system.
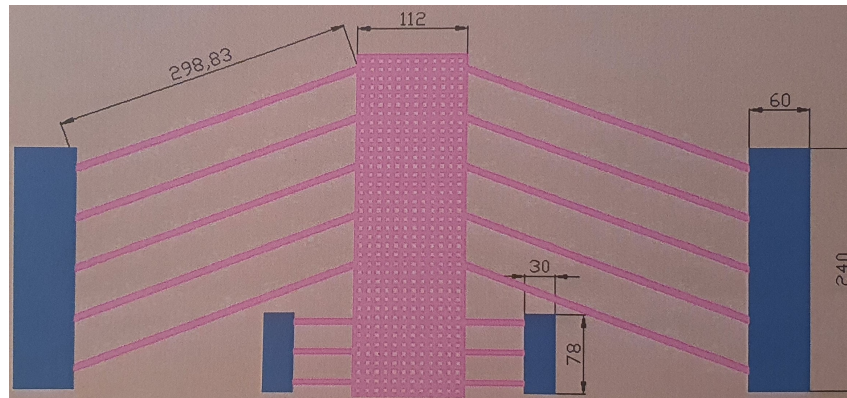
Figure 3.3: Sketch of ETA2 with the designed dimensions in μm ([9]).

3.2. Electro-thermal actuators for on-chip nanoscale tensile tests

This family of electro-thermo actuated devices includes the structures depicted in figure 2.1(a) and (b) (ETA1 and ETA2, respectively), both designed to perform axial tensile mechanical tests on a given sample. They load the specimen until rupture measuring the elongation through the capacitance variation of parallel plates capacitors, while the generated force could be computed by means of the quadratic relation with the applied voltage. The elastic stiffness and the nominal tensile strength of the device have been obtained by increasing the difference of potential till rupture, and then decreasing it to zero.

These two devices represent the evolution of structures with this aim presented in literature [6] [7]. For both of them, first an analytical estimation has been performed, followed by FE multi-physics simulations.

Both the devices have parts with a similar morphology, such as the capacitance sensors, designed by parallel plates capacitors, and the springs for heat dissipation and mechanical support (heat sinks), visible in figure 3.4.

In this section the testing procedure and the obtained results of the ETA2 are reported. In the figure 3.4 the designed and tested device (by [7] and [9]) is shown.
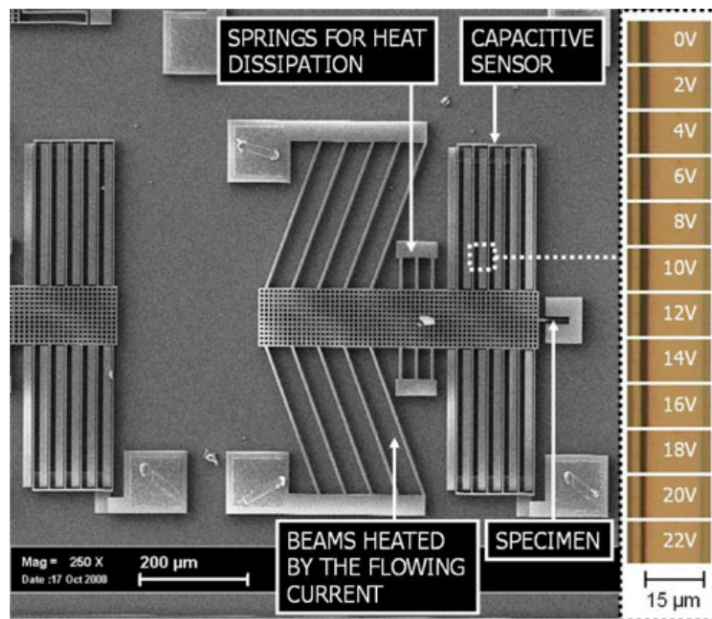
Figure 3.4: Device for tensile mechanical characterisation of a 0.7 μm thick Poly1 sample ETA2.

As a first step, the determination of the specimen elastic stiffness and nominal tensile strength have been carried out. The typical experimental procedure has been conducted in two phases: in the first one, the voltage has been raised from 0 V to 17 V through 0.25 V steps, applied between the ETA contacts. Therefore, the movable portion has been subjected to a monotonically increasing potential, which causes the generation of an axial force and the shuttle's horizontal displacement, measured by the parallel plate capacitors. The maximum voltage level has been chosen to cause the sample rupture. In the second phase, the voltage has been gradually reduced from 17 V to 0 V, keeping the same step used in the first phase. The only difference between the two phases has been that, in the second one, the measured displacement has been the one of the shuttle alone without the constraint represented by the sample, because it was broken in the previous phase.

In the figure 3.5, the achieved displacement as a function of the applied voltage is plotted, and the two subsequent phases can be easily distinguished, as the rupture event.
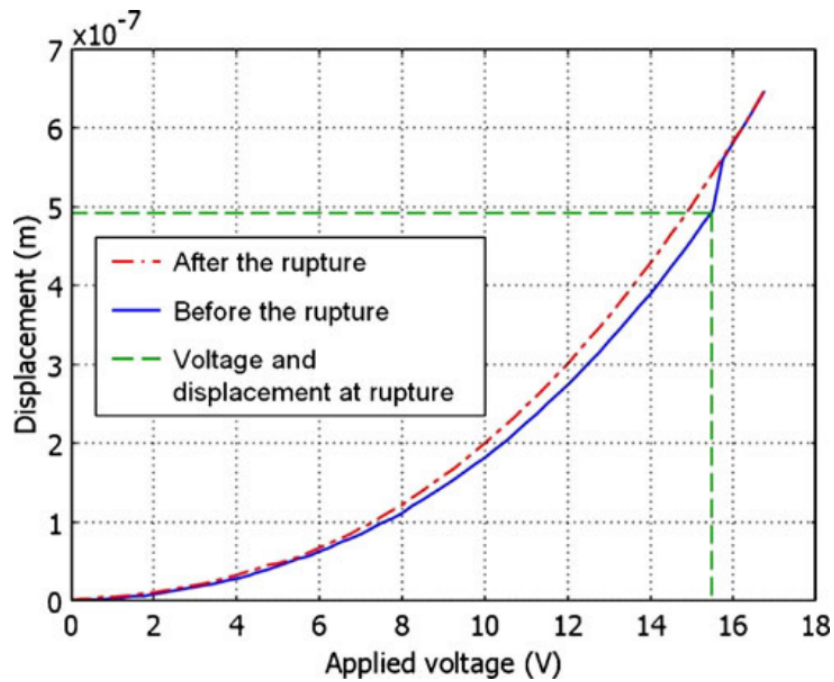
Figure 3.5: Experimental displacement vs. voltage plot [7].

It can be observed how, after rupture, the mechanical response abruptly changes, following a different displacement-voltage characteristic, defined by higher displacement values due to the reduced stiffness of the device, no longer constrained by the specimen [7]. As expected, the sample's rupture occurs in the central thinner portion, as it can be seen from the pictures taken with a scanning electron microscope (SEM), reported in the figures 3.6(a) and 3.6(b).
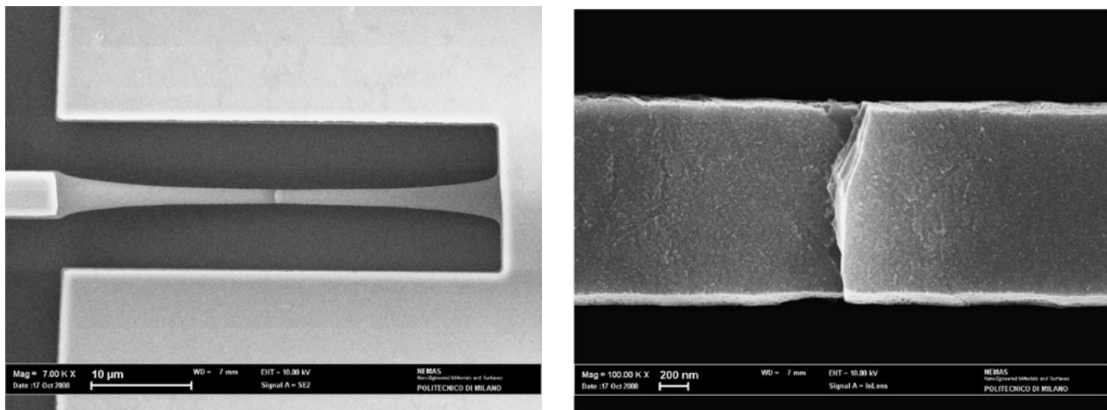
(a) *Overview*

(b) *Detailed view of the fractured sample*

Figure 3.6: Broken ETA2 specimen, images taken from SEM [7].

Under the hypothesis of linear elastic material till rupture, the stiffness of the sample can be evaluated from the difference between the two measured displacement values before and after the break, through the analytical model described in the section 2.4. On the basis of this model, the displacement values, d and d_0, respectively, can be expressed as:

$$d = \frac{2m\alpha\Delta T sin\theta EA}{mk_b + k + nk_{sTA}},\tag{3.6}$$

$$d_0 = \frac{2m\alpha\Delta T sin\theta EA}{mk_b + nk_{sTA}}.\tag{3.7}$$

In these two equations, m is the number of inclined pair beams, with an angle θ, having a stiffness equal to k_b. K_{sTA} represents the stiffness of n supporting springs and k is the sample stiffness. α is the thermal expansion coefficient, ΔT is the temperature variation generated inside the beams; E is the effective Young's modulus of the material composing the actuator (polycrystalline silicon), while A is the cross-section of the inclined beams. The specimen stiffness can be evaluated, by knowing the displacement of the device at a certain voltage difference before and after the rupture, through the equation:

$$k = (mk_b + nk_{sTA})\frac{d_0 - d}{d},\tag{3.8}$$

where the two stiffness values, k_b and k_{sTA}, can be evaluated through the equations 3.11 and 2.22. These two equations overestimate the real stiffness, due to the proportionality with respect to the the effective Young's modulus of the polysilicon used to fabricate the device (considered here to be a known parameter, but in reality it is reduced by temperature increases). Thus, through the equation 3.8 a higher stiffness value is achieved too, and, therefore, 3D FE models accounting for the temperature-varying properties have been built to verify the accuracy of these two equations.

The considered geometry, represented in figure 3.7, is formed by five beam couples, three spring couples and a Young's modulus value for the actuator equal to 143 GPa. Through this input data, a percentage difference of 5.6% has been obtained on the stiffness value of the beam, while an error value of 7.9% has been achieved, considering the specimen's stiffness calculation, by comparing the analytical results and the simulated ones. These results confirm the validity of equations 3.11 and 2.22 as a first approximation, but also emphasize the importance of simulations for a more exact estimation of the considered parameters.
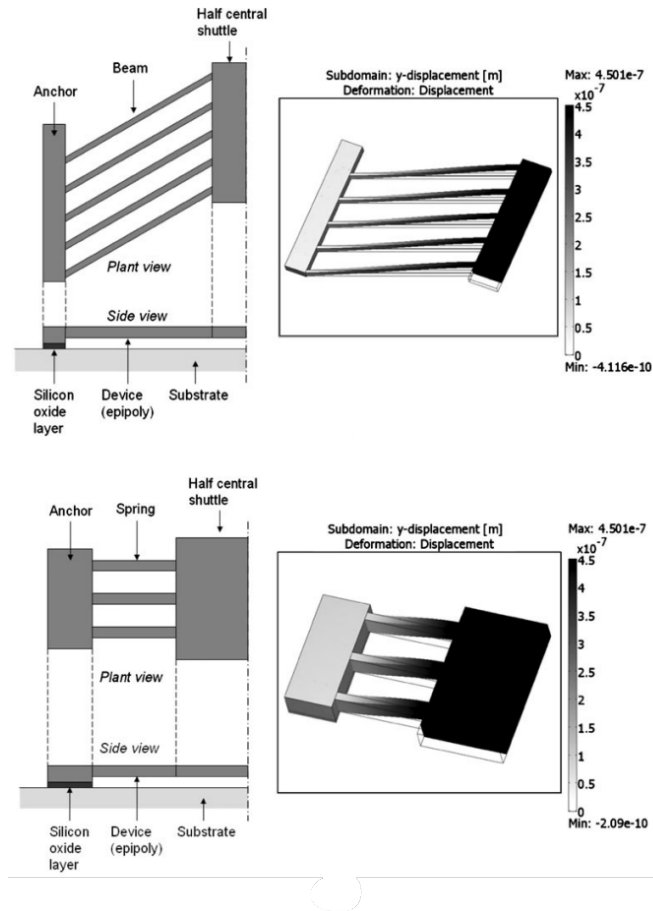
Figure 3.7: 3D FE model of ETA2: beams and heat sinks configuration [7].

It is important to point out that, for the specimen elastic stiffness calculation, a careful control has been carried out on the optimal operative voltage range. This procedure is required because of the dependence of k on the measured displacements, as indicated in equation 3.8. In figure 3.8 the results of 10 on-chip tests are represented. It must be noticed that in the voltage range $0 - 8$ V the noise, related to the small displacement achieved in this potential spectrum, does not allow to obtain reliable stiffness results. Hence, in order to perform k's calculations, the voltage range $8 - 14.5$ V, above which the rupture occurs, has been considered, and the result of an averaging procedure on the 10 on-chip tests of figure $3.8(a)$ is shown in figure $3.8(b)$, together with the standard deviation. From this plot the average value at varying voltage is 4.977 N/m with a standard deviation in the range of $94 - 376$ N/m [7].
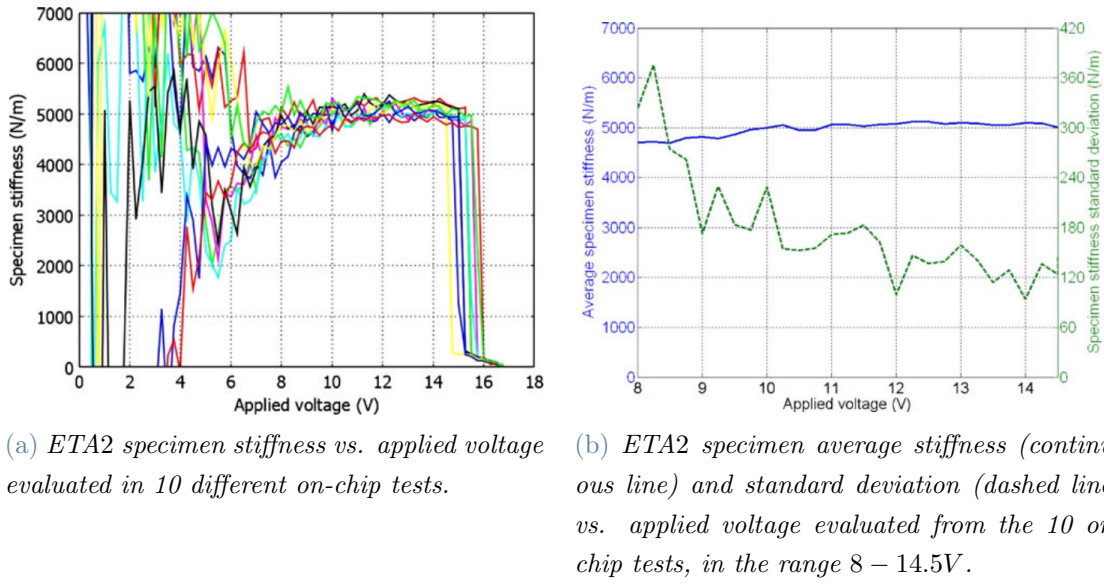
(a) *ETA2 specimen stiffness vs. applied voltage evaluated in 10 different on-chip tests.*

(b) *ETA2 specimen average stiffness (continuous line) and standard deviation (dashed line) vs. applied voltage evaluated from the 10 on-chip tests, in the range 8 − 14.5V.*

Figure 3.8: (*a*) ETA2 specimen stiffness evaluation in 10 different on-chip tests, and (*b*) representation of the standard deviation [7].

Once calculated the tensile specimen elastic stiffness, the specimen effective Young's modulus can be computed; the plot reported in figure 3.9 represents the result, as a function of the applied voltage, and the relevant standard deviation. It can be observed that the average value is in the range $165 − 180\ GPa$ with a standard deviation in the range $3 − 13\ GPa$; the average value at varying voltage being $175\ GPa$ [7]. This result fits well with the values present in literature, which give an average result equal to $174\ GPa$ ([4]).
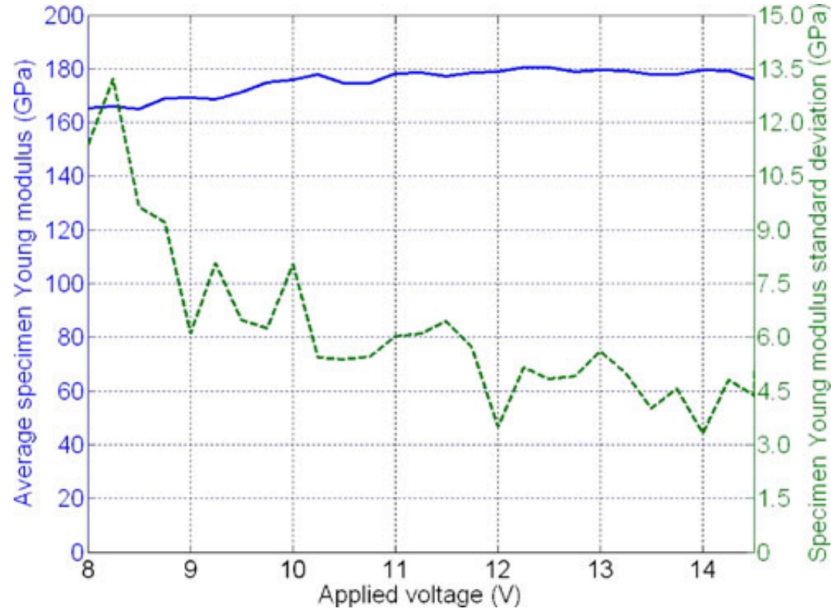
Figure 3.9: Specimen average effective Young's modulus (continuous line) and standard deviation (dashed line) vs. applied voltage evaluated from the 10 on-chip tests, in the range 8–14.5 V [7].

In the above relations, as for the determination of both the stiffness and effective Young's modulus are concerned, the temperature dependence has been neglected. This assumption has been motivated by a partial knowledge of the real dependence of polysilicon Young's modulus on the temperature and by the lack of measures of polysilicon effective temperature during the on-chip tests [7]. The consequences of this assumption can be seen in figure 3.8(b), in which the evaluated specimen stiffness k shows a slight increasing trend. This behaviour can be attributed to the Young's modulus reduction due to the temperature increase in the actuator portion of the device, caused by the Joule's effect. This phenomenon affects also the displacement achieved by the device, more precisely the value of d, thus the function $(d_0 - d)/d$ in the equation 3.8 increases with the reduction of E. Therefore, if equation 3.8 is used for the identification of the specimen stiffness k by considering constant the beam and springs' stiffness, k_b and k_{sTA}, during the test, thus disregarding their temperature variation for simplicity, the result is an apparent increase of the computed specimen stiffness, as shown in figure 3.8 [7].

3.3.   Devices for On-Chip Impact and Chipping Characterization of Polycrystalline Silicon

This class is formed by the devices depicted in figures 2.1(c) and (d) (ETA3 and ETA4, respectively); they represent the evolution in design to refine the testing procedure and perform the more accurate mechanical impact characterisation possible. The main differences between the two are related both to the different inclination angle of the V-shaped ETA and to the specimen testing configuration. This last feature has been improved, passing from the "hammer" to the "sling-like" configuration, in order to obtain a better control on the rotation of the moving part.

Both are composed by two different thermo-actuated structures: one is oriented along the horizontal direction and has the role of charging the "bullet" to let it acquire as much kinetic energy as possible; the other structure is blocked vertically and must provide the unhook, letting the bullet to collide against the target. This two-structure configuration allows repetitive tests on the same device, also modifying the applied voltage to change the generated force; indeed, the motion of the two devices can be manipulated in order to re-hook the bullet by the horizontal shuttle, if the performed experiment has not been carried out correctly.

One of the main objectives of this thesis concerns the testing procedure on the latest version of the ETA4 for impact and the chipping characterisation of polycrystalline silicon (using the "sling-like" device figure 2.1(d)) and, possibly, propose a modification in the design. The first step consists into performing mulyi-physics FE simulations to acquire data on the device behaviour.

In order to perform accurate simulations, firstly the physical problem must be described, namely the electro-thermo-mechanical coupled problem, that is the actuation process common to both the considered ETAs.

3.4.   ETA3: impact test device through hammer configuration

The first device realized, with the aim of the mechanical impact characterization of polycrystalline silicon, has been the one reported in the work [9].
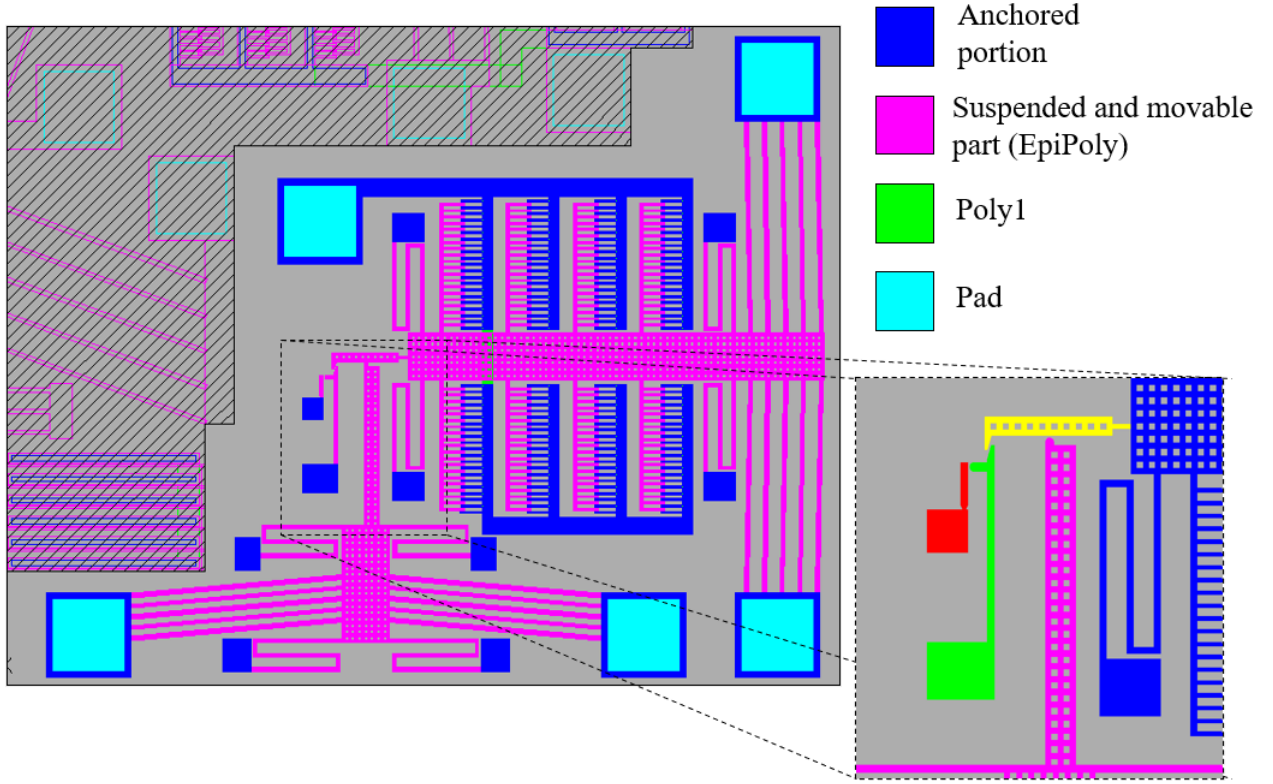
Figure 3.10: ETA3: prototype for mechanical impact characterization of polycrystalline silicon [9].

The module is made of by a V-shaped actuation system, chosen due to its versatility and to the possibility to generate a sufficient force for the tests performed.

This module has been designed with a beam inclination equal to $\theta = 1°$, which means that the operative motion of the shuttle is high, at the expense of the maximum reachable force.

As it has been explained in the section 2.4, through a purely mechanical analysis it is possible to infer the displacement caused by the thermal dilatation, obtaining the equation:

$$U^{\Delta T} = U_y = \alpha \Delta T l \frac{s}{\left(s^2 + c^2 \frac{12l}{AI^2}\right)} = \alpha \Delta T l \frac{s}{\left(s^2 + \frac{c^2}{\psi}\right)}, \tag{3.9}$$

where α is the thermal expansion coefficient, ΔT is the temperature difference in each actuation beam, having a section A and a length l. I is the moment of inertia with respect to the axis perpendicular to the substrate.

Considering the basic equation of elasticity and the Hooke's law $(F = ku)$, it is possible

to write an equation for the displacement when a general force is applied, thus:

$$U^F = U_y^A = \frac{F}{2(s^2\frac{EA}{l} + c^2\frac{12EI}{l^3})} = \frac{Fl}{EA}\frac{1}{2(s^2 + \frac{c^2}{\psi})},$$

(3.10)

therefore, the stiffness (k_b) can be evaluated as:

$$k_b = \frac{F}{U_y^A} = \frac{2EA}{l}(s^2 + \frac{c^2}{\psi}).$$

(3.11)

From the equation 3.11, the dependence of the elastic stiffness from the angle θ is evidenced; thus, as has been said, the horizontal motion is directly affected by the inclination of the actuation beams, together with the temperature generated.
Simulations have been carried on V-shaped modules, modelled to reflect the real geometry, considering all the fabrication limits (related to the ones of the ThELMA process developed by STMicroelectronics), which, in 2005, imposed a maximum thickness of 15 μm, modifying both the working conditions and the the geometrical features, such as the inclination angle and the length of the beams.
The considered structure is characterised by a beam length equal to 300 μm, while θ has been made to vary depending on the simulation set; it is depicted in the figure 3.11.
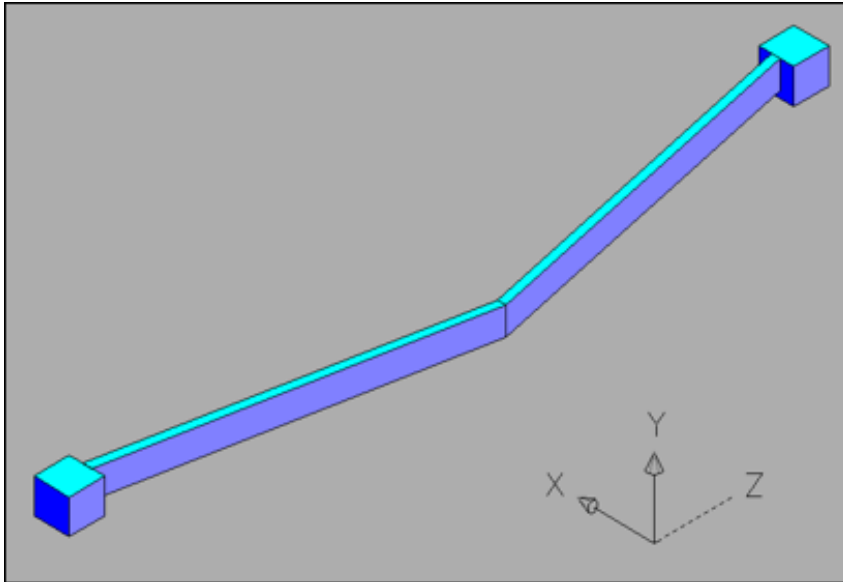

Figure 3.11: Structure considered for elementary simulations by [9].

After a short remark on the actuation mechanical working principle, the global module

can be considered. It has been fabricated to store as much potential energy as possible; it will be transformed into kinetic energy, letting the "hammer" structure free to collide against the target. The energy has been stored during the so-called "charging phase", bending the vertical rod (depicted in green in figure 3.10), thanks to the horizontal motion of the ETA; the hook in figure 3.10, placed in the extreme left portion of the shuttle provides the bending of the "hammer", when it is connected (in yellow colour in the figure 3.10). The release occurs thanks to the presence of the vertical ETA, which has been placed just below the hook, and, through its vertical displacement, bends the yellow tail. The charged "hammer" will collide against the target, i.e. the "bump" (coloured in red in figure 3.10). At the target connection with the anchor, a small groove has been manufactured, to facilitate its rupture during the experimental procedure.

The vertical ETA does not only provide the unhook phase, but it also allows test repetition, on the same device, if the procedure does not carry out the expected results; for example, if the imposed voltage is not as high as required to bend the hammer, it is possible to return back to the initial situation moving the vertical ETA and re-hooking the "hammer".

The horizontal shuttle has been designed with five couples of inclined beams, 300 μm long, which must provide a theoretical maximum allowable displacement of 20 μm.

3.5. Electro-thermo-mechanical coupled problem

The behaviour of the ETA involves the coupling between three different fields, in the electrical, the thermal and the mechanical domains. It is necessary to know how characteristic variables and parameters are distributed inside these physical domains, more precisely:

- the electric potential;

- the electric currents;

- the heat produced by the current flow;

- the thermal expansion of the material;

- the thermal deformation.

All these quantities can be calculated by solving the system of differential equations which describes the three coupled phenomena. Each of these problems can be set individually using the proper boundary conditions, combined with the constitutive equations of the considered phenomena.

As an example, the 15 unknowns (three displacement components, six independent strain

tensor components and six independent stress tensor components) of a general three dimensional mechanical problem can be calculated by setting the kinematic compatibility relations with suitable boundary conditions together with a material constitutive law.

The coupling with the other fields is obtained through the temperature increases ΔT assigned as inelastic strains through the coefficient of thermal expansion α, and the temperature-dependent definition of the elastic module for the polysilicon material. For the thermal problem, using the main principles of the heat conduction, in the general case of a continuous and homogeneous solid, the Fourier's law of conduction can be adopted, that reads:

$$q = -k \cdot grad(T). \tag{3.12}$$

It relates the spatial gradient of temperature, $grad(T)$, with the heat flux q through the thermal conductivity of the medium k. Combining this equation with the power balance of an infinitesimal volume of the continuum body, the Fourier's heat equation is obtained:

$$\nabla^2 T + Q_T = c_h \rho \frac{\partial T}{\partial t}, \tag{3.13}$$

where Q_T is the internal source of thermal power per unit volume (given by the Joule effect), c_h is the specific heat and ρ is the volume density of he material. The solution requires boundary conditions for the considered problem, such as:

- initial condition

$$T(x, t = 0) = T_0(x); \tag{3.14}$$

- convection boundary conditions, that relate the normal component (to the external surface) of the heat flux to the temperature difference between the surface and the reference value T_∞, far from the boundary

$$q(x, T)n = h(T - T_\infty); \tag{3.15}$$

- the radiation boundary conditions, that relate the component of the heat flux projected in the direction of the normal to the external surface to the difference between the fourth power of the surface temperature and that of the reference value T_∞

$$q(x, T)n = \epsilon\sigma(T^4 - T^4_\infty), \tag{3.16}$$

where ϵ is the emissivity of the body and σ is the Stefan-Boltzmann constant. Combining these relationships with the heat equation (3.5), the temperature distribution in the body can be obtained, solving the thermal problem.

Finally, the electrical field problem variables has to be stated. Since it is strongly coupled with the other fields, its discussion is left to the next section.

3.6. Coupling between the physical phenomena in an ETA

The following analysis is taken mainly from the Abaqus Theory Guide [1] and the Analysis User's Manual [22], and describes the coupling between the physical fields, with a particular focus on the numerical simulation.

Recalling the description of the three coupled phenomena, the different domains interact by means of two instances: with the generation of heat due to Joule effect, and with the thermal expansion related to the temperature increase.

The coupling between the electrical and temperature degrees of freedom arises from temperature-dependent material parameters and internal heat generation (Joule heating), which is a function of the electrical current density [22].

The first step in the resolution of this problem is the geometrical definition of the actuator's domain, where the differential equations, which describe the physics, will be solved. The chosen geometry for the actuator model is represented in the figure 3.12, and the first set of simulations has been effectuated focusing only on the horizontal thermal actuator, since it can be considered the main movable portion. The actuation part is formed by five couples of beams, attached at the right portion of the shuttle, also known as the "head", which generates the translation along the x-direction. Other important features are: the series of interdigitated comb-finger capacitors, which allow the motion sensing, and the four heat sinks, which favour the heat dissipation and act as mechanical support.
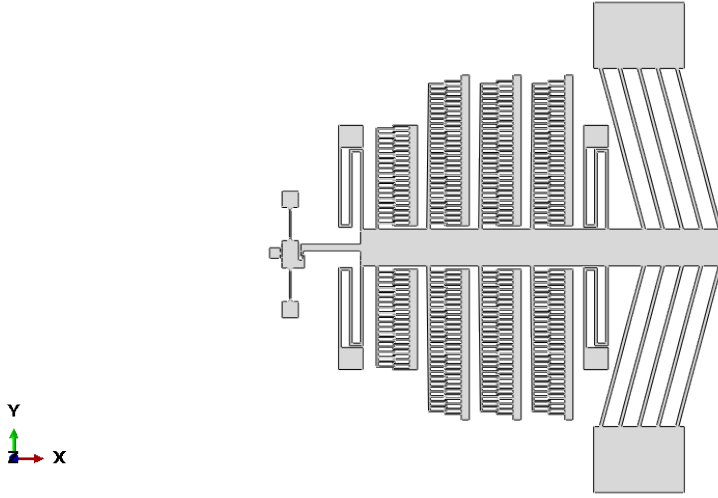
Figure 3.12: Abaqus model for the thermal actuator ETA4.

The subsequent step is the definition of the governing differential equations and their relative boundary conditions necessary for the problem resolution. Because the initial input is an external voltage, the electrical problem will be solved first.

The electric field in a conducting material is governed by the Maxwell's equation of conservation of charge. Assuming a steady-state direct current, the equation reduces to

$$\int_S \underline{J} \cdot \underline{n}dS = \int_V \underline{r}_c \, dV, \tag{3.17}$$

where V is control volume whose external surface is S, J is the electrical current density and r_c is the internal volumetric current source per unit volume [22].

Through the divergence theorem, the surface integral has been converted into a volume one, thus, considering an arbitrary volume, the differential equation has been provided point-wises:

$$\frac{\partial \underline{J}}{\partial \underline{x}} - \underline{r}_c = 0. \tag{3.18}$$

Introducing an arbitrary, variational, electrical potential field, $\delta\phi$, and integrating over the volume, using first the chain rule and, then, the divergence theorem, this equation can be written as

$$-\int_V \frac{\partial \delta\phi}{\partial \underline{x}} \cdot \underline{J} \, dV = \int_S \delta\phi\underline{J} \, dS + \int_V \delta\phi\underline{r}_c \, dV. \tag{3.19}$$

This causes a flow of electrical current described by the Ohm's law:

$$\underline{J} = \underline{\underline{\sigma}}^E \cdot \underline{E},$$ (3.20)

where $\underline{\underline{\sigma}}^E(T)$ is the electrical thermal dependent conductivity matrix and $\underline{E}(\underline{x})$ is the electrical field intensity along the current flow direction defined as

$$\underline{E} = -\frac{\partial \varphi}{\partial \underline{x}}.$$ (3.21)

Since a potential rise occurs when a charged particle moves against the electrical field, the direction of the gradient is opposite to the field. Therefore, combining the equations (3.9) and (3.10), the Ohm's law can be rewritten as:

$$\underline{J} = -\underline{\underline{\sigma}}^E \cdot \frac{\partial \varphi}{\partial \underline{x}},$$ (3.22)

Introducing this formulation into the conservation of charge equation (3.8), it becomes:

$$\int_V \frac{\partial \delta \varphi}{\partial x} \cdot \underline{\underline{\sigma}}^E \cdot \frac{\partial \varphi}{\partial \underline{x}} dV = \int_S \delta \varphi \underline{J} dS + \int_V \delta \varphi \underline{r}_c dV,$$ (3.23)

which describes the electrical problem.
The flow of electrical current is the cause of the temperature rising, thus the thermal problem can be described by the basic energy balance relationship:

$$\int_V \rho \dot{U} \delta T dV + \int_V \frac{\partial \delta T}{\partial \underline{x}} \cdot \underline{K} \cdot \frac{\partial T}{\partial \underline{x}} dV = \int_V \delta T r dV + \int_S \delta T q dS,$$ (3.24)

V is a volume of solid material, with area S; ρ is the density of the material; U is the internal energy; K is the thermal conductivity matrix; r is the heat generated within the body; q is the heat flux per unit area of the body, which can be evaluated, considering two radiative points A and B, through:

$$q = F[(T_A - T^Z)^4 - (T_B - T^Z)^4],$$ (3.25)

where T^Z is the value of absolute zero temperature on the adopted temperature scale; q is the heat flux per unit surface area crossing the gap at this point, from surface A to

surface B; T_A and T_B are the temperature of the two surfaces, and F is the gap radiation constant derived from the emissivity of a surface and from the Stefan-Boltzmann constant $(5.67 \cdot 10^{-8} W/(m^2 K^4))$.

The coupling between the electrical and the thermal problem derives from the temperature dependence of the electrical conductivity, $\sigma^E = \sigma^E(T)$, and from the current dependence of the heat generation rate $r = r(J)$.

More precisely, the electrical current dissipation (namely the power P_{ec}), due to the current flowing in the semiconductor, is transformed into heat power (P_h). It is assumed in first approximation the totality of the electrical dissipation is transformed in heat, so $P_{ec} = P_h$.

This is described by the Joule's law as:

$$P_{ec} = E \cdot J, \tag{3.26}$$

which, recalling (3.11), is rewritten as

$$P_{ec} = \frac{\partial \varphi}{\partial x} \cdot \sigma^E \cdot \frac{\partial \varphi}{\partial x}. \tag{3.27}$$

As already mentioned, the Joule heating effect gives rise to thermal strains, causing the motion; considering a material with thermal isotropic behaviour, the thermal strains can be defined as

$$\varepsilon_T^T = [\alpha \Delta T \ \ \alpha \Delta T \ \ \alpha \Delta T \ \ 0 \ \ 0 \ \ 0], \tag{3.28}$$

where α is the linear coefficient of thermal expansion.

In a linear isotropic material, thermal strains can be then related to the stresses as:

$$\sigma = D(\varepsilon - \varepsilon_T), \tag{3.29}$$

where D is the stiffness matrix of the material.

Others thermal phenomena exist and could influence the mechanical performances of the device, such as the fast volumetric deformation, but they are not considered in this work, since their contribution in elastic solids is usually neglected.

4 | Numerical simulations

Multi-physics 3D finite elements simulations are the first step in the device's characterization. Indeed, since the solving methodology has been described in chapter 3, it is possible here to go more in details in the simulations carried out and their results. To obtain simulations duplicating the real device behaviour, the setting procedure is fundamental, and it is presented in detail in the following sections.

It is important to recall again the physical principle of ETA: the applied input voltage will cause a temperature gradient along the inclined beams, and their subsequent deformation, which involves the planar motion of the whole shuttle.

4.1. Parameter setting

To simulate this coupled problem, the temperature dependence has been considered. The software continuously adapts the model response to the rise in temperature caused by the potential difference applied, and more realistic responses are therefore considered. The solution is obtained by solving a system of differential equations, describing the relevant phenomena occurring, such as: electromagnetism, heat propagation, and deformation induced by thermal stresses in an elastic continuum (see chapter 3 for the governing equations in the mathematical problem).

The aim in the following sections is therefore to define the temperature dependent properties, in a range just below the melting point of the polysilicon ($1414\,°C$). In particular, the temperature dependence of the following silicon's intrinsic properties must be known: thermal conductivity (k), electrical conductivity (σ), specific heat (C_p), emissivity (ϵ) and thermal expansion coefficient (α_T).

4.1.1. Thermal conductivity

The local temperature-dependent thermal conductivity of the doped polysilicon layers is modelled by an approximate solution of the Boltzmann transport equation for phonons, which uses frequency-dependent relaxation times to represent phonon scattering events [19].

The thermal conductivity is mainly dominated by phonon conduction. Mobile carriers, introduced by doping procedure, can also contribute in increasing this property. On the other hand, significant factors that impede the phonon transport include phonon-phonon scattering, impurities such as dopants, and grain boundaries within polysilicon.

If the material is considered isotropic, a general form of the thermal conductivity is given by the Boltzmann transport equation:

$$K = \frac{KB}{2\pi^2 v} \frac{KB^3}{\hbar^3} T^3 \int_0^{\frac{\theta_D}{T}} \tau_c \frac{y^4 e^y}{(e^y - 1)^2} dy. \tag{4.1}$$

In this form, KB is the Boltzmann constant, $\hbar$ is the Planck constant, θ_D is the Debye temperature, v is the averaged phonon velocity in silicon and τ_c is the relaxation time, which has contributions from the factors that impede phonon transport. The nondimensional parameter y is defined as:

$$y = \frac{\hbar\omega}{KB \cdot T}, \tag{4.2}$$

where ω is the phonon frequency, which rises with temperature and explicates the frequency dependence of the thermal conductivity [10]. However, for the purposes of this work, the thermal conductivity has been considered constant and equal to 34 W/mK, according to [5]. This assumption is also supported by [17]: assuming a small grain size and high dopant concentration (in the order of 10^{20} $atoms/cm^3$), the temperature dependency of the thermal conductivity of polysilicon is not a dominant factor.

4.1.2. Electrical conductivity

Dopant concentrations have a significant impact on the temperature dependent conductivity polysilicon. Furthermore, grain boundaries exhibit charge carrier trapping and contribute to the temperature dependent behaviour. Undesired instability effects could be generated for low doping levels. Thus, dopant levels for thermal actuators are generally high, where the electron and hole scattering, arising from thermal vibrations, dominate effects deriving from increases in charge carrier concentration.

This results in a positive temperature coefficient of resistance, and this linear increase has been used as a general resistivity model [10], represented in figure 4.1.
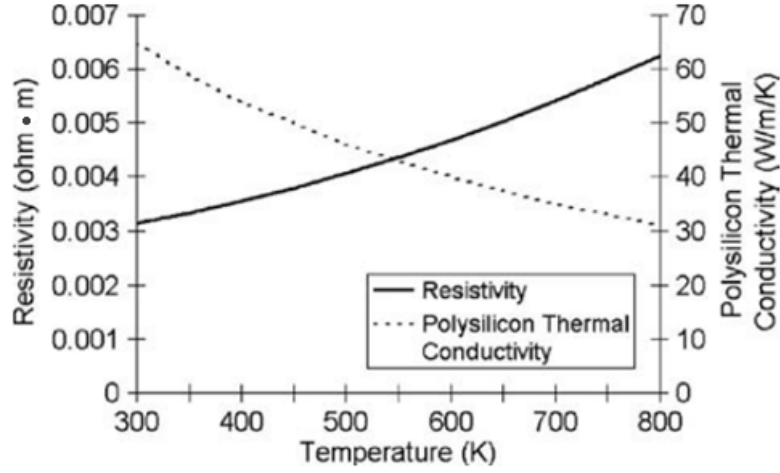
Figure 4.1: Temperature dependence of polysilicon electrical resistivity and thermal conductivity [6].

Starting from these considerations, the electrical resistivity, evaluated in $[ohm \cdot m]$, can be evaluated through the following equation:

$$\rho = 3.4 \cdot 10^{-5}[1 + 1.25 \cdot 10^{-3}(T - 293)]. \tag{4.3}$$

Therefore, by reversing this equation, the dependence on temperature of the electrical conductivity can be determined.

4.1.3. Thermal expansion coefficient

This parameter, necessary to simulate the optimal displacement of the thermo-actuator, has been measured in the temperature range 273 K to 1,433 K through several procedures, such as an interferometric dilatometer, X-ray diffractometry and others [18]. The empirical measurements match the following analytical expression:

$$\alpha(T) = 3.725(1 - e^{-5.88 \cdot 10^{-3}(T-124)}) + 5.548 \cdot 10^{-4}T, \tag{4.4}$$

where the temperature varies in the above mentioned range.
The adopted values, computed through this formula, are plotted in figure 4.2.
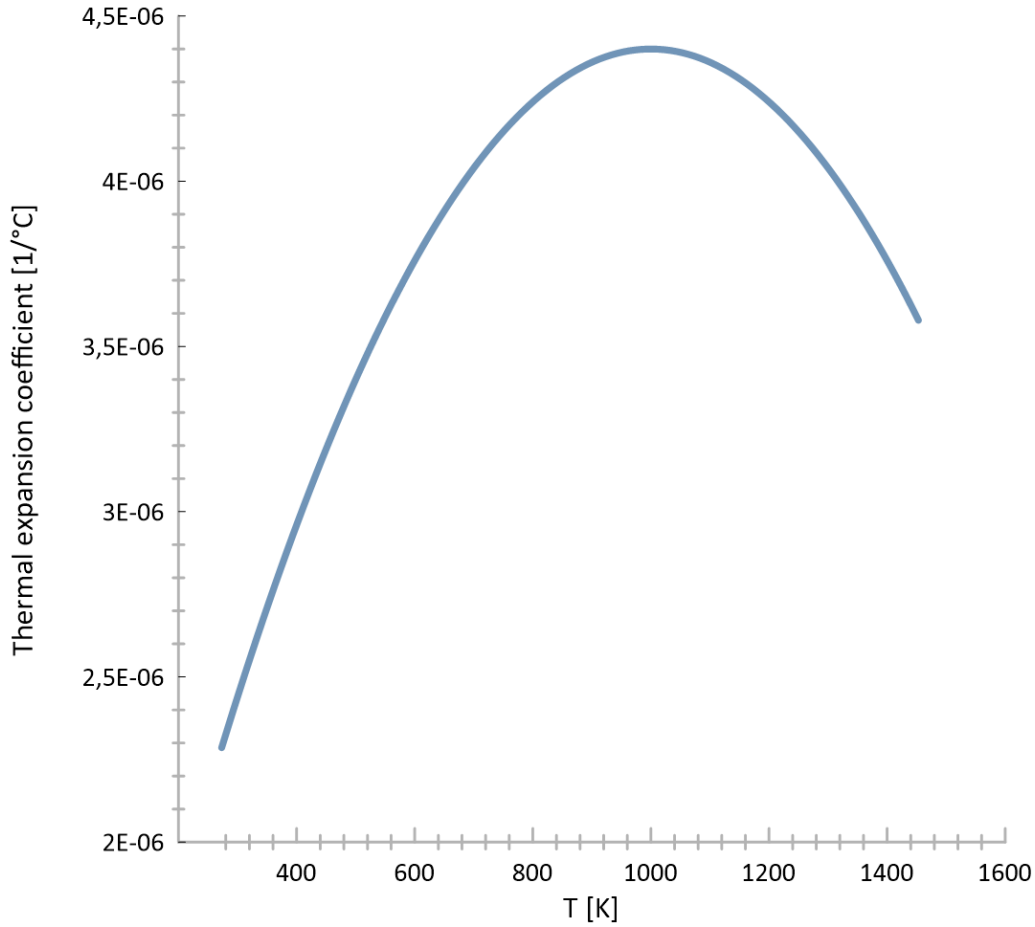
Figure 4.2: Polysilicon thermal expansion coefficient as a function of the temperature.

4.1.4.   Specific heat

Polysilicon specific heat at constant pressure is governed by the phonon's vibration modes, thus it is possible to consider the heat capacity as temperature dependent.

The Debye theory of heat capacity crystals is used to calculate the temperature dependence specific heat as:

$$C_p = 9\frac{R}{A}\frac{T^3}{\theta_D^3}\int_0^{\frac{\theta_D}{T}}\frac{y^4 e^y}{(e^y-1)^2}dy, \tag{4.5}$$

where R is the ideal gas constant, A is the atomic weight for silicon, θ_D is the Debye temperature and y has been defined in equation 4.2 . The values considered in the simulations are reported in table 4.1: starting from the ambient temperature, the value increases constantly for increasing temperatures. Due to this reason, a constant rise of this parameter, till the melting temperature, has been verified and then assumed.

$C_p[J/(kg \cdot K)]$	T[K]
730	300
840	400
850	500
860	600
870	700
880	800

Table 4.1: Temperature dependence of the specific heat at constant pressure for polysilicon.

4.1.5. Emissivity

Emissivity is related to the effectiveness in emitting energy as thermal radiation. It is defined as the ratio between the radiance of a given object and the one of a black body at the same temperature.

Thus, for this work purposes, it is the main cause of temperature losses which directly affects the maximum reachable displacement. This agrees both with articles present in literature, such as [17], and with the simulations, which confirm the negligible dependence of the response on other thermal dissipation phenomena.

There have been several studies of the thermal radiation emitted by silicon at elevated temperatures, but, since silicon emissivity strongly depends on many factors, such as the sample thickness, doping and surface conditions, experiments must be interpreted with care, before applying one of the various measured silicon emissivity values to any kind of model. As first approximation, an emissivity acceptable for the different experimental results is null at room temperature, then rises smoothly with temperature to a maximum value of 0.7 at 1,220 K [18].

4.2. Temperature effects on the mechanical properties

For a complete discussion about the parameters varying with temperature, also the effective elastic modulus must be considered. A theoretical discussion could be done consid-

ering [14] and [18].

4.2.1. Elastic modulus

The most general situation considers an anisotropic material, and, in this case, elasticity is defined as the proportionality constant, in the Hooke's law, between stress (σ) and strain (ε) and it characterizes the stiffness of an elastic material. For the uniaxial case, it is:

$$\sigma = C\varepsilon \tag{4.6}$$

$$\varepsilon = S\sigma. \tag{4.7}$$

In an anisotropic material, the Hooke's law involves a fourth rank tensor to describe the elastic relationship between the second rank stress σ_{ij} and strain ε_{ij} tensors:

$$\sigma_{ij} = C_{ijkl}\varepsilon_{kl} \tag{4.8}$$

$$\varepsilon_{ij} = S_{ijkl}\sigma_{kl}. \tag{4.9}$$

Fortunately, in silicon, the combination of cubic symmetry and the equivalence of the shear conditions allow to specify the fourth rank tensor with only three independent components [14].

From a quantum physics point of view, the elasticity of a material is represented by the interaction forces between its constituent atoms, and it can be evaluated from quantum theory as the strain derivative of the crystal energy.

Analytically, it can be measured from the slope of the linear portion of the stress-strain curve, recorded from an experiment where the specimen undergoes to a uniaxial load. More accurate measurement could be performed involving acoustic wave propagation in the solid, as reported in the table 4.2:

C$_{11}$	C$_{12}$	C$_{44}$	S$_{11}$	S$_{12}$	S$_{44}$
165.65	63.94	79.51	7.9	-2.14	12.6

Table 4.2: Elastic constants in silicon at $298K$ (units are: for C $10^9 Pa$, for S $10^{-12} Pa$) [18].

Through the constants measured in this way, it is possible to calculate the Young's modulus versus the crystallographic orientation, as depicted in figure 4.3.
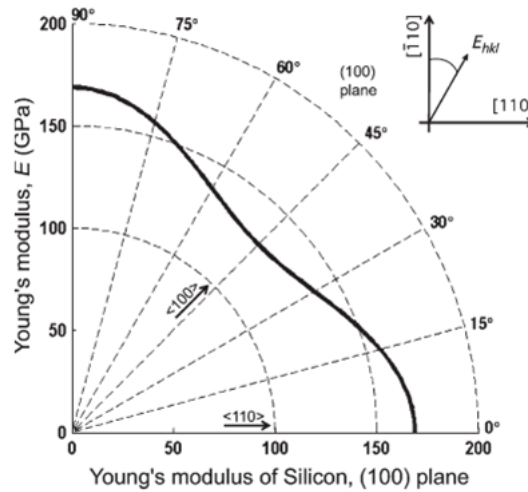

Figure 4.3: Value of Young's modulus versus the orientation of the elastic axes in silicon.

Otherwise, the Young's modulus E along a generic direction can be calculated from the general formulae for a cubic crystal:

$$\frac{1}{E_{hkl}} = s_{11} - 2[(s_{11} - s_{12}) - \frac{1}{2}s_{44}](m^2 n^2 + n^2 p^2 + m^2 p^2) \qquad (4.10)$$

where m, n, p are the "direction cosines", i.e. the cosine of the angle between the $[hkl]$ direction and the three axes of elasticity [14]. The thermal dependency is described through the Thermal Coefficient of Elasticity (TCE) with respect to the considered elastic constant. More precisely, the thermal variation is calculated with a power series of $TCE(C)_k$'s coefficients:

$$C(T) = C(T_0)[1 + \sum_{k>=1} TCE(C)_k(T - T_0)^k] \tag{4.11}$$

where C is a generic elastic constant. The most accurate performed experiments come from the research of Bourgeois et al. [3], whose values include the second order temperature coefficients and are reported in table 4.3:

TCE	n-type $(0.05\Omega \cdot cm, P)$	n-type $(0.05\Omega \cdot cm, P)$
	First-order (x $10^{-6}/K$)	Second-order (x $10^{-6}/K^2$)
TCE_{s11}	63.60 $\pm$0.60	60.51 $\pm$0.35
TCE_{s12}	45.79$\pm$2.80	75.70 $\pm$6.10
TCE_{s44}	57.96 $\pm$0.17	57.31 $\pm$1.40

Table 4.3: Temperature coefficients for the elastic constants [18].

In this thesis, due to the hypothesis of an effective isotropic material for polysilicon, the Young's modulus has been calculated as the mean value between E_{100} and E_{110} (calculated though equation 4.10), taking into account, for each constant, its temperature dependence. The effect in the crystallographic plane [111] has not been taken into account due to the interest into the mechanical properties for the x-y plane only, where the shuttle motion occurs. The obtained values are plotted in figure 4.4.

Another simplification has been to neglect the doping effects on the elastic constants. This is, supported by [14], due to the small changes in the effective Young's modulus (1% -3%) for heavy doping levels.
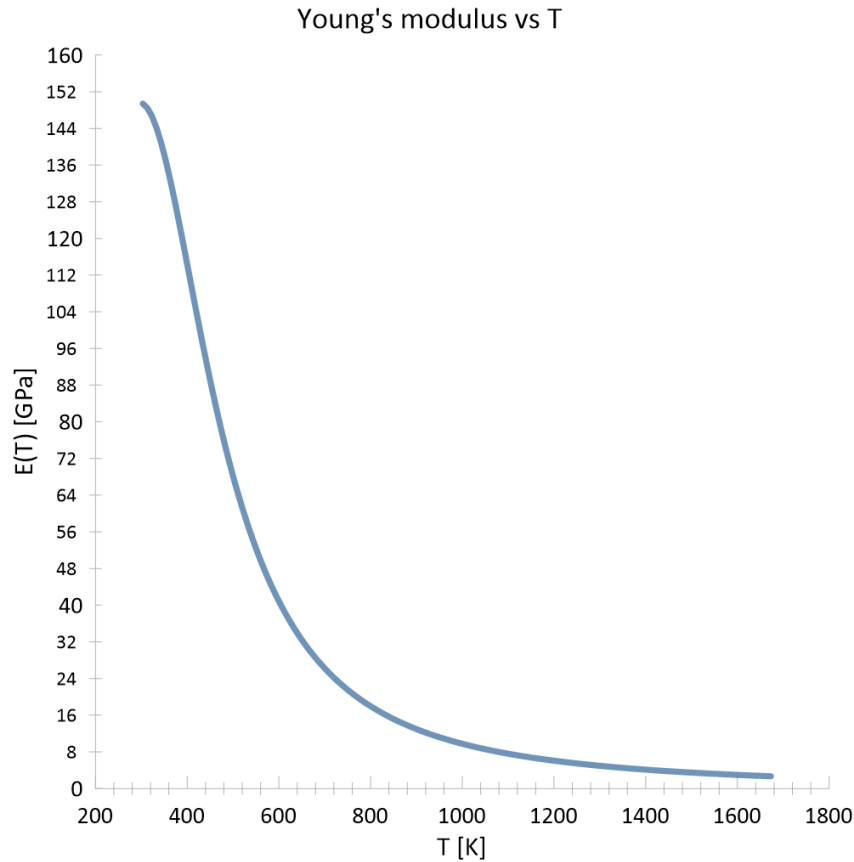
Figure 4.4: Effective, in plane Young's modulus as a function of the temperature for polysilicon.

4.2.2. Brittle to Ductile Transition

Silicon is a brittle material at room temperature, thus the crack propagation is not affected by any significant plastic deformation. Nevertheless, a ductile behaviour is observed above a given temperature T_{BD}, for given loading rate and doping level.

From the literature, silicon shows a characteristic sharp brittle-to-ductile transition. This transition occurs over a very narrow temperature range, typically less than 10 K (see figure 4.5). The microscopic studies of the fractured samples have shown that there is dislocation activity at the crack tip below the brittle-ductile transition temperature: a few hundred dislocations can be seen from the crack, moving into the bulk, along well-defined crystallographic directions when approaching T_{BD}, and a huge amount of dislocations nucleate above the critical temperature T_{BD} [18].
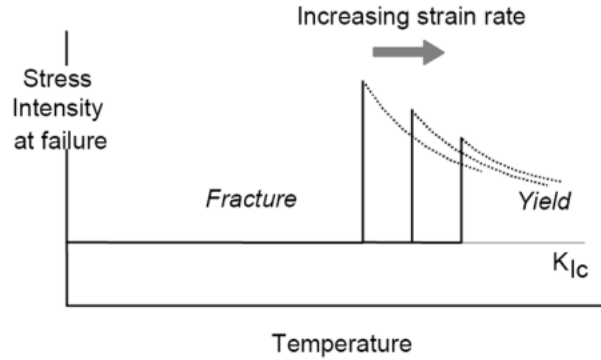
Figure 4.5: Brittle-ductile transition in silicon. The stress intensity at fracture rises abruptly at T_{BD} [18].

The results are strongly affected by the testing method and that n-type dopants decrease the brittle-ductile transition temperature. These experiments have determined T_{BD} as a function of the activation energy for the brittle-ductile transition U_{BD} [18].

$$\dot{K} = A \cdot exp(\frac{-U_{BD}}{KBT_{BD}}) \qquad (4.12)$$

where A is a model constant, the stress intensity at failure and KB is the Boltzmann constant. U_{BD} was measured to be 1.6 eV for n-type silicon by [21].

A quantitative model for the brittle-ductile transition of silicon has been proposed by [12][13], in which the competition between the shielding of the crack front (by dislocation) and the rising of the stress intensity factor K_I to the critical value K_{IC}, is described.

The main feature of the model is that the material becomes ductile only when the emitted dislocations shield every point of the crack front. In this sense, the mobility of the dislocations plays the major role in this model [18].

4.3.   Thermal-simulations

The first physical field that has been investigated is the temperature increase from the electro-thermal coupled problem. This analysis has been performed through multi-physics FE simulations using the software Abaqus, under a steady-state hypothesis, combined with boundary conditions, and temperature as a free variable.

A time-independent benchmark problem for a single polycrystalline silicon beam has been first carried out, comparing analytical and simulated results. The analytical procedure has been extracted from [15]. This calculation, subjected to the assumption of neglecting

all types of thermal losses and of a 1 mm-long beam, has been performed by imposing a voltage at one extreme of the rod and leaving the temperature free to vary in the whole sample. The analytical solution is determined through the equation:

$$T = T_{\text{inf}} + (T_b - T_{\text{inf}}) \cdot e^{-mx}, \tag{4.13}$$

where $m = \sqrt{\frac{4h}{kD}}$, h is the convection coefficient, k represents the thermal conductivity, while D defines the diameter of the rod.

From the simulations, an exponentially decreasing temperature has been also observed along the beam length, reported in the figure 4.6, confirming the correct procedure for the thermal simulations.
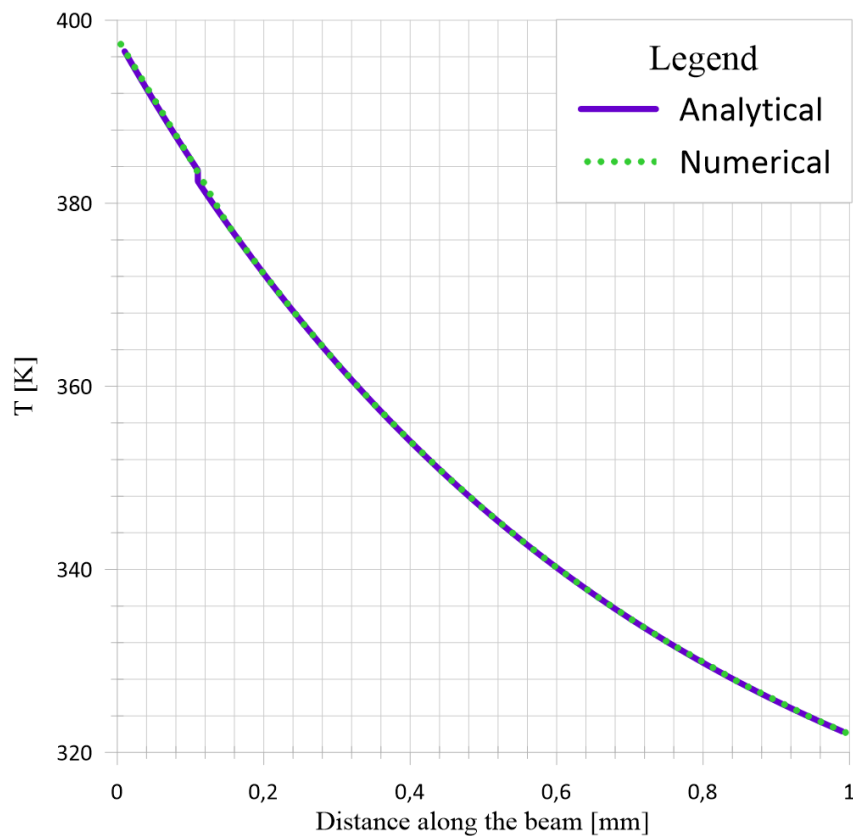

Figure 4.6: Temperature distribution for a single beam subjected to a thermal gradient.

Finally, simulations on the device have been performed, setting as the driving force the voltage difference at the two big pads of the horizontal thermal-actuated device (see figure 4.7), allowing the beams' deformation and, therefore, the device movement. The second condition imposed has been the prescribed initial temperature, equal to 298 K, in corre-

spondence of the anchor of the heat sinks. This is an approximation of the real behaviour of the sinks. The other boundary conditions are both related to the thermal dissipation phenomena, more precisely to the convection and to the surface radiation. From the performed simulations, and in accordance with [17], the effects of convection are negligible compared to the other temperature dissipation phenomenon: indeed, it reduces the rising temperature only of a few Kelvin degrees. These interactions (convection and radiation) are both applied to the upper part of the devices, neglecting the lateral and bottom surfaces: due to the small thickness of the device (24 μm) and to the narrow air gap which separates the movable portions to the substrate, it is a reasonable assumption.

(a) *Pads, on which the potential difference has been applied.*

(b) *Anchorage on which $T = 298K$ has been fixed.*

(c) *Top surface of the shuttle, responsible of thermal dissipation.*
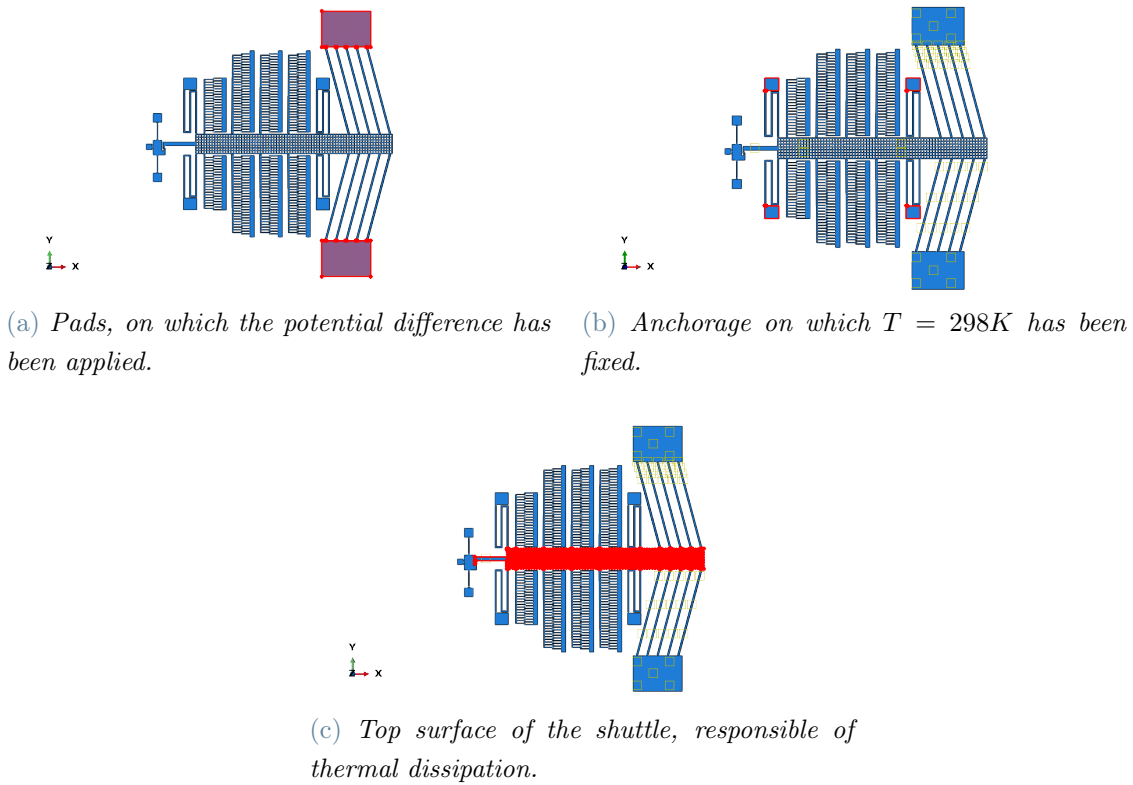
Figure 4.7: Device parts which the BCs have been applied (highlighted in red colour).

Using this setup, a temperature distribution confined along the V-shaped beams and in the right portion of the shuttle, the "head", has been obtained for all the applied potential differences. Cross analyses between the potential and emissivity values have been performed. For each voltage, five different emissivity values have been considered, allowing to characterise the temperature spectrum for different dissipation intensities.
More precisely, the values have been the following:

$$Emissivity = 0.10/\,0.21/\,0.35/\,0.49/\,0.65 \tag{4.14}$$

Independently from the temperature magnitude, its qualitative profile has resulted to be almost the same and it is depicted in figure 4.8.
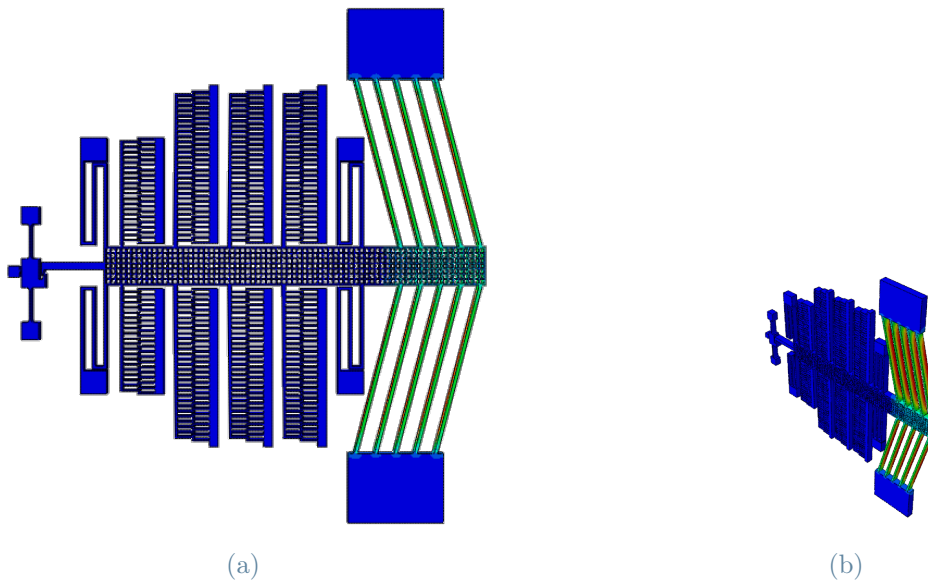

(a)   (b)

Figure 4.8: Temperature profile of the horizontal shuttle, (a) top and (b) lateral.

These temperature profiles are completely different with respect to the ones predicted [2] on the same device. In the previous studies, through 2D simulations at $5V$ with constant emissivity, equal to 0.65, a temperature distribution in the whole device has been obtained; the maximum values have been found to be in the right portion of the device shuttle and correspond to $1,191K$, while the average beam temperature is about $854K$, as it is represented in figure 4.9.
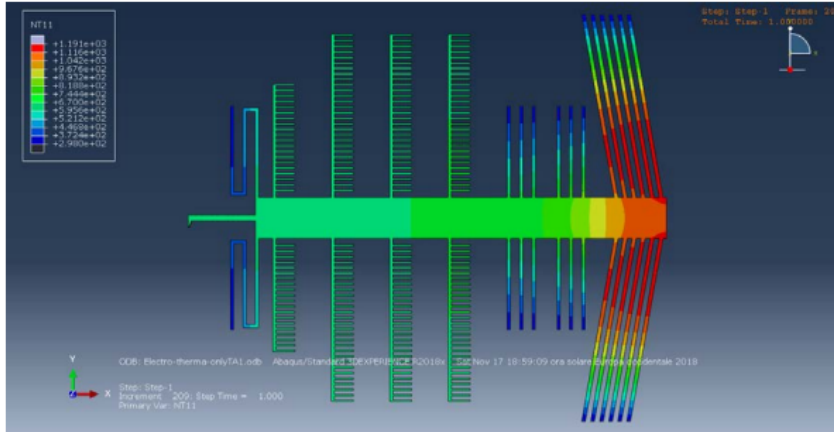
Figure 4.9: Temperature distribution of the first set of 2D electro-thermal simulations performed in [2]

This result is not comparable with the simulations carried out on the 3D modelled device in the present work. Indeed, the maximum reached temperature in this case is $865K$ at $25V$. Obviously, due to the close relationship between temperature and displacement, this outcome anticipates also a lower horizontal device motion.

4.4. Coupled thermo-electrical-structural simulations

After running the thermal simulations, the coupled thermo-electrical-structural problem has been carried out. Differently from the previous simulations, these analyses do not assume the steady-state hypothesis, but are performed in transient regime; thus, the time interval in which the tests will be carried out must be defined. It has been determinate as the time the temperature takes to reach a constant value, and, therefore, the time in which the maximum displacement is reached.

Simulation results in figure 4.10 show that the time required to reach a constant temperature, independently from the applied voltage difference, is about 75 μs; thus, the time interval considered in the following simulations has been imposed conservatively equal to 100 μs, and all the contour plots will refer to the end of the analysis, when the steady state condition has been reached.
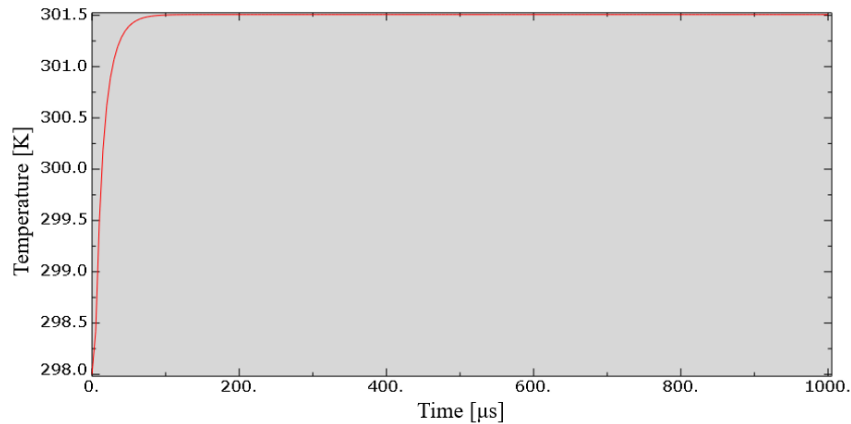
Figure 4.10: Evolution of temperature with time, which highlights the time required to reach the steady state condition.

After these introductory remarks, the focus shifts on performing simulations to control the device operation. In order to do that, simulations that couple both the electro-thermal behaviour and the mechanical response, namely the axial displacement field, have been performed. The material properties have been set according to the prescriptions shown in the section 4.1, taking into account for the influence of temperature on the parameters. The simulations have been formulated considering various boundary conditions and interactions.

Among the boundaries conditions, the first one is related to the difference of potential applied on the pads, located in the right part of the device (on one pad the ground is connected, while on the other pad a potential is imposed). Once more it is emphasized that this represents the driving force of the whole system: through the electrical flow inside the beams, heat is generated; due to the temperature increase and to the constraints at the beam extremity, the beams deform and elongate and, so, displacement is generated for the whole shuttle.

Both the displacement and the force generated are proportional to the applied potential; therefore, to determine the maximum output, several values have been simulated, all providing an upper temperature below the melting point for the material, which corresponds to the temperature of $1,414°C$. Practically, the fusion limit corresponds to imposing a voltage slightly higher than $25 - 26\ V$, which, for this reason, will be the upper voltage limit.

The second set of boundary conditions concerns the fixed mechanical constraints of the device, which are:

- the pads, on which the potential difference is applied i.e. suspension springs' anchors;

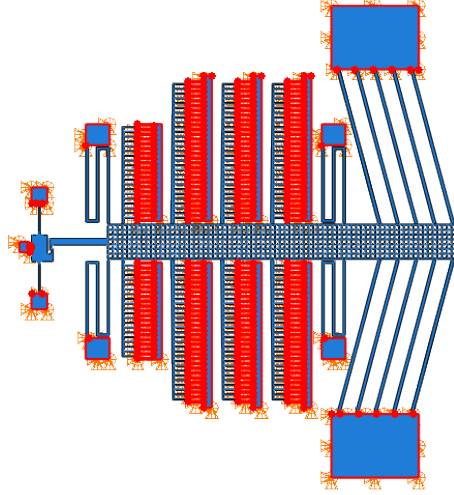- the stators, which are fixed to the substrate;

- the bullet anchor.

Figure 4.11: Fixed portions of the device in red colour.

As for the previous simulations described in section 4.3, also in this case a prescribed temperature value, equal to 298 K, has been assigned to the fixed anchors of the suspension springs. This condition has been also imposed to the parts which do not belong to the shuttle central body, such as the stators and the bullet.

The other boundary conditions are referred to the thermal dissipation, which is mainly due to surface radiation. In this work, only the upper shuttle surface has been considered for the radiation phenomenon, through the definition of its emissivity value. This parameter is the most relevant between the whole parameter set, because it determines the maximum reachable temperature. Unfortunately, in literature a precise temperature dependence of the emissivity is missing and, thus, multiple simulations have been carried out, with different voltage and emissivity values. The coefficients chosen for voltage are: 5 V, 8 V, 10 V, 13 V, 15 V, 17 V, 19 V and 25 V; while for the emissivity, the assigned values are the same considered in the thermal steady-state simulations, thus: 0.10/ 0.21/ 0.35/ 0.49/ 0.65. With this procedure, a complete overview of all the possible expected thermal profiles can be obtained, and then, through the comparison with experimental tests, the optimal value of emissivity could be determined.

Together with this dissipation condition, also the convection effect has been imposed on the same surface; as described in literature, the latter phenomenon is negligible compared to the pradiation condition, and this has been also confirmed by the simulations. Indeed, it is responsible of just a few K decreases.

4.4.1. Results of 3D coupled FE simulations

For each value of the difference of potential five different emissivity values have been evaluated, as explained in the previous section 4.4. Therefore, from this procedure 40 simulation results have been obtained. In this way, it has been possible to achieve a complete overview of both the thermal and mechanical behaviour for the micro-system. Among the two behaviours, the thermal will be the first reported. Firstly, it must be remarked that the qualitative profile of the temperature distribution is independent on the driving voltage applied, as already reported in section 4.3.

The figures 4.12(a) and 4.12(b) report the portions of the shuttle in which a temperature increase has been observed. Indeed, differently from what predicted by the starting 2D FE simulations performed by [2], the temperature increase is confined only into these device's parts, while the expected distribution has shown to be an exponential decreasing function in the whole structure, as predicted from the simplified model of the single rod (see section 4.3).

(a) *Thermal profile of the right portion of the device.*

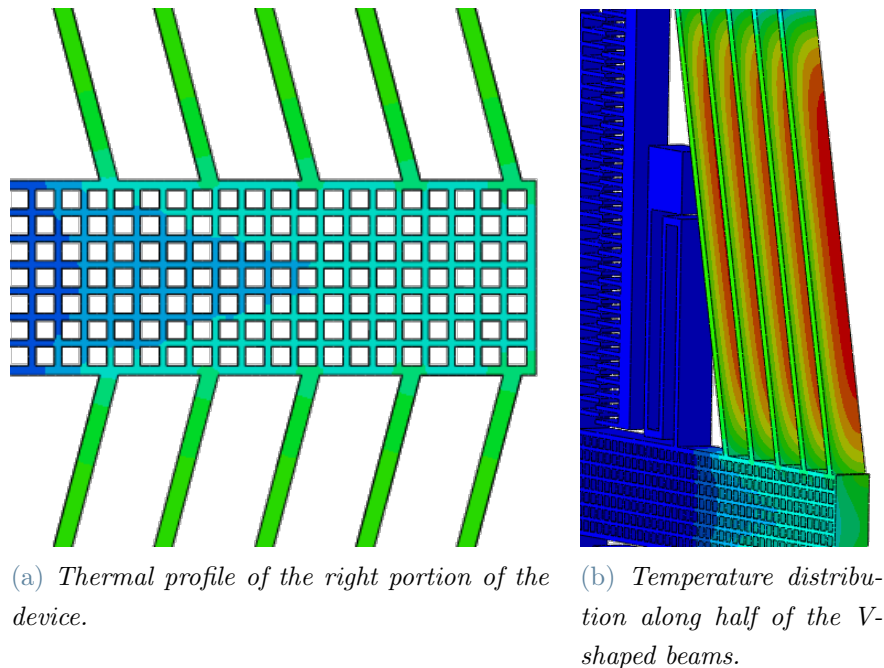(b) *Temperature distribution along half of the V-shaped beams.*

Figure 4.12: Qualitative temperature profiles of the heated portions of the central shuttle and of inclined beams for the ETA4.

This unexpected trend could be a tridimensional effect catched by the FE analysis, versus the two dimensional case previously run in [2]. Indeed, a higher maximum temperature was expected, equal to $1,191\ K$, for a considered emissivity value of 0.65 and a driving

voltage of 5 V. Instead, for the same input parameters, the obtained results are depicted in figure 4.13, in which the horizontal ETA, the bullet and the target structures are represented. Possibly, in the 2D analyses the radiation boundary condition on the top surface has been wrongly assumed to be effective, while it has been applied, instead, only to the exterior-in-plane surface; the misunderstanding about the boundary condition imposition could be responsible of the different results reported below.
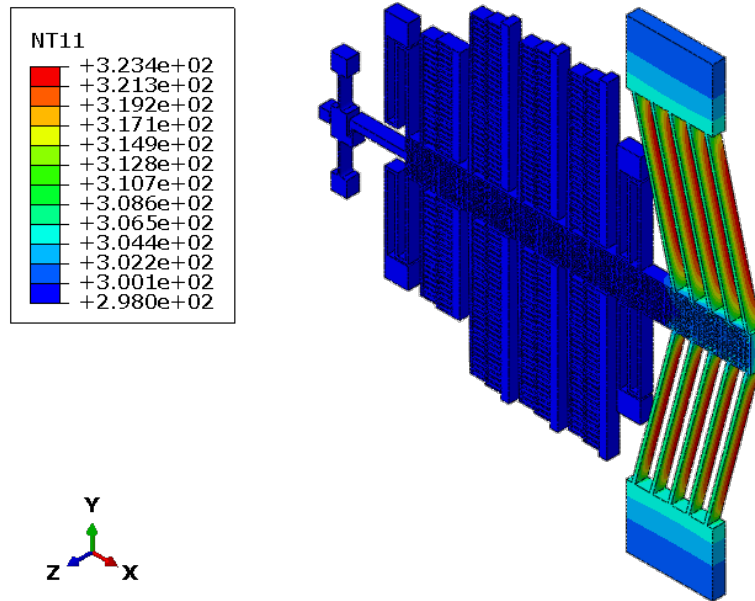

Figure 4.13: Temperature profile (in K) for ETA4, considering an emissivity equal to 0.65 and an input voltage equal to 5 V.

As it can be seen, the temperature values rise from the two lateral pads, reaching the maximum (323 K) in correspondence of the lateral and bottom surfaces of the V-shaped ETA.

The firstly performed simulations have considered only 5 V for the difference of potential, while in the plots shown in figure 4.14 the whole set of results in terms of the temperature distribution along the inclined beam are reported, for the different potentials and emissivities imposed. Indeed, the data is taken from the most heated portion of the device, the actuation part, thus the V-shaped beams. Due to the radiative condition on the upper surface, combined with the high resistivity of the considered body, the maximum temperature is located at the bottom part of the device, more precisely of the beams, as it can be noticed in figure 4.12(b). In the pictures reported below (figure 4.14), the effect of radiance thermal losses against the difference of potential applied is visible: thus the five curves depicted in every plot represent the temperature distribution along one of the inclined beams for varying values of emissivity.
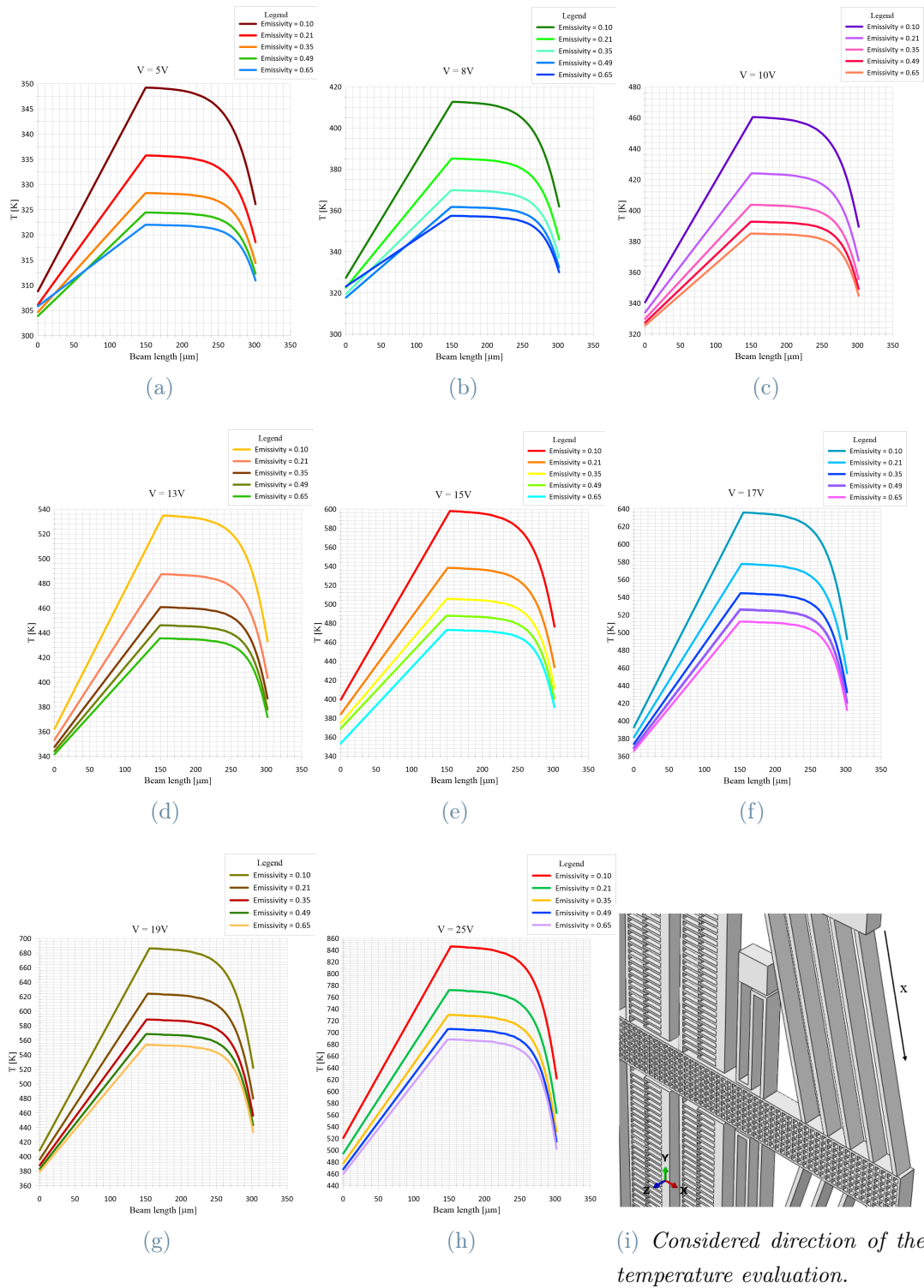
Figure 4.14: Temperature evolution along the ETA4 beams at different voltage difference and at varying emissivity values. The data between 0 and 150 μm are referred to the extremity values.

(a)

(b)

(c)

(d)

(e)

(f)

(g)

(h)

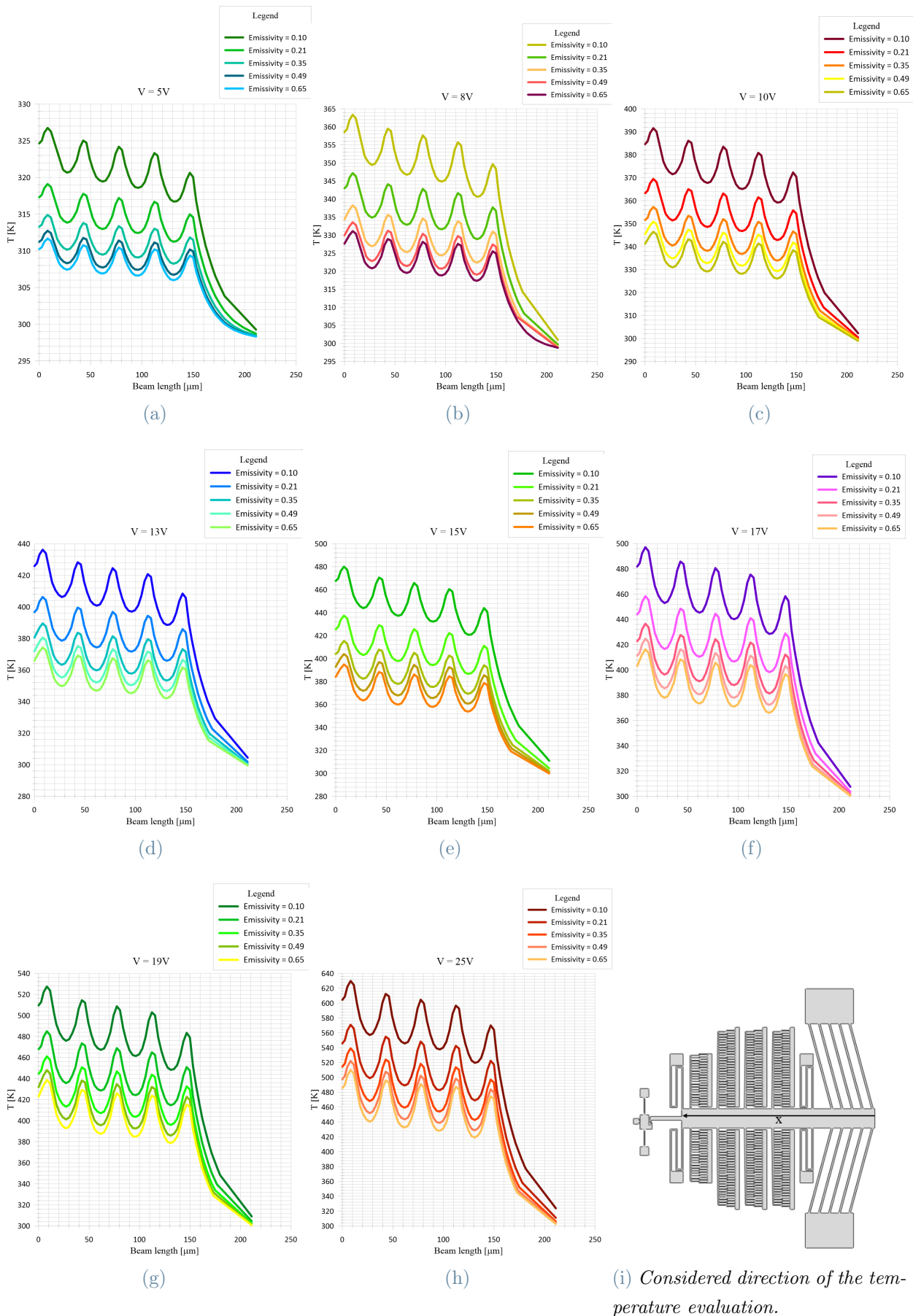(i) *Considered direction of the temperature evaluation.*

Figure 4.15: Temperature evolution along the ETA4 right portion at different voltage difference and at varying emissivity values.

As expected, the application of a surface radiation condition influences significantly the maximum reachable temperature in the shuttle. The same outcome can be also observed considering the temperature profile of the right portion of the shuttle, depicted in figure 4.15. The temperature profile of the "head" of the horizontal shuttle is depicted, which includes the region of the V-shaped ETA till the first supporting spring. This part of the device, together with the inclined beams, is the only section affected by a significant temperature variation. Indeed, in the plots it is possible to point out five different temperature peaks before the fast decrease to room temperature ($298\ K$), representing the connections between the beams and the central portion of the micro-system, in which the temperature is higher.

This result, described only by the temperature field, directly affects the horizontal displacement of the whole structure. Indeed, due to the lower temperature values obtained, the displacement, along the x-direction, is far less compared to the predicted value of $3.91\ \mu m$ in [2], obtained through 2D FE simulations, which are indeed related to a maximum reached temperature of $1191°C$. The displacement is, in fact, strictly related to the temperature by the working principle of the device itself; due to Joule's heating of the inclined clamped beams, which form the V-shaped ETA, the axial motion of the shuttle is induced by their deformation. The coupling between the different physical fields involved is emphasized by the temperature dependence of the set parameters, allowing both to obtain more precise results and to impose the evolving temperature as the driving principle, affecting all the material properties and so the solving equations. Indeed, exceeding the voltage value of $15\ V$, thus reaching a reasonably high temperature, the displacement profile along the shuttle follows the temperature profile; therefore, a higher displacement is present in the "head" region, which drags the whole module. The two pictures, $4.16(a)$ and $4.16(b)$, represent two different cases (emissivity fixed to 0.1 and the potentials set equal to $15\ V$ and $25\ V$), highlighting the strict relationship between temperature and displacement: in fact, the red region in the device "head" represents the part in which a higher motion is visible, but also corresponds to the module's section affected by a superior heat generation rate. However, for lower temperature values, the displacement profile is homogeneously distributed along the central shuttle, as reported in the figure $4.16(c)$.

(a) *Displacement distribution in the right portion of the ETA4 considering 15 V and 0.1 emissivity.*

(b) *Displacement distribution in the right portion of the ETA4 considering 25 V and 0.1 emissivity.*

(c) *Displacement profile along the shuttle ETA4, considering 25 V and 0.1 concerning emissivity .*
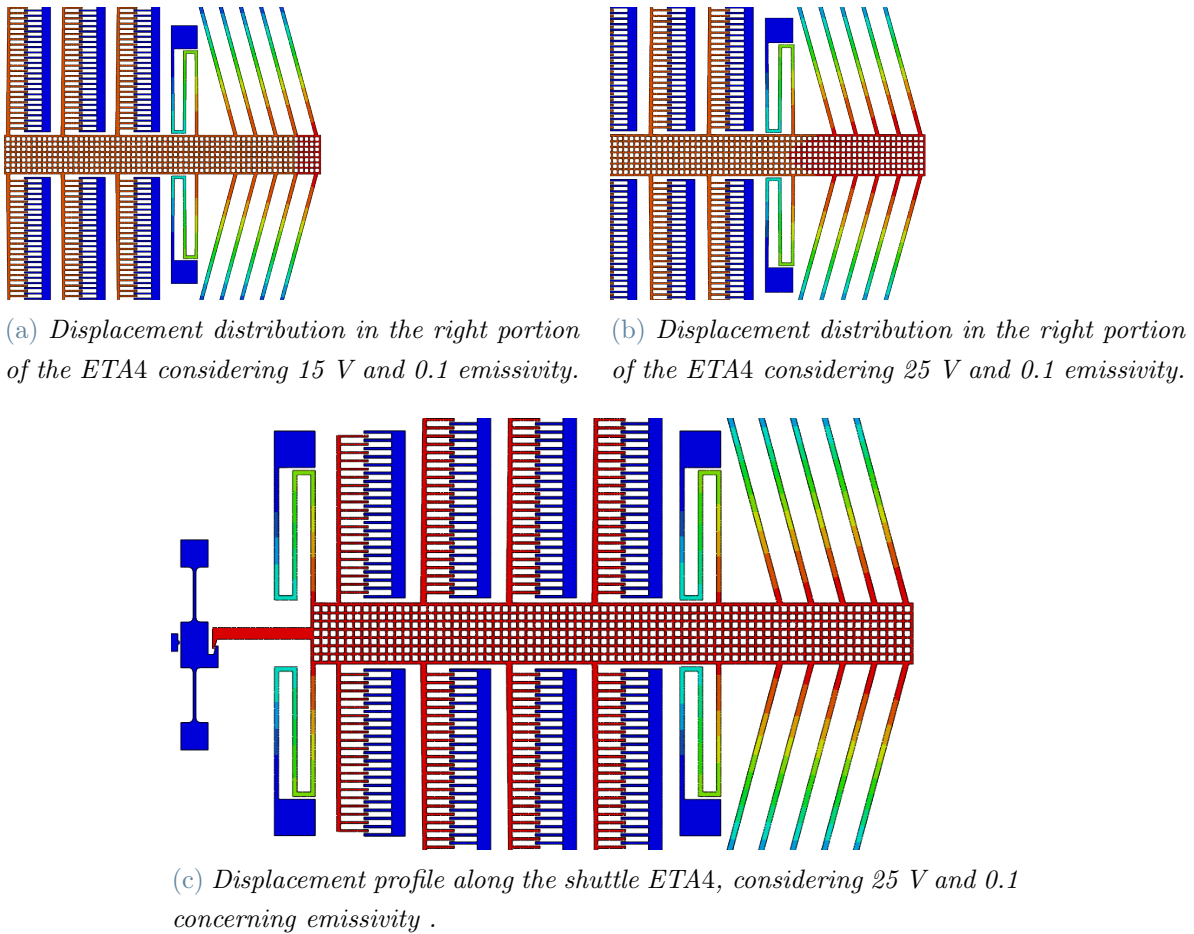
Figure 4.16

Intuitively, the maximum displacement value has been achieved by setting the lowest emissivity value and the upper limit for the potential, therefore 0.1 and 25 V respectively; the obtained result is reported in figure 4.17. The horizontal displacement of the ETA shuttle is equal to 2.7 μm. This value is sufficient to hook the bullet, if an uniform over-etch value of 0.3 μm all over the external boundaries of the device is considered, because the distance between the sample's hook and the device's one becomes equal to 2 μm.

Introducing a stiff object like the bullet itself, the movement of the thermal-actuator could be hindered, if the force and the displacement generated would be enough to hook the sample.

The result is represented in the figure 4.18, where it can be seen that the maximum horizontal displacement generated from the actuation module is equal to 2.55 μm, thus reduced compared to the 2.7 μm obtained considering the actuator alone (without the bullet).

This effect results from an increase both in the total mass and in the global stiffness,

which turn reduces the motion of the ETA. It can also be understood by looking into the analytical description of the motion principle, in which a inverse proportionality between the displacement and the specimen stiffness has been considered, see section 2.4.
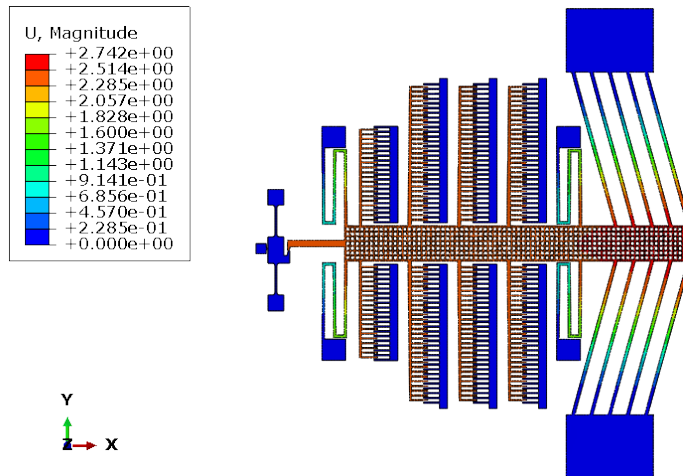

Figure 4.17: Displacement, in μm, along the x-direction of the horizontal shuttle for an applied voltage of 25 V and an emissivity value of 0.1.
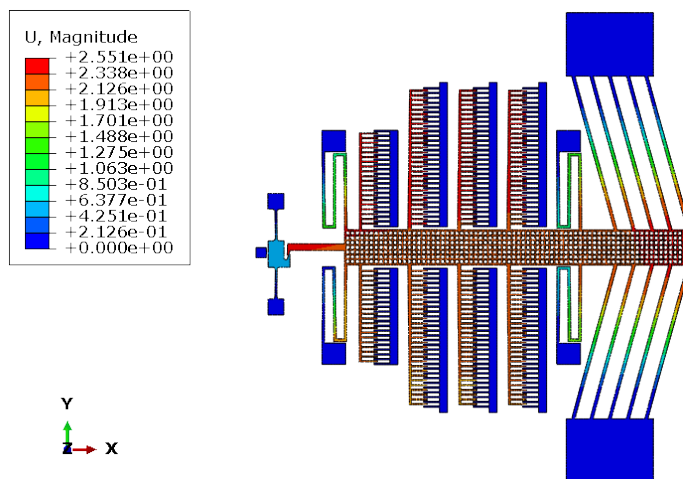

Figure 4.18: Contact between the actuation module and the bullet for an applied voltage of 25 V and an emissivity value of 0.1.

The stress distribution has been also evaluated, to estimate the integrity of the system. Another parameter that could affect the entirety of the model is the temperature, but, as reported, the maximum achieved value has been significantly less than the melting temperature of the polysilicon, thus it does not affect the structural integrity.

Both the stresses arising in the actuator and the ones in the region comprehending the bullet and the hook system are quite low, as it can be seen in figure 4.19.
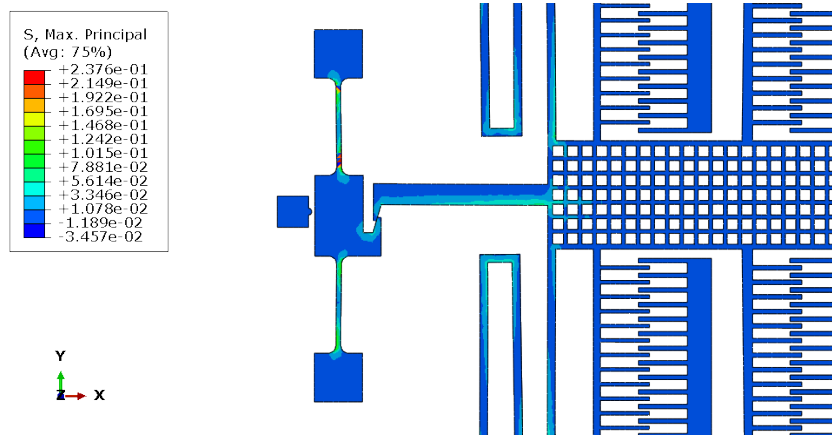

Figure 4.19: Stresses, in MPa, arising in the region comprehending the bullet and the hook system (input: 25 V and $\varepsilon = 0.1$).

The presence of low stress values depends on the small motion of the bullet, caused by an inadequate horizontal displacement of the shuttle, which is not able to charge the bullet itself and, thus, to rise internal stresses both in the lower and in the higher parts of the hook.

5 | Experimental set-up and results

This chapter presents the experimental configurations and the results obtained, both for the ETA3 and for the ETA4, particularly regarding the maximum reached displacement by each device shuttle and the release and impact procedure, aimed to the material characterization. To create an axial horizontal motion of the bullet, see figure 2.22 related to ETA4, a deformation is required for the actuation part of the shuttle; it is recalled once more that it is achieved by imposing a potential difference at the anchored pads attached to five couples of symmetrical beams (see figure 2.14). However, to fully characterise an ETA device, additional tests need to be carried out; therefore, in this chapter the following test types will be described:

- *Test A)* (purely) capacitance voltage (C-V) test on the comb finger capacitors;

- *Test B)* frequency response analysis in an assigned frequency range, associated to the shuttle motion;

- *Test C)* voltage-current tests along the inclined beams;

- *Test correspondD)* electro-thermal-actuation of the device, possibly including either capacitance sensing or the hook-unhook mechanism.

The procedures for these four test types are collected at the beginning of this chapter; subsequently, the relevant results for ETA3 and ETA4 are instead presented.

5.1. Description of the test types

5.1.1. Test A: C-V on the comb finger capacitors

The capacitance change is the key quantity to monitor the horizontal motion of the module; a capacitance increase corresponds to a motion of the rotor comb finger in the direction

of the stator. The C-V (capacitance versus DC bias voltage) response of a micro-system is, therefore, a relevant characteristic of the system. To evaluate the capacitance that varies with the applied DC bias voltage to a stator, a small AC signal is superimposed to the DC bias voltage. Usually, a MEMS shows a small capacitance (on the order of pF or fF), due to its reduced dimensions, thus the device must be sensible to these capacitance values with a high resolution at a low signal level. Precise DC bias voltage output is also required to make an accurate C-V measurement; thus, to satisfy these requirements auto-balancing bridge instruments are usually employed. This component, is formed by to two terminals, labelled Low and High connections; since the Low terminal is sensitive to incoming noise, it is important that it is not connected to the substrate that is electrically connected to the prober's noisy ground where floating charges could be located.
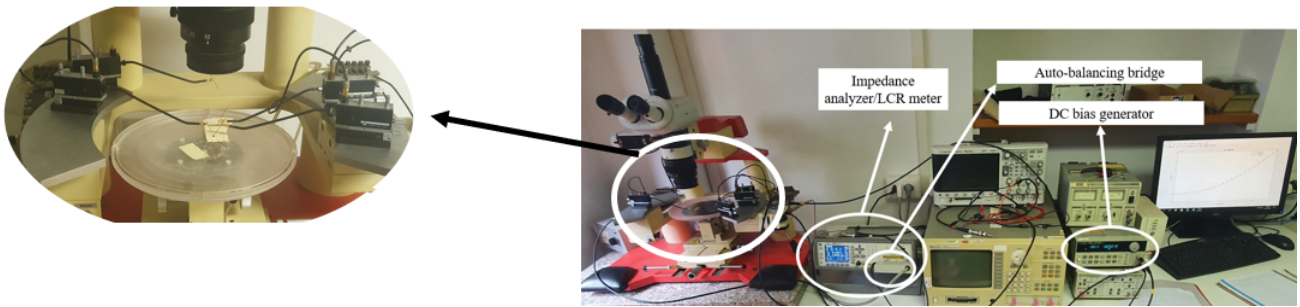

Figure 5.1: Overview of the experimental setup: probe station with micromanipulators, LCR meter, DC supply, digital spectrum analyzer and current amplifier.

The first C-V tests aim to detect possible malfunctions or manufacturing defects that could hinder the device motion: a DC bias is applied to the comb-finger stators, through the High connection with the LCR meter, while the rotor is put to Low, as depicted in figure 5.2).
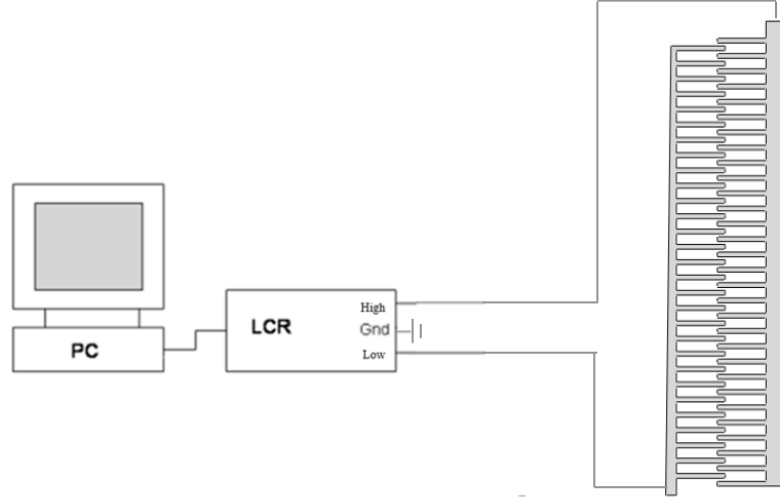
Figure 5.2: Set-up used for C-V standard analysis.

The possibility for the shuttle to move has been verified; moreover, information on the module stiffness, necessary for the over-etch identification, has been retrieved.

5.1.2.   Test B: frequency response function (FRF) for the shuttle horizontal motion

It is a measurement used to identify the resonant frequencies of a physical MEMS structure. A FRF is a complex function containing an amplitude and a phase term, equal, respectively, to the ratio between the input and the response, and to the change in the output phase, as a consequence of the input signal. The so-described function has real and imaginary components, such that:

$$Amplitude = \sqrt{Real^2 + Imag^2}, \tag{5.1}$$

$$Phase = tan^{-1}(\frac{Imag}{Real}). \tag{5.2}$$

Transforming the FRF into real and imaginary terms, it can be noticed that:

1. the real part is equal to zero at the resonance frequencies;

2. the imaginary part shows peaks (either negative or positive) in correspondence of the resonant frequency values.

The measurement exploits a digital signal analyzer giving an AC voltage signal, in a frequency range, at a stator and reading the output from a second source (typically, another stator). The Fast Fourier Trasnform of the ratio output/input signal is observed in real time, achieved by a remote control, and, subsequently, used to obtain the amplitude and the phase of the mechanical response. To flatten purely electrical peaks in the response, the measurement is repeated with and without a displacement offset applied to the rotor, through a DC voltage provided by the DC supply.

5.1.3.   Test C: voltage vs current along the inclined beam

To detect the maximum operative input for the ETAs, the experimental relationship between the input current and the resultant voltage has been investigated. The experimental setting is represented in figure 5.3, where the actuator pads have been connected to the two poles of the DC supply, to focus on the effect of the temperature increase on the relationship between the potential difference and the current.

Either DC voltage or current control is possible in this test; in both the cases the quantity which is not applied as input needs a maximum safety limit, to avoid device failures due to overheating. For example, in case of current control, the current values are imposed by the DC supply and a voltage limit has to be set. If this limit is reached during the test, the instrument prevents further voltage increases, possibly affecting current increases, too. A similar behaviour can be observed when the voltage control is in effect, i.e. a current limit is active.
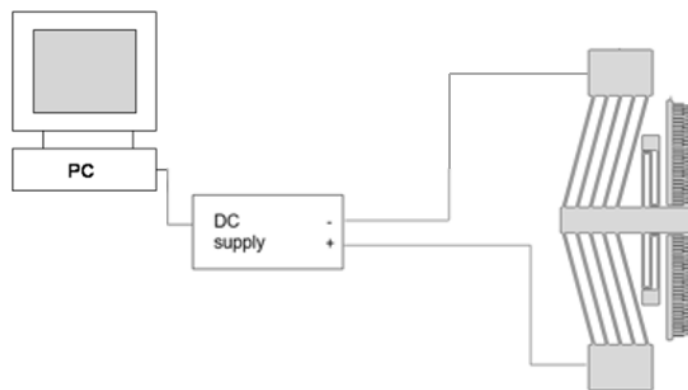

Figure 5.3: Experimental set-up for V-I tests.

5.1.4. Test D: electro-thermal tests

The analysis has been performed by forcing a driving current through a DC generator on the pads (see figure 5.4) and measuring the displacement thanks to the capacitance increase, detected by the LCR meter at the comb finger capacitors. Data acquisition has been achieved by connecting in series with the negative pad both the ground and the Low of the LCR meter, while the High has been applied to the comb finger stator.
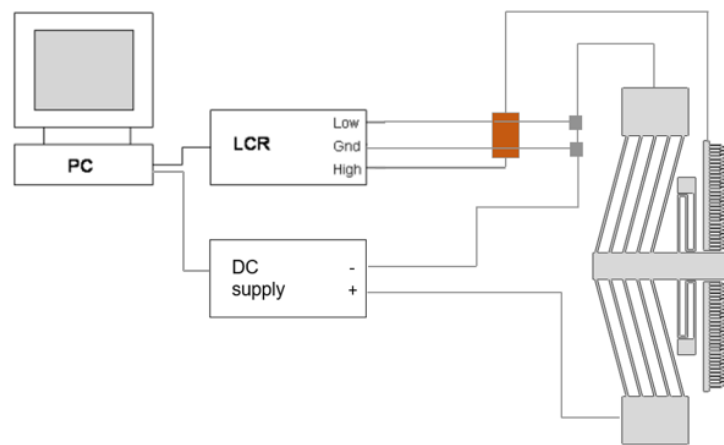

Figure 5.4: Schematic representation of experimental set-up concerning the ETA3 module.

Experimentally, this has been obtained by using micro-manipulators with tungsten tips, in turn connected through wires to a DC supply. A Matlab software on a PC allows the control of the driving potential but also enables to impose the amplitude and the frequency of the AC signal, superposed to the DC one, necessary for the capacitance variation measurement. The input signal, which can be either a current or a potential difference, is let to grow with a regular step. Between two successive steps of the input signal increase, a delay time has been introduced to allow the correct acquisition of the measurements, required by the fact that the single acquisition of the increase in capacity is averaged multiple times; this increases the accuracy of the measurement and reduces the effects of external sources of noise; for each step of the driving current, 30 averages have been considered.

Considering ETA4, the experimental set-up is similar to the configuration used on ETA3, with the only difference is related to inverted LCR meter connections: the High connection is applied to the negative pad, while the Low on the stator arm of the comb-fingers

(depicted in figure 5.5). These settings have been tried as an alternative, because the previous ones did not guarantee reasonable results. Since this other setting did not work either, then it has to be concluded that there is something wrong with the device, as it will be discussed in section 5.4.
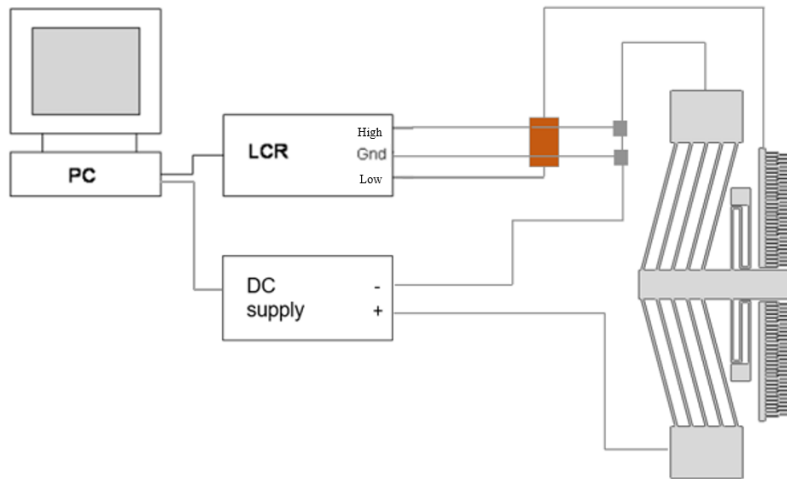

Figure 5.5: ETA4: alternative experimental set-up used in the the electro-thermal C-V tests.

5.2. Results from tests on ETA3

5.2.1. Test A

Following the experimental set-up described in the section 5.1.1, the capacitance variation measurement, as a function of the applied DC bias to the comb-finger stators, has been obtained. The measurement has been carried out by setting, through the Matlab script, a potential difference equal to 20 V, increased regularly by interval of 1 V; between two subsequent steps, a number of averages equal to 20 has been set, to eliminate most of the background noise. After the maximum driving value has been reached, it has been decreased, along the same path, as a counter-proof for a correct measurement. An AC signal has been also superimposed on the DC, characterized by a frequency of 500 kHz and an amplitude equal to 400 mV; the motion of the comb-finger, as can be seen in the figure 5.6, has led to obtain an increasing exponential response to the applied difference of potential, verifying the actual absence of possible defects that could hinder the correct functioning of the device.
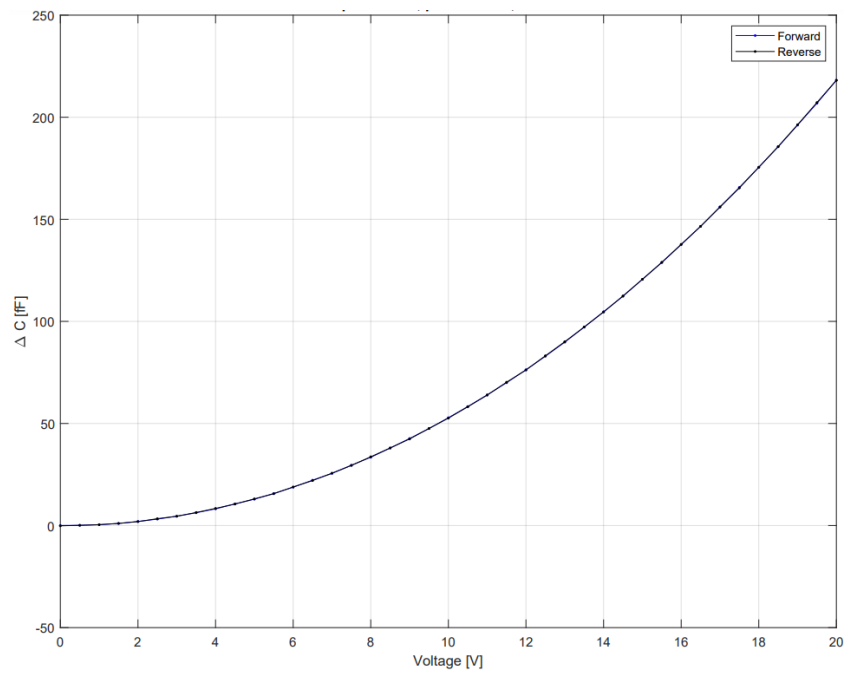
Figure 5.6: C-V response, as obtained from the testing procedure on ETA3.

5.2.2. Test B

FRF analyses has been performed to evaluate the resonant modes of the module; the obtained result is reported in figure 5.7: a peak has been observed in correspondence of 12.5 kHz, which represents the resonant frequency related to shuttle oscillation.
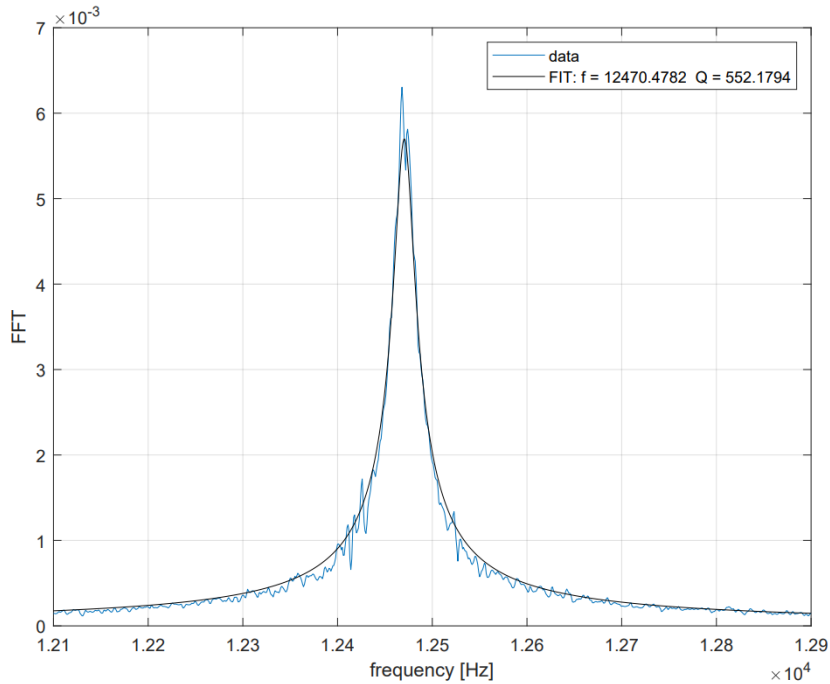
Figure 5.7: FRF of ETA3, it shows the resonant peak at 12.5 kHz; Q=quality factor.

The measurement has been repeated several times to ensure a reliable estimation of the measured parameter. However, the resonant frequency value is too low to influence the CV response.

5.2.3.   Test C

The evaluation of the maximum input has been performed by applying a signal, either current or voltage, to the actuation pads of the module, following the configuration depicted in figure 5.3. In the results, a loss in the linearity of the V-I trend has been observed, when the current value of 20 mA is exceeded. A maximum allowable current value of 30 mA has been experimentally ascertained, which corresponds to about $18 - 18.5$ V, above which the actuation beams burn, making the device unusable.

Concerning the influence of temperature on the electrical resistivity, as reported in the section 4.1, the resistivity increases proportionally to the temperature, leading to a higher heat dissipation.
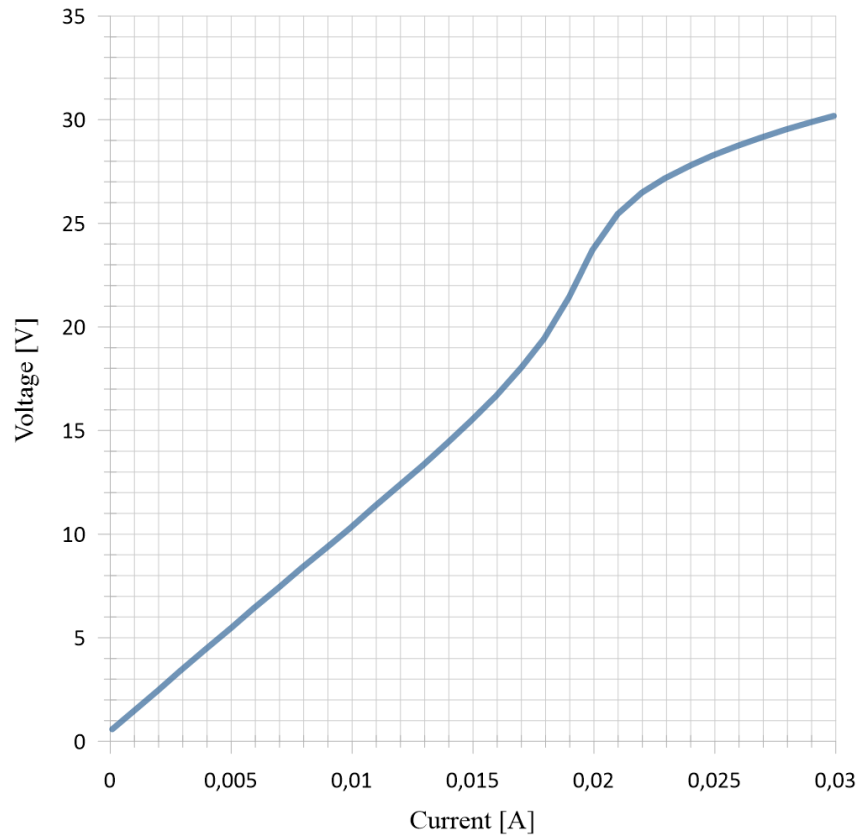
Figure 5.8: V-I curve for ETA3.

5.2.4. Test D

In the following tests, a DC bias signal, superposed with an AC signal with an amplitude equal to $400\ mV$ and a frequency of $500\ kHz$, has been applied on the actuation pads, which must induce the actuation beams deflection, due to the Joule's effect which generates a temperature gradient along them, providing the horizontal motion of the whole shuttle.

To check the reliability and repeatability on the performed analysis, the driving current has been imposed for ten subsequent times. Following this aim, different current values have been considered: 10 mA, 15 mA, 17 mA, 20 mA, 25 mA and 30 mA; a ramp up to these values and then down to 0 has been imposed, at a regular pace (1 mA), averaging each measurement 30 times. A good matching between the ten analysis has been achieved, implying the possibility to perform repeatable tests. The results are shown in the figure 5.9.
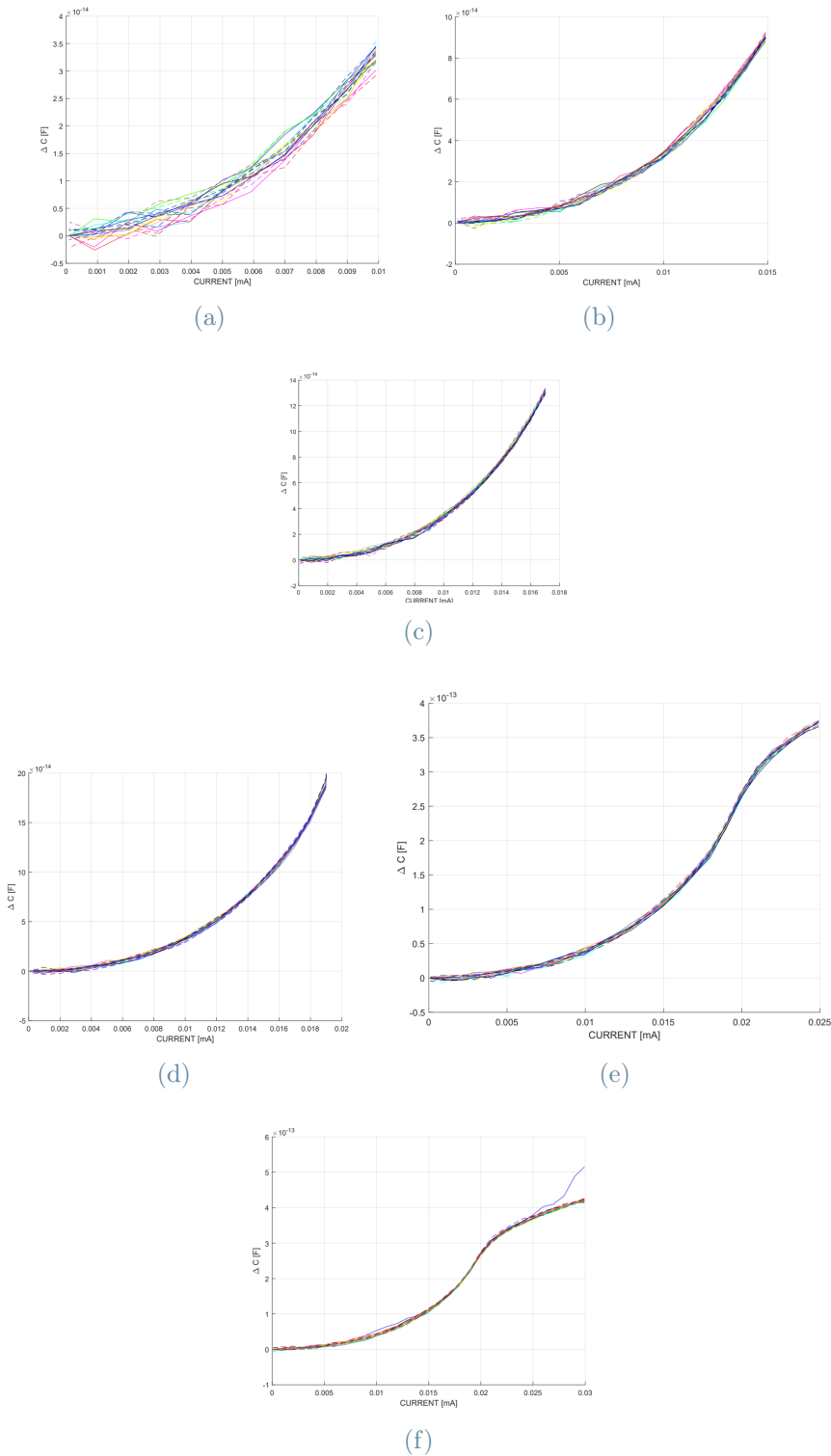
(a)

(b)

(c)

(d)

(e)

(f)

Figure 5.9: Repeated tests on ETA3, considering the following current values: (a) 10 mA, (b) 15 mA, (c) 17 mA, (d) 20 mA, (e) 25 mA and (f) 30 mA.

Exceeding the input of 20 mA, the measured capacitance variation tends to flatten out,

as depicted in the figures 5.9(e) and 5.9(f); the reason for this change can be related to the hook between the horizontal shuttle and the "hammer".

From the capacitance results, which have been obtained and depicted in figure 5.9, the motion of the module can be evaluated through the equation 2.7 as:

$$x = \frac{\Delta C d}{2\varepsilon_0 t N}. \tag{5.3}$$

Combining the equation 5.3 with the results reported in the figure 5.9, the following displacement values are obtained:

I [mA]	$\Delta C \cdot 10^{-14} [F]$	Displacement $[\mu m]$
10	3.2	1.51
15	9.0	4.24
17	13	6.12
20	20	9.41
25	37	17.41
30	41	19.3

Table 5.1: Displacement values for the ETA3 module as a function of the driving current.

As it can be seen from the displacements reported in the table 5.1, the maximum motion of the module is less than the theoretical limit of 20 μm, considered in the design phase (see section 3.4).

The following step has been the experimental procedure leading to the mechanical impact of the polycrystalline silicon sample: it requires the application of the potential difference on both the horizontal and vertical ETA pads. Concerning the bigger, horizontal shuttle, the voltage difference has been gradually increased till reaching the upper current limit, equal to 30 mA, to preload the impacter and generate the maximum achievable impact force. In this configuration, an instantaneous potential has been imposed to the vertical ETA to bend the hook and release the "hammer". However, differently from what that has been predicted in the work [9], such a testing procedure has not shown the expected results: the collision does not break the rod, henceforth excluding the possibility of carrying out an impact characterization.

5.3.   Results from tests on ETA4

5.3.1.   Test A

Also for ETA4, as for ETA3, the first performed analysis has been the verification of the correct motion of the module, performed (as previously described in the section 5.2.1) through an applied difference of potential, equal to 40 V, reached by subsequent constant steps equal to 1 V, and then decreased following the same path; for each acquisition, to eliminate noises, 30 averages have been applied. An AC signal is superimposed to the DC one, to evaluate the sensing arms motion, the AC signal has been characterised by an amplitude of 400 mV and an oscillating frequency of 500 kHz. The result in figure 5.10 does not evidence possible causes of hindrance to movement, verifying the absence of manufacturing defects.
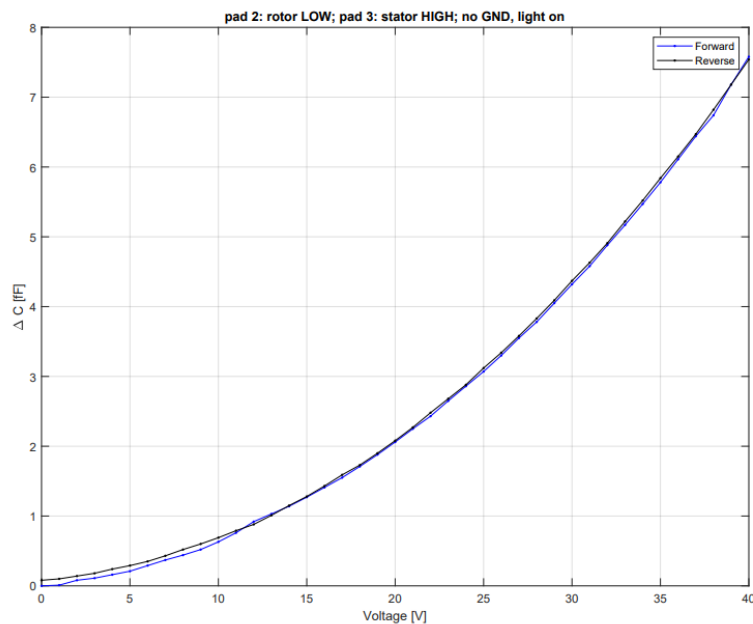

Figure 5.10: C-V response, as obtained from the testing procedure on ETA4.

5.3.2.   Test B

To get insights into the resonant modes, numerical simulations have been carried out. Therefore, a frequency mode analysis (through Abaqus) has been performed to investigate the possible vibration modes of the module in a frequency range between 0 Hz and 1 MHz, looking for modes which cause a horizontal motion of the shuttle and deformations

in the sensing portion (i.e. the arms with the comb fingers).

The simulations have highlighted several vibrational modes, in the scanned frequency range, but only one horizontal mode, in correspondence of 19.650 kHz. Starting from the vibrations, they affect both the V-shaped beams and the comb-fingers' arms, and actually have been observed in the whole considered frequency range. The only exception has been found at 19.650 kHz, when, through the axial deformation of the actuation inclined beams, the module moves along the x-direction. The figure 5.11 reports the obtained result, pointing out the maximum deformed portion with a red colour.

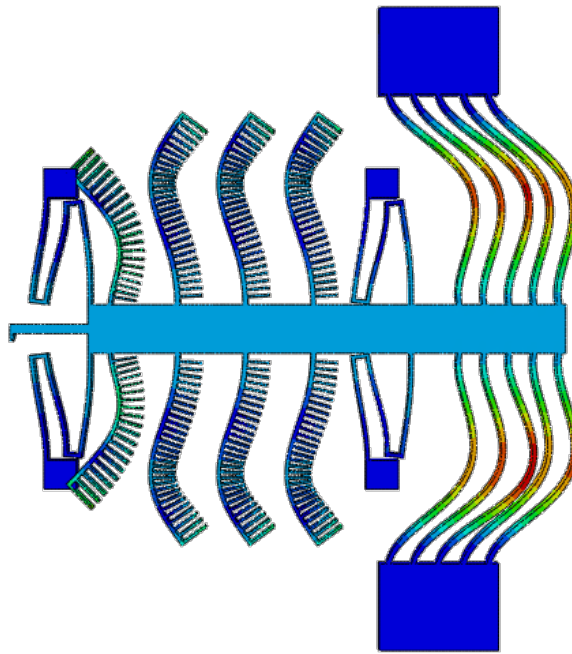Figure 5.11: Resonant mode along the x-direction for the module ETA4.

To validate the simulated results and to ascertain the presence of a resonant frequency around 19.650 kHz, the frequency response function has been experimentally evaluated between 0 Hz and 50 kHz. A resonant frequency peak in correspondence of about 18 kHz has been found (figure 5.12), which approximately validates the previous result.
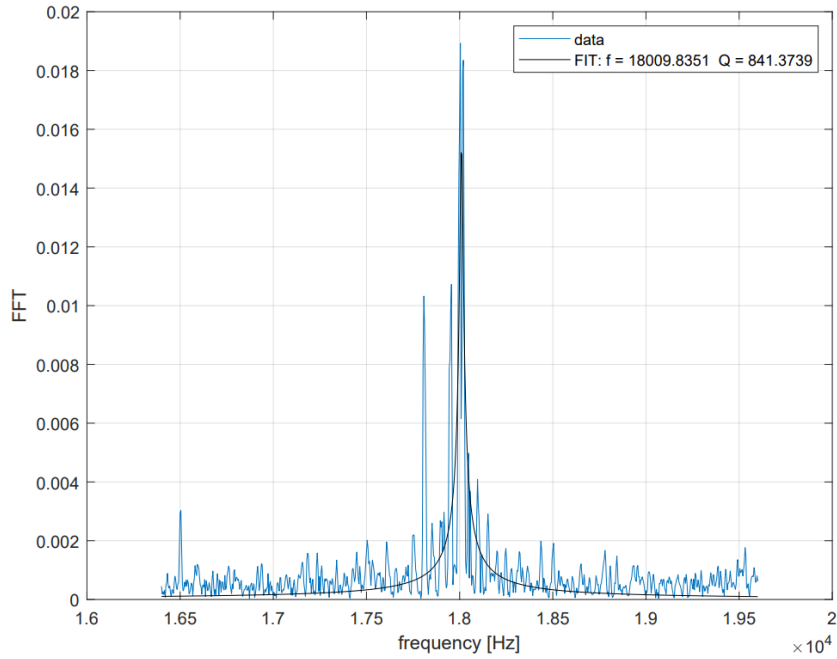
Figure 5.12: ETA4: resonant frequency peak of the module; Q=quality factor.

The resultant resonant frequency of the ETA4 assumes a value too low to be considered the cause of the unexpected shape of the $\Delta C - I$ curve, leading to look for other possible reasons.

5.3.3. Test C

Also on this device, as has been observed, concerning ETA4 (see section 5.2.3), a loss of the ohmic regime has been detected when the current value of 20 mA (figure 5.13) is exceeded, but in addition to this, if the input signal is further increased, a bending of the sensing arms occurs, causing a short-circuit. This has also been observed in subsequent measurements with the LCR meter, where the capacitance change has suffered an instantaneous collapse towards zero (figure 5.14). More precisely, what happens is a deformation of the single comb, which, by bending, comes into contact with the face of the corresponding stator. The so described situation does not allow to determine a true upper input limit, except for the reaching of the polysilicon melting temperature, but prudentially an operative limit at the end of the linear response can be envisaged.
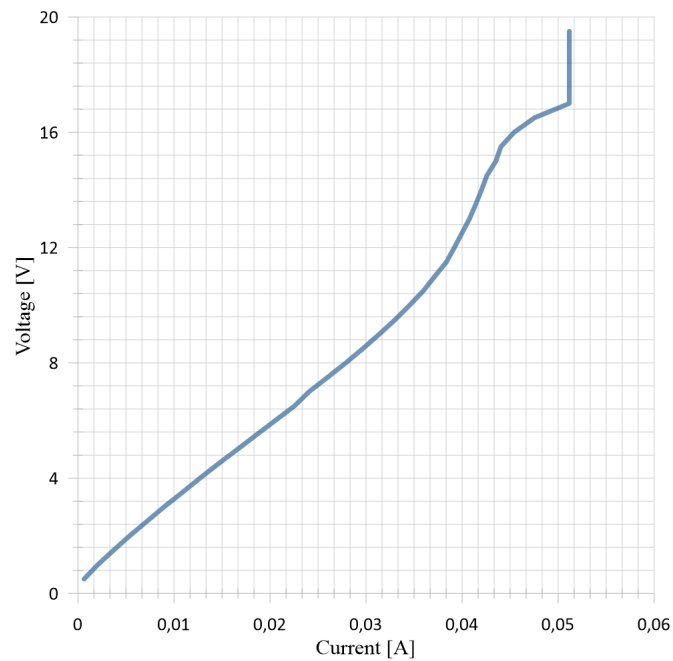
Figure 5.13: V-I curve on ETA4.

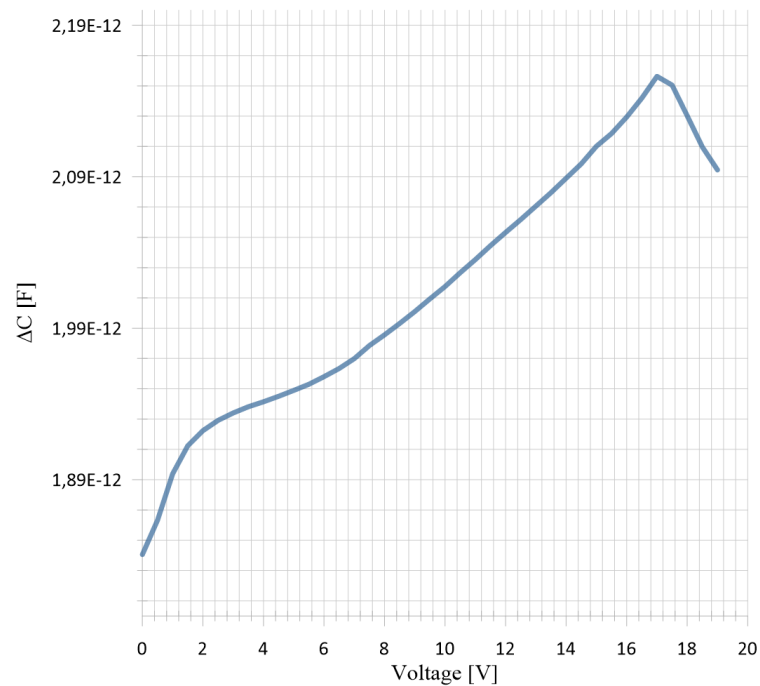
Figure 5.14: ETA4: drop in the capacity value.

5.3.4.   Test D

The device under consideration has been designed to reproduce the (accidental) impact behaviour of the polysilicon through the micro fabrication of a movable "sling-like" device.

The horizontal displacement of the whole shuttle, due to the Joule's heating induced deformation of suitably designed V-shaped actuators, must be sufficient to drag the sample with the whole shuttle; the generated force must also overcome the increase in the overall stiffness, raised by the the bullet's junction. Indeed, the horizontal shuttle is 1.4 μm away from the bullet; thus, firstly, the motion of the module must reach this distance, after which the ETA's tail becomes connected through a hook to the bullet. In order to do that, a compromise between the generated displacement and force must be found; the tuning is done by varying the angle of the inclined beams in the electro-thermal actuated portion of the module. More precisely, relatively high distances can be achieved designing a small inclination; on the other hand, the rising in the angle is proportional to an increase in the maximum force attainable (see also section 2.4).This feature will be also checked, to guarantee the optimal functioning of the module, through repetitive tests using the same input features at different current level, which can be easily reinterpreted in potential difference terms, if the equivalent resistance of the device equal to 330 Ω is taken into account for the considered current levels are: $10\,mA/$ $15\,mA/$ $17\,mA/$ $19\,mA/$ $20\,mA/$ $25\,mA/$ $30\,mA$. Together with the DC input, an AC, with a frequency of 500 kHz and an amplitude of 400 mV, has been superimposed. Thanks to the Matlab script, the analysis has been performed following the same procedure described in the section 5.2.4: both the forwards and the backward path are followed, with an increasing step of 1 mA, each averaged 20 times.

Figure 5.15 reports the results obtained by comparing ten tests on the same module, for the current values reported before.

As it can be seen, a repeatable behaviour has not been obtained, excluding the possibility of performing an objective testing procedure on a such designed device.

It must be also noticed the different shapes of the curves with respect to the expected one, which should follow the same trend depicted in figure 5.10. Indeed, instead of getting a monotonically increasing path with a positive concavity, the obtained results show a slower growth and a negative concavity.
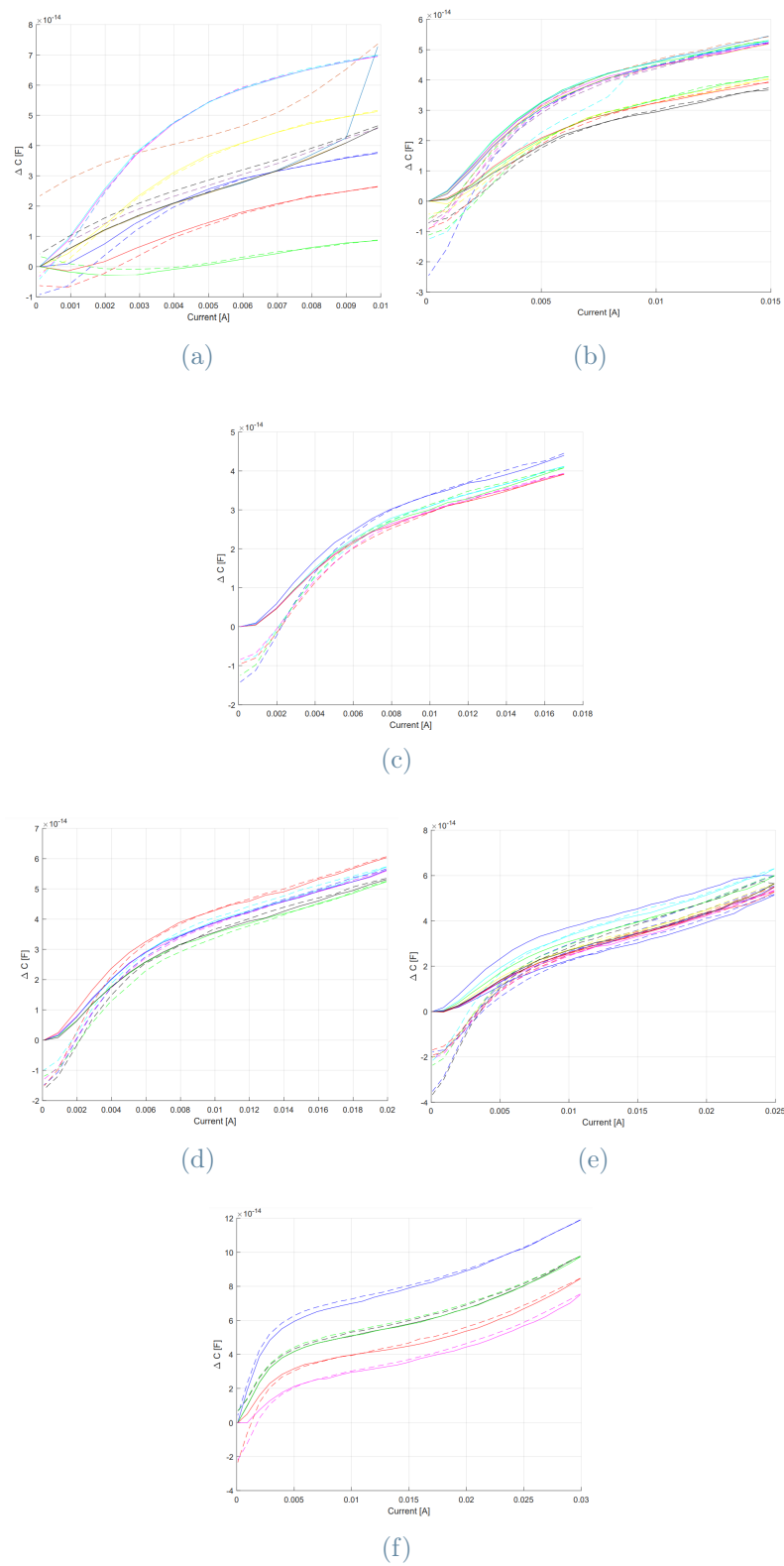
Figure 5.15: Repeated tests on the same module, considering the following current values: (a)$10mA$, (b)$15mA$, (c)$17mA$, (d)$20mA$, (e)$25mA$ and (f)$30mA$.

However, independently from the applied driving current, the shapes of the resulting curves show always the same trend; a linearly increasing part can be distinguished at the beginning, followed by a reduction in the slope. The first trait cannot be associated with a real increase in capacity variation since, as can be observed in the CV plot reported in figure 5.10, the initial growth starts with a null derivative value. On the other hand, the subsequent part of the plot depends either on the voltage saturation due to reaching the temperature/displacement limit, or on the increase in the overall mass and stiffness due to the coupling with the bullet.

5.3.5. Electro-mechanical simulations

A possible explanation for the unexpected shape of the C-V curves obtained from the testing of ETA4, figure 5.15, could be the effect of the bending of the rotor's arms. To verify this hypothesis, a numerical analysis, carried out according to [11], is presented in this section.

The model considers two comb-finger arms with different length (figure 5.16), as present in the module, embedded in an air layer which separates the two plates of the capacitor. When the bending occurs, the geometry of the air gap changes continuously, resulting in an electric field variation between the two electrodes.
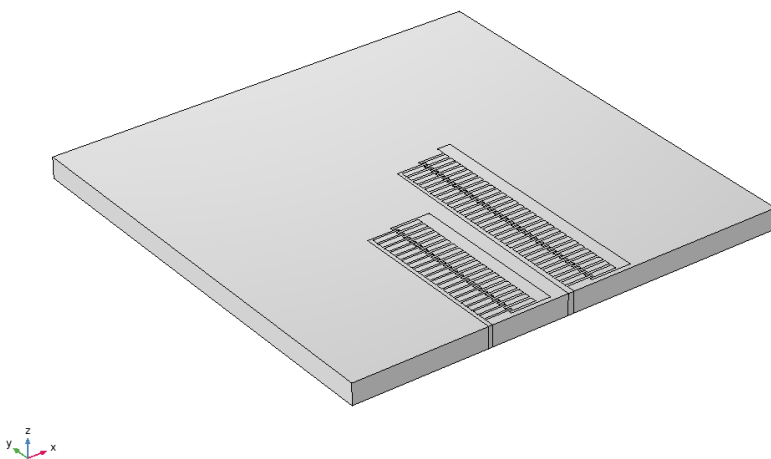

Figure 5.16: Model, created with the Comsol software, used to simulate the electromechanical problem.

The Poisson's equation governs the electrostatic field both in the air and in the solid domain, i.e. comb-fingers:

$$-\nabla \cdot (\varepsilon \nabla V) = 0, \tag{5.4}$$

where derivatives are taken with respect to the spatial coordinates. The numerical model represents the electric potential and its derivatives on a moving mesh with respect to the spatial frame.

The arms on the left are connected to a voltage terminal with a specified bias potential, while the ones on the right are grounded.

The force density that acts on the capacitor's face of the comb-fingers results from the Maxwell's stress tensor:

$$F_{es} = -\frac{1}{2}(E \cdot D)n + (n \cdot E)D, \tag{5.5}$$

where E and D are the electric field and electric displacement vectors, respectively, while n is the outward normal vector to the boundary.

From these analyses, by imposing a potential difference in the range between 100 mV and 130 mV (higher voltages will cause the contact of the two terminals, terminating the simulation), the bending of the left arm of both the two portions has been obtained. The simulations have been developed by imposing a potential difference on the fixed portion, thus the stator, and letting the motion free in the x-direction. The bending has been also guaranteed by anchoring to the ground the bottom part of the rotors, which corresponds to the joint which the central body of the shuttle. The surrounding air has been also modelled, ensuring the presence of a dielectric medium between the capacitor plates.

This configuration implies the imposition of a moving mesh of the fluid domain, corresponding to the the solid well motion. This is fundamental to simulate accurately the reduction in the air gap in the capacitors, resulting in a change in the perceived electric field (figure 5.18), and, thus, in the electrostatic force. The mesh deformation has been associated to a not defined motion of the considered domain, which is calculated during the course of the simulation, and therefore depends on the electrostatic force established between the two faces of the capacitor. The whole set of simulations has been carried under the stationary time hypothesis.
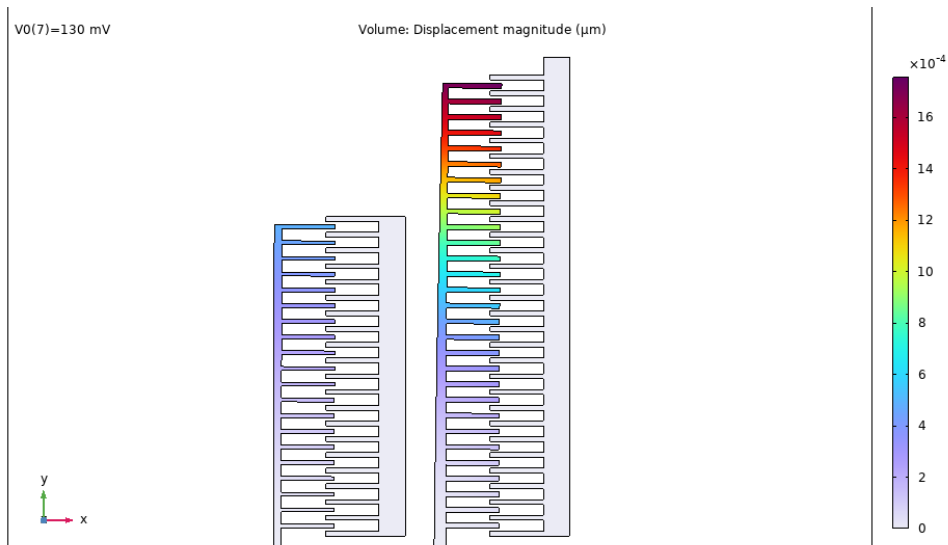
Figure 5.17: Bending of the comb finger arms, for an applied voltage which ranges between 100 mV and 130 mV.
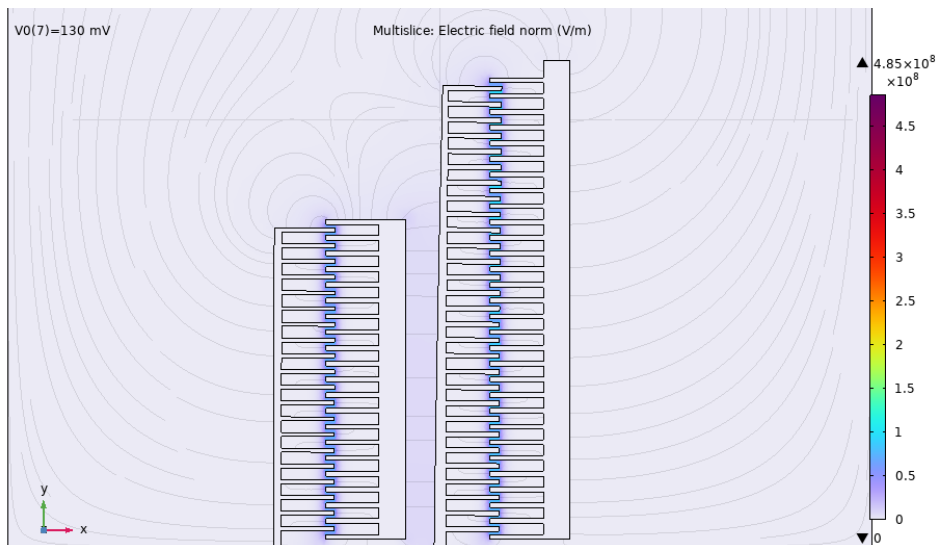

Figure 5.18: Electric field generated in the area of the comb-fingers plates.

The obtained results show an increase of the capacitance value, but, due to the small range of voltages in which the analysis has been carried out, the obtained shape has, instead of a smooth-growth trend, a parabolic trend, as reported in the figure 5.19.
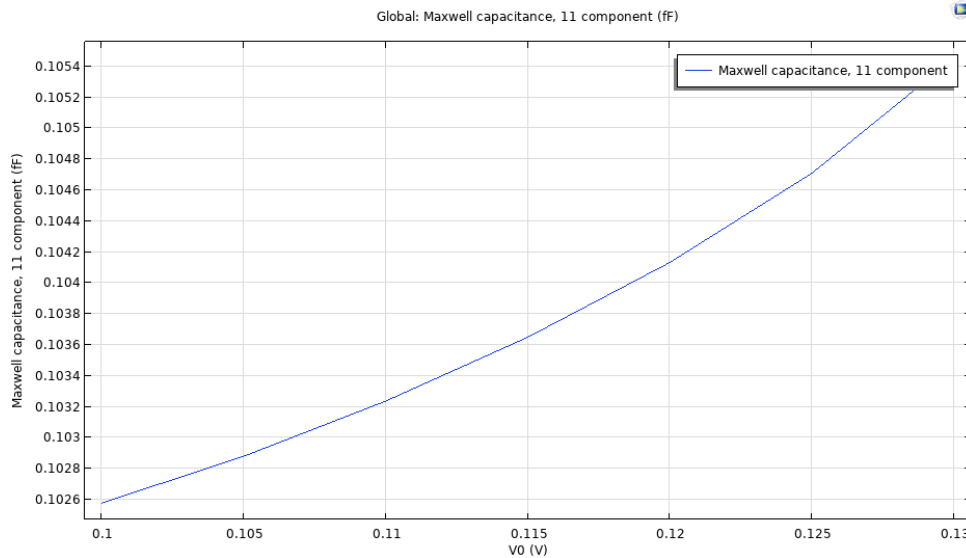
Figure 5.19: Numerical change of capacitance, as a consequence of the bending of the comb-fingers arms.

5.4.   Discussion

The testing procedure, both on ETA3 and on ETA4, has begun with the detection of possible malfunctions or manufacturing defects, which could prevent the shuttle from moving or cause unexpected behavior of the module, through a standard C-V test (figure 5.2). For both devices, the same expected trend has been obtained, characterized by monotonic growth, highlighting the absence of factors that could hinder the correct functioning of the structure (figures 5.10 and 5.6). This result has allo to proceed with the evaluation of the upper input limit, through the observation of the V-I curve (figure 5.3). The obtained results have show a loss in the ohmic trend of such curve, when the current value of 20 mA has been exceeded, due to the temperature effect on the electrical resistivity; indeed, by rising the heat generation, the resistivity increases too, reducing the electron flow inside the device. This phenomenon has affected both the ETAs, but, concerning the ETA3, a maximum operative current has been detected at 30 mA, while, for the ETA4, a bending of the comb-fingers has been instead observed, leading to the contact between the parallel surfaces of the sensing portion, i.e. short circuit. This has been confirmed by a drop in the capacitance variation measure, as is depicted in figure 5.14.

After having determined the operational input range of the structure, the analysis has moved on the actual motion of the shuttle; it has been performed by following the setting shown in figures 5.4 and 5.5 for ETA3 and ETA4, respectively. While for ETA3 the expected result has been obtained, which implies a horizontal translation of the module

following the heating and the subsequent deformation of the inclined beams, for ETA4 the trend of the $\Delta C - V$ curves assumes instead an unexpected shape. Moreover, if the repeatability of the tests is considered, while for the first ETA3 the ten tests have confirmed the repeatibility, for ETA4 this has not been possible (figure 5.15), as each test has shown a different trend from the others. This has led to a shift in the interest to investigating the reasons why the device has not been working properly. In this regard, two hypotheses have been formulated; the first has considered the possible oscillations caused by the AC signal as the reason of possible inaccuracies in the measurement of the capacity variation. About this, a FRF test has been carried out, on both the ETAs, aimed at the identification of possible resonance frequencies around that characteristic of the applied AC signal; such circumstance could in fact set the comb-fingers arms in dynamical motion, modifying the actual measured capacity value. However, for both the electro-thermal actuators the observed resonance frequency have been found significantly lower than the input signal, thus excluding this possible explanation. A second hypothesis has considered the bending of the comb-fingers arms; in regard to this, electro-mechanical simulations have been set up to check the deformation of the comb finger arms (section 5.3.5). The analysis has been conducted in the potential range of 100-130 mV, because higher potential will cause errors in the simulation. These simulations have emphasized the deformation of the comb finger arms caused by the the electrostatic force, proportional to a variation in the electric field perceived by the parallel faces of the capacitors; this result also explains the $\Delta C - V$ curve shape, and at the same time it confirms the vey small motion of the ETA4, a circumstance that unfortunately excludes the possibility of carrying out the polycrystalline silicon impact characterization.

6 | Conclusions and future perspectives

Objective of this thesis work is to compare different ETA, for on-chip mechanical characterisation of structural materials used in the MEMS fabrication processes. More precisely, both tensile and impact test can be performed using the considered modules, to determine stiffness and effective Young's modulus values. By considering, in fact, the device present in [9] and [2], the "chipping" phenomenon at the micro-scale of polycrystalline silicon could be investigated, as this event has become a problem more and more diffuse, mainly due to the rapid diffusion of MEMS in everyday applications.

After presenting the common features between the different devices, such as the actuation mechanism, the sensing portion and suspension springs, the study has been developed by simulating numerically the latest designed device, [2], to reproduce, in the most accurate way, its working condition.

The focus has then moved on the ETA4, firstly by employing numerical simulations, then by carrying out experimental tests. The numerical analyses have been carried out by imposing the temperature dependence for most of the parameters, to account for the coupling between the three involved physical domains. Temperature increase is the relevant quantity for the module's motion, triggered by the driving input potential difference. Applying a potential at the support pads, placed in the right part of the central shuttle, a temperature gradient rises along the clamped inclined beams, inducing their deformation, and therefore, the motion of the whole module in the right direction, along the x axis. The temperature increase is guaranteed by the Joule's effect, under the hypothesis of unitary Joule heat fraction, which means that all the input electrical power is converted into heat without losses. From the simulations a lower displacement has been found, with respect to the expected value, as obtained from the starting 2D FE analysis reported in [2], where a displacement of 3.91 μm at a temperature of 1400 K, considering an actuation potential of only 5 V, was predicted. These promising initial results have been contradicted by the 3D simulations carried out, since, despite having considered several potential-emissivity combinations, the maximum displacement value reached has been only 2.7 μm at a tem-

perature of 860.5 K.

The testing procedure has been performed both on ETA3 and ETA4 (see chapter 5); on both the devices a preliminary analysis has been executed to determine their correct working, which could be hindered either by the presence of manufacturing defects or by possible adhesion phenomena occurring in the movable portions. Therefore, a standard C-V test has been performed to evaluate the response of the sensing portions to the driving signal. The operating limits of the devices have then been studied, by imposing a difference of potential to the pads. This has revealed, for ETA4, a nonlinearity in the relationship V-I, due to the temperature increase and to the influence this has on the material properties, more precisely on the electrical conductivity. An operative limit has to be set at the end of the linear trait. On the other hand, considering the ETA3, a maximum input current equal to 30 mA can be detected, which results sufficiently low to keep the ohmic trend of the V-I curve.

After acquiring this initial information regarding the two thermo-actuators, the study has focused on their actual motion. By imposing the driving signal on the actuation pads and observing the horizontal movement of the shuttle, through the increase in the variation of capacitance, sensed by the LCR meter connected following the schemes reported in figure 5.4 and 5.5, different behaviors for the two devices have been found: an actual motion for ETA3, characterized by the possibility of performing repeatable tests, and unexpected results for ETA4. In the latter case, in fact, the resultant curves, instead of showing an increasing parabolic response for the C-V curve, have presented a non standard nonlinear shape, as described in the chapter 5.

Concerning the ETA4 module, also the repeatability of subsequent tests has not been guaranteed, as it has been shown in figure 5.15. To understand the origin of this unexpected result, two possible hypotheses have been formulated: the first, also suitable for verifying the results obtained for the ETA3 device, admits that the input signal in AC can induce a mechanically resonance to the structure, affecting the reliability of the results. In regard to this, FRF tests have been conducted to evaluate the resonance frequencies of both modules; the results have been obtained between 12 and 18 kHz. To support this hypothesis, frequency mode simulations have also been conducted on ETA4, showing at 19.650 kHz a resonant mode related to the shuttle motion along the x axis. Unfortunately, the frequency values have been much lower than the applied AC frequency, excluding this explanation as a possible cause in the C-V curve mismatch. The second hypothesis has proposed the bending of the comb finger arms as a possible cause of the unexpected capacity value measured by ETA4; to this aim, electro-mechanical simulations have been conducted to verify whether the increase in the electrostatic force, due to an increased proximity between the faces of the capacitor, might have caused the bending

of the sensing arms (see section 5.3.5). A deformation of these has been actually found, which has led to an increase in capacity, but without a sensible shuttle motion.

Considering the actuation mechanism, it must be said that the beam inclination for ETA4 is equal to 15°, which, as it has been said in the chapter 3, allows to achieve high forces at the expense of the maximum allowable horizontal motion of the shuttle. This observation, combined with the experimental test observations, has led to the reasonable hypothesis that the device moves much less than what expected from the simulations. Therefore, a sufficient kinetic energy, required to generate an impact necessary for the characterization of the polycrystalline silicon, has not been obtained.

For this reason, a modification of the module will be proposed in future works, by reducing the beam inclination. A good compromise between the generated force and the achieved displacement must be found; this compromise can be reached considering an angle of 5° or a few degrees higher.

Bibliography

[1] Abaqus. *Abaqus (2021) Theory Manual. Version 2021, Dassault Systemes Simulia, Inc., https://help.3ds.com. Last accessed on March 27, 2022.*

[2] M. Bollati. Modelling, simulation and design of an electro-thermal microactuator for on-chip dynamic testing. Master's thesis, M. Sc. Double DegreeMaterials Engineering and Nanotechnology Mechanical Engineering, 2018.

[3] C. Bourgeois, E. Steinsland, N. Blanc, and N. De Rooij. Design of resonators for the determination of the temperature coefficients of elastic constants of monocrystalline silicon. In *Proceedings of International Frequency Control Symposium*, pages 791–799. IEEE, 1997.

[4] F. Cacchione, A. Corigliano, B. De Masi, and C. Riva. Out of plane vs in plane flexural behaviour of thin polysilicon films: Mechanical characterization and application of the weibull approach. *Microelectronics Reliability*, 45(9-11):1758–1763, 2005.

[5] M. Chiao and L. Lin. Self-buckling of micromachined beams under resistive heating. *Journal of Microelectromechanical Systems*, 9(1):146–151, 2000.

[6] A. Corigliano, L. Domenella, H. D. Espinosa, and Y. Zhu. Electro-thermal actuator for on-chip nanoscale tensile tests: analytical modelling and multi-physics simulations. *Sensor Letters*, 5(3-4):592–607, 2007.

[7] A. Corigliano, L. Domenella, and G. Langfelder. On-chip mechanical characterization using an electro-thermo-mechanical actuator. *Experimental Mechanics*, 50(6):695–707, 2010.

[8] A. Corigliano, R. Ardito, C. Comi, A. Frangi, A. Ghisi, and S. Mariani. *Mechanics of microsystems.* John Wiley and Sons, Ltd, 2018.

[9] L. Domenella. Attuatori elettro-termo-meccanici per microsistemi. Master's thesis, Master thesis in Electronic Engineering, Politecnico di Milano, 2004/2005.

[10] A. A. Geisberger, N. Sarkar, M. Ellis, and G. D. Skidmore. Electrothermal properties

and modeling of polysilicon microthermal actuators. *Journal of Microelectromechanical Systems*, 12(4):513–523, 2003.

[11] R. K. Gupta. *Electrostatic Pull-In Structure Design for In-Situ Mechanical Property Measurements of Microelectromechanical Systems (MEMS)*. PhD thesis, Massachusets Institute of Technology, Cambrigde, MA,, 1997.

[12] P. Hirsch and S. Roberts. The brittle-ductile transition in silicon. *Philosophical Magazine A*, 64(1):55–80, 1991.

[13] P. Hirsch and S. Roberts. Modelling plastic zones and the brittle-ductile transition. *Philosophical Transactions of the Royal Society of London. Series A: Mathematical, Physical and Engineering Sciences*, 355(1731):1991–2002, 1997.

[14] M. A. Hopcroft, W. D. Nix, and T. W. Kenny. What is the young's modulus of silicon? *Journal of Microelectromechanical Systems*, 19(2):229–238, 2010.

[15] F. P. Incropera, D. P. DeWitt, T. L. Bergman, and A. S. Lavine. *Fundamentalsof Heat and MassTransfer*. John Wiley and Sons, Ltd, 2007.

[16] G.-B. Lee, R.-S. Chen, and C. J. Kung. Analysis of optimal inclined angles on v-shaped electro-thermal microactuators. *Journal of the Chinese Society of Mechanical Engineers, Transactions of the Chinese Institute of Engineers, Series C/Chung-Kuo Chi Hsueh Kung Ch'eng Hsuebo Pao*, 23(2):155–162, 2002.

[17] C. D. Lott, T. W. McLain, J. N. Harb, and L. L. Howell. Modeling the thermal behavior of a surface-micromachined linear-displacement thermomechanical microactuator. *Sensors and Actuators A: Physical*, 101(1-2):239–250, 2002.

[18] A. Masolin, P.-O. Bouchard, R. Martini, and M. Bernacki. Thermo-mechanical and fracture properties in single-crystal silicon. *Journal of Materials Science*, 48(3):979–988, 2013.

[19] A. D. McConnell, S. Uma, and K. E. Goodson. Thermal conductivity of doped polysilicon layers. *Journal of Microelectromechanical Systems*, 10(3):360–369, 2001.

[20] A. Potekhina and C. Wang. Review of electrothermal actuators and applications. In *Actuators*, volume 8, page 69. Multidisciplinary Digital Publishing Institute, 2019.

[21] J. Samuels and S. Roberts. The brittle–ductile transition in silicon. i. experiments. *Proceedings of the Royal Society of London. A. Mathematical and Physical Sciences*, 421(1860):1–23, 1989.

[22] D. S. Simulia. *Abaqus (2021) Analysis User's Manual. Last accessed on March 27, 2022.*

[23] Y. Zhu, A. Corigliano, and H. D. Espinosa. A thermal actuator for nanoscale in situ microscopy testing: design and characterization. *Journal of Micromechanics and Microengineering*, 16(2):242, 2006.